Computational and Mathematical Methods in Medicine

Application of Computational Methods and Mathematical Models in Nuclear Medicine and Radiotherapy

Lead Guest Editor: Adam Konefal
Guest Editors: Maria Sokół and Sebastian Adamczyk

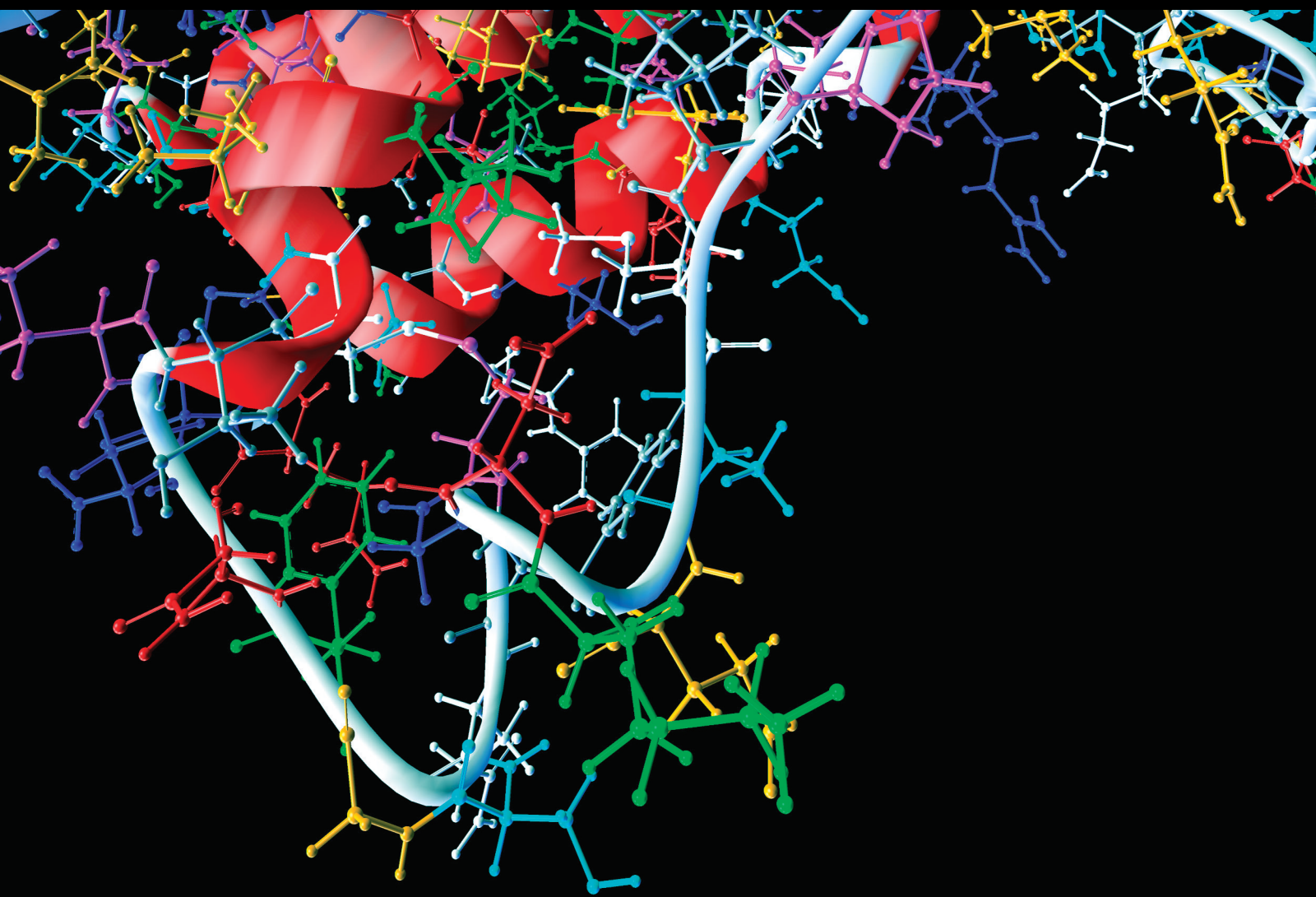

Application of Computational Methods and Mathematical Models in Nuclear Medicine and Radiotherapy

Computational and Mathematical Methods in Medicine

Application of Computational Methods and Mathematical Models in Nuclear Medicine and Radiotherapy

Lead Guest Editor: Adam Konefal
Guest Editors: Maria Sokół and Sebastian Adamczyk

Contents

Hindawi
Computational and Mathematical Methods in Medicine
Volume 2020, Article ID 5972594, 11 pages
https://doi.org/10.1155/2020/5972594

Research Article

Holistic View on Cell Survival and DNA Damage: How Model-Based Data Analysis Supports Exploration of Dynamics in Biological Systems

Mathias S. Weyland,[1,2] **Pauline Thumser-Henner**,[3,4,5] **Katarzyna J. Nytko**,[3,4,5] **Carla Rohrer Bley**,[3,4] **Simone Ulzega**,[1] **Alke Petri-Fink**,[2,6] **Marco Lattuada**,[6] **Rudolf M. Füchslin**,[1] **and Stephan Scheidegger**[1]

[1]*Zurich University of Applied Sciences Winterthur, Switzerland*
[2]*BioNanomaterials Group, Adolphe Merkle Institute, University of Fribourg, Fribourg, Switzerland*
[3]*Division of Radiation Oncology, Vetsuisse Faculty, University of Zurich, Zurich, Switzerland*
[4]*Center for Applied Biotechnology and Molecular Medicine (CABMM), University of Zurich, Zurich, Switzerland*
[5]*Center for Clinical Studies, Vetsuisse Faculty, University of Zurich, Switzerland*
[6]*Department of Chemistry, University of Fribourg, Fribourg, Switzerland*

Correspondence should be addressed to Mathias S. Weyland; mathias.weyland@zhaw.ch

Received 10 September 2019; Revised 10 April 2020; Accepted 21 May 2020; Published 6 July 2020

Academic Editor: Reinoud Maex

In this work, a method is established to calibrate a model that describes the basic dynamics of DNA damage and repair. The model can be used to extend planning for radiotherapy and hyperthermia in order to include the biological effects. In contrast to "syntactic" models (e.g., describing molecular kinetics), the model used here describes radiobiological semantics, resulting in a more powerful model but also in a far more challenging calibration. Model calibration is attempted from clonogenic assay data (doses of 0–6 Gy) and from time-resolved comet assay data obtained within 6 h after irradiation with 6 Gy. It is demonstrated that either of those two sources of information alone is insufficient for successful model calibration, and that both sources of information combined in a holistic approach are necessary to find viable model parameters. Approximate Bayesian computation (ABC) with simulated annealing is used for parameter search, revealing two aspects that are beneficial to resolving the calibration problem: (1) assessing posterior parameter distributions instead of point-estimates and (2) combining calibration runs from different assays by joining posterior distributions instead of running a single calibration run with a combined, computationally very expensive objective function.

1. Introduction

DNA damage and repair is a critical aspect of radiotherapy, where tumor cells are killed by irradiation. The radiation induces DNA damage which eventually leads to cell death if the damage cannot be repaired successfully. Mild hyperthermia is a treatment to boost radiotherapy by heating up the cancer cells to temperatures between 41°C and 43°C. While the exact working principles of hyperthermia and its interaction with radiotherapy is still subject to research [1], it has been shown that hyperthermia acts as a radiosensitizer by affecting the DNA repair that takes place after an irradiation event [2–5]. In consequence, knowledge about the dynamics of DNA damage and repair is essential in order to optimize hyperthermia treatment plans.

For radiotherapy, in silico modeling is employed to assist in treatment planning decisions. Such planning is based on Monte Carlo simulations or kernel methods and deliver dose-volume histograms [6]. Beyond these geometric dose calculations, approaches to shape the prescribed radiation dose according to the biological properties of the tumor have been proposed but are currently not established [7]. The prescribed dose of radiation is generally divided into fractions that are delivered in subsequent sessions; however, this

fractionation scheme is usually not optimized on a patient level, and the dose prescription is chosen based on clinical trials and experience. While planning software may include calculators for biological effective dose (BED) and equivalent dose (EQD2), they are not modeling biological effects (such as DNA damage and repair), but rather, they are tools for comparing fractionation schemes. Similarly, for hyperthermia, planning systems for hyperthermia output temperature or specific absorption rate (SAR) maps exist [8] and calculators for equivalent doses have been proposed [9, 10]. Yet, a more profound understanding and modeling of the aforementioned radiobiological effects—DNA damage and repair in this context—would yield a better treatment method. For example, hyperthermia is believed to deactivate DNA repair proteins for a certain amount of time [2]. If radiation-induced damage is introduced during this time window, odds of eliminating the cells increase [11]. Thus, if calibrated correctly, a model involving DNA damage and repair would be able to quantify the duration of this window by simulating the de- and reactivation of said proteins.

In this work, a method is established to calibrate a model that describes the basic dynamics of DNA damage and repair. This model can then be used to extend planning for radiotherapy and hyperthermia to include the biological effects discussed above, i.e., DNA damage and repair: The biological system is modeled in silico, and a parameter search for model calibration is performed with the goal to be able to quantify biological effects for the system of interest. While previous efforts demonstrated feasibility [12], a thorough analysis of the calibration process is provided. This analysis reveals that some parameters remain unidentified. One strength of the method is that it is able to combine calibration results originating from different input data sources (i.e., assays). With this approach, the yet unidentified parameters could be further refined.

Model calibration requires data which can be obtained from number sources which are shown in Figure 1: (1) immunocytochemical assays such as γH2AX, which quantify DNA repair [13]; (2) comet assay, which quantifies the amount of DNA damage [14]; this assay is further discussed in Section 2.3; (3) clonogenic assay, which quantifies clonogenicity [15] and is discussed in Section 2.2. (4) In a clinical setting, DNA damage and repair in tumor cells also affects response evaluation criteria, tumor volume, patient survival, tumor progression and growth rate, etc. Thus, these data (yet quite heterogeneous [7] and thus potentially a poor choice) could, in theory, also be used for model calibration.

These four different options correspond to the four levels illustrated in Figure 1 on the left. On the right, suitable models for these types of readout are depicted. Often, these models merely attempt to replicate some observed readout. For example, the cell survival curves discussed above usually exhibit a parabolic nature in the logarithmic domain [16, 17]. Thus, a quadratic model for $\log(S)$ is often used for the dose-response, without further rationale but just as a method for fitting the existing data. In the past, this approach has been expanded to a linear-quadratic-linear relationship [18], again in a mere attempt to mimic experimentally observed data. Similarly, biostatistical models for comet assay analysis

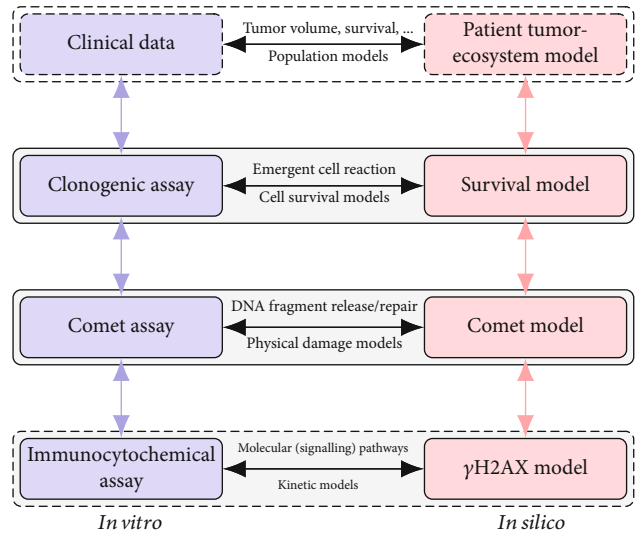

Figure 1: Overview of different assays (clonogenic, comet, and immunocytochemical) capturing different aspects of DNA damage and repair (cell survival, physical damage, and molecular pathways). Each assay (left) provides data that correspond with a suitable model in silico (right). Alternatively, those various aspects can be captured in a single, holistic model from which synthetic assay data are derived for comparison. The latter approach is pursued in this work for emergent cell reactions (clonogenic assay) and physical DNA fragment repair (comet assay).

are able to describe the assay readout but do not model actual DNA damage and repair, let alone in a dynamic fashion [19, 20].

Another class of models go one step further and actually describe underlying molecular principles instead of the mere assay readout. For example, the H2AX phosphorylation discussed above can be modeled using a set of differential equations [21], and the γH2AX readout is derived from the model. This approach is mechanistic in the sense that it is directly modeling the kinetics of the γH2AX pathway and can be seen as syntactic description of molecular mechanisms. Other models including the lethal-potentially-lethal (LPL) model by Curtis [22] and the model by Vassiliev [23] and the Γ-LQ model [24] all follow radiobiologically motivated approaches but do not consider hyperthermia. The AlphaR model [25] takes the effect of hyperthermia into account, albeit for temperatures above 43.5°C which are not the focus of this work. Going one step further, the multi-hit-repair (MHR) model describes radiobiological semantics [26] instead of mechanics. It was used to derive cell survival curves [12] as well as comet assay readouts [27]. In addition to the semantic approach, the MHR model was chosen for this work because it is bioinspired and in the past, its ability was shown to explain many radiobiological phenomena.

2. Materials and Methods

In the following sections, the experimental setup (Section 2.1), the different biological assays (Section 2.2 and 2.3), the model used in this work (Section 2.4), the methods to map the model state to the readout from experimental assays

(Section 2.5), and the calibration method (Section 2.6) are introduced, concluding with a brief section about the software and its availability (Section 2.7).

2.1. Experimental Setup. Hyperthermia and irradiation was performed on cells from the Abrams cell line; they were a kind gift of Prof. Robert Rebhun (University of California, Davis, California, USA). These canine osteosarcoma cells were selected because of their radioresistance (SF2: 0.85) [28], yet they respond well to hyperthermia as a radiosensitizer ($\alpha = 4.6 \times 10^{-3}$ Gy^{-1}, $\beta = 6.4 \times 10^{-3}$ Gy^{-2}, and α/β =0.72 Gy with hyperthermia enhancement-factors (EF) $\alpha_{EF} = 6.7$ and $\beta_{EF} = 1.2$ [29] for hyperthermia performed as indicated below.)

Cells were kept in DMEM at 37°C in a humidified incubator with 5% CO_2 (MCO-18AC-PE, Sanyo, Osaka, Japan). In case of a hyperthermia treatment preceding irradiation, the cells were transferred to another incubator of the same type, set to 42°C, and exposed to a heat-up phase of approx. 40 min, followed by another 60 min of treatment time at the target temperature. The sequence of treatments (hyperthermia followed by irradiation) and the treatment time were chosen to match the clinical practice [30]. To ensure repeatability and quantify thermodynamic effects such as heat transfer and evaporative cooling, incubators were carefully calibrated [29]. In case of an experiment without hyperthermia treatment, the cells remained in the 37°C incubator. Upon completion of the hyperthermia treatment time, the cells were removed from the incubators and irradiated with a 6 MV linear accelerator (Clinac iX, Varian, Palo Alto, USA). Adequate dose build-up and optimal homogeneity of the dose distribution over the irradiation field were ensured by appropriate layers of Plexiglass. Since the irradiation device is also used for regular animal patient treatments, the dose calibration is carried out by a board-certified, qualified medical physicist and is regularly checked with an ionization chamber calibrated at the Swiss Federal Institute of Metrology (METAS).

For logistic reasons (transfer time, setup time, and sequence of irradiation), there was a time-gap of approx. 10 min between the end of the hyperthermia treatment and the beginning of irradiation. Irradiation occurred at doses between 0 Gy and 6 Gy with a dose rate of 600 MU, corresponding to approx. 6 Gy/min. Figure 2 illustrates the timeline of the experiments. It is important to note that while the timeline may suggest otherwise, any experimental procedure (clonogenic and comet assay) discussed below is destructive to the cells. Cells used for a given readout can therefore not be used again for a later or different readout. Thus, the readout originates from different batches of cells.

2.2. Clonogenic Assay. Clonogenic assay is a method to quantify the fraction of cells that survive a treatment, in this case an irradiation event [15]. It works by seeding a number of cells in a dish such that colonies form around these cells due to cell division. After 10 days, the number of colonies are counted and related to the number of cells seeded. If a cell loses clonogenicity due to the treatment, it will not form a clone, while cells which survive the treatment (in the sense of maintaining clonogenicity) will form a colony. The dataset to model clonogenic cell survival in canine osteosarcoma Abrams cells used here was previously published, and the details of the experimental protocol are described in [29].

2.3. Comet Assay. Comet assay is a method to quantify physical DNA damage in individual cells [14] and was performed as follows: approximately 1.5×10^5 Abrams cells were seeded in each well of 6-well plates the day before treatments. Cells were treated with radiation and/or heat and harvested after treatments. For this, trypsin was used, and cells were then resuspended in ice-cold PBS. After centrifugation, cells were counted in each sample and resuspended in their DMEM culture medium complemented with 10% DMSO, in an appropriate volume to reach the concentration of 2×10^5 cells per mL. Samples for cells used in comet assay were then stored at -80°C. Experiments were repeated 3 times.

Cells from every repeated experiment were thawed on the same day and run for comet assay (5 different runs were needed to run all the samples). After thawing and centrifugation, DMSO was quickly removed and ice-cold PBS added. Cells were suspended in molten LMAgarose (CometAssay® LMAgarose, Trevigen) at a ratio of 1/10 (approximately 1500 cells per sample). Cells were embedded in agarose on a glass slide and left in the dark for 10 min at 4°C. Slides were then immersed in a 4°C lysis solution (CometAssay® Lysis Solution, Trevigen) for 1.5 h in a room at 4°C. Slides were then immersed in the electrophoresis running buffer (8 mg/mL NaOH, 2 mL/mL 0.5 M EDTA pH 8, in dH_2O) for 10 min at 4°C in the dark. For electrophoresis, slides were placed in the Trevigen Comet assay tank (CometAssay® Electrophoresis System II, Trevigen) in a cold room, in an exact volume of 850 mL of 4°C electrophoresis solution. Runs lasted 30 min at 21 V and 0.3 A. Care was taken to maintain the same temperature and volume of solution between runs to avoid interrun variability. Slides were finally immersed twice in dH_2O for 10 min each, then in 70% ethanol for 15 min at room temperature. For staining, diluted SYBR Gold (1 : 10 000, SYBR Gold Nucleic Acid Gel Stain, Invitrogen) was then added to each spot of dried agarose including cells, for 15 min at room temperature, in the dark. Slides were rinsed, dried, and stored at room temperature in the dark.

In order to quantify DNA damage, the microscopy image of the stained comets is analysed with the image processing software COMET IV, which computes a value for each cell/comet, indicating the degree of DNA damage. From the damage metrics offered by the software, the relative tail intensity (RTI) was chosen because it provides a linear relationship between the number of DNA strand breaks and the quantified damage [31, 32]—a property highly desired for the data-mapping introduced in Section 2.5. The resulting data was used in a previous publication [27].

2.4. The Multi-Hit-Repair Model. As mentioned in [27], the MHR model [12] is a dynamic population model where cells are assigned to populations $\mathscr{H}_i$ depending on the number of radiation-induced hits (thus the variable name $\mathscr{H}$) they have accumulated. The variable H_i counts the number of cells in population $\mathscr{H}_i$. A hit is defined in this work as a lesion that

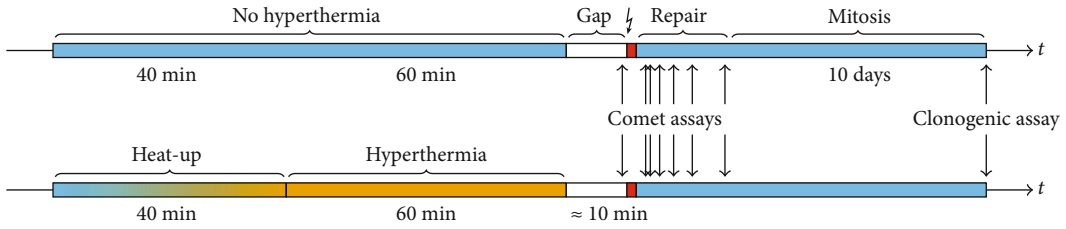

Figure 2: Graphical representation of the experimental treatment. The timeline at the top depicts an experiment without hyperthermia, where cells are kept at 37°C, then transferred to the linear accelerator, irradiated (↯), and then left to grow clones. Comet assays are performed prior to irradiation as well as during the ≈6 h of repair time post irradiation. For clonogenic assay, the clones are fixed and quantified after 10 days. The timeline at the bottom follows the same scheme, but with the additional hyperthermia treatment including the ramp-up to and treatment at 42°C. The time axis is not drawn to scale.

is hindering the cell from mitosis. In consequence, cells with one or more hits cannot undergo mitosis until all the hits are cured by the repair process. Clonogenicity is the ability of cells to form clones, for which mitosis is a prerequisite. Thus, only the cells in $\mathscr{H}_0$ are clonogenic. Figure 3 provides a graphical illustration of the model. Cells can accumulate up to K hits, corresponding to the length of the aforementioned chain. The chain length could be infinite, but for an implementation, K has to be limited. The practical limit for K is chosen such that no congestion at the end of the chain occurs. This criterion is met at $K = 9$; thus, the chain length was chosen accordingly.

During a simulation run, all cells are clonogenic at first; thus, they are assigned to population $\mathscr{H}_0$, counted by the state variable H_0. Hits are induced by radiation with dose rate $R(t)$, which is set to 0 Gy/min at any time except during irradiation. Thus, $R(t)$ is a square pulse that starts at $t = 0$ with an intensity of 6 Gy/min (see Section 2.1); the width of the pulse corresponds to the administered dose. While $R(t) > 0$, cells conceptually travel into the chain as they accumulate hits according to a radiosensitivity parameter α (α in the context of the MHR model is unrelated to α as used in the linear-quadratic model mentioned in Introduction). After irradiation, repair processes inside the cells cure the lesions and thus, cells travel in the opposite direction where they eventually may reach $\mathscr{H}_0$. This repair is governed by the repair rate constant c_r and modulated by a repair function $r(\cdot)$ (see below). Alternatively, the repair processes may fail, leading to the death of a cell. This elimination process occurs at a rate of $c_e H_i$. Thus, the differential equations for population $\mathscr{H}_i$ is

$$\frac{\mathrm{d}H_i}{\mathrm{d}t} = \alpha R(t) H_{i-1} - \alpha R(t) H_i - r(H_i) + r(H_{i+1}) - c_e H_i. \quad (1)$$

DNA repair cannot occur immediately after repair, since radiation not only induces DNA damage but also damages the proteins required for repair. The consequent initial impedance of repair is modeled using the transient biological dose equivalent (TBDE) Γ:

$$\frac{\mathrm{d}\Gamma}{\mathrm{d}t} = R(t) - \gamma\Gamma. \quad (2)$$

Γ decays after irradiation and is used in the repair function to impede repair after irradiation:

$$r(H_i) = c_r \exp(-\mu_\Gamma \Gamma) H_i. \quad (3)$$

Since some small amount of damage is already present before irradiation, initial conditions were chosen to reflect the damage distribution according to Equation (8) in prior work [27]. Alternatively, it can be assumed that no damage is present before irradiation; i.e., $H_0(0) = 1$, $H_{i>0}(0) = 0$, and $\Gamma(0) = 0$. Negligible differences in terms of the model output were found between these two approaches; thus, the latter, simpler approach is used in this work. The full set of equations is given in the supplementary materials; a summary of the model parameters is presented in Table 1. See [12, 26, 27] for the derivation, validation, and further discussion of the MHR model.

For hyperthermia, the two variables Y and Λ are introduced to track the state of active (Y) and inactive (Λ) repair proteins. These variables represent the respective relative amount of repair protein, and thus, they sum up to 1; i.e., $Y + \Lambda = 1$. The activation and inactivation is governed by the following differential equations:

$$\frac{\mathrm{d}Y}{\mathrm{d}t} = -k_1 Y + k_2 \Lambda, \quad (4)$$

$$\frac{\mathrm{d}\Lambda}{\mathrm{d}t} = k_1 Y - k_2 \Lambda. \quad (5)$$

The rate at which inactive repair protein is reactivated, k_2, is assumed to be constant in prior research [12, 26, 27, 30] and throughout this work. While the reactivation may be temperature-dependent, the authors are unaware of any research supporting that hypothesis, thus, following the principle of assuming simple circumstances whenever possible and, k_2 is not a function of temperature.

The inactivation of repair protein, however, is temperature-dependent [2, 33, 34]. The rate at which this occurs, k_1, incorporates the Arrhenius law [35] as follows:

$$k_1 = a \cdot 10^{-3} \exp\left(\frac{E_a}{\overline{R}(273.16 + 37)} - \frac{E_a}{\overline{R}(273.16 + T)}\right). \quad (6)$$

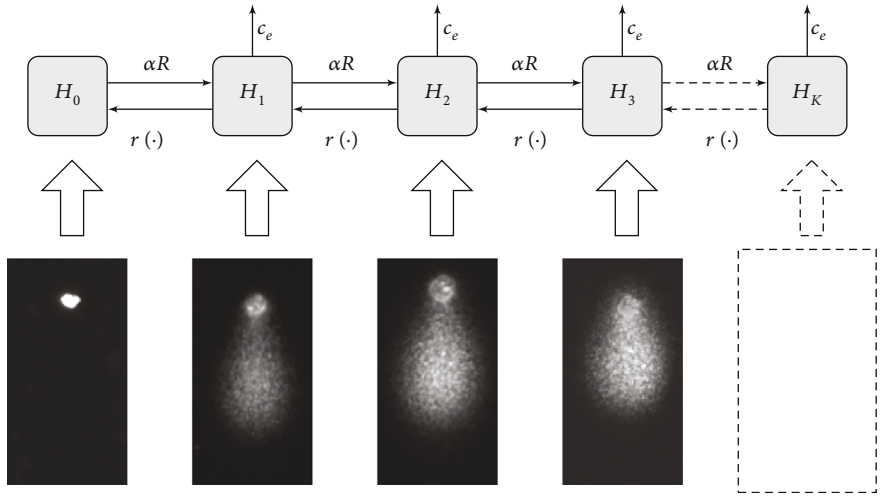

Figure 3: High-level illustration of the MHR model [27]. The boxes depict the chain structure with the populations H_i; the arrows denote how cells accumulate hits (to the right), undergo cell death (to the top), or undergo repair (to the left). Below the chain, comet assay pictures conceptually illustrate how comets with increasingly high relative tail intensities are mapped to populations with increasingly high numbers of hits.

Table 1: Summary of model parameters including their search space. The last column indicates the result of parameter search (see Section 2.6).

Parameter	Description	Search space
α	Radiosensitivity (Gy^{-1})	$[0.17\,;2]$
c_r	Repair rate constant (h^{-1})	$[0\,;10]$
c_e	Elimination rate constant (h^{-1})	$[0\,;10]$
μ_Γ	TBDE weighting factor (Gy^{-1})	$[0\,;10]$
γ	TBDE rate constant (h^{-1})	$[0\,;10]$
a	Repair protein deactivation rate (h^{-1})	$[0\,;2]$
k_2	Repair protein activation rate (h^{-1})	$[0\,;0.1]$
μ_Λ	Hyperthermia weighing factor	$[0\,;5]$

The parameter a is introduced for numeric reasons. $\bar{R} = 8.314\ \mathrm{J{\cdot}K^{-1}\cdot mol^{-1}}$ is the gas constant, and $E_a = 1528\ \mathrm{kJ{\cdot}mol^{-1}}$ is the activation energy as published in the literature [12, 36]. It is important to note that E_a may be cell-line specific; thus, the choice of E_a should be revisited in the future once such data is available for the Abrams cell line used here. It is easy to show that the equilibrium of Equations (4) and (5) are $Y \approx 1$ and $\Lambda \approx 0$, respectively, for $T = 37\,^\circ\mathrm{C}$. Those values therefore serve as initial conditions as it is assumed that this equilibrium is reached prior to the hyperthermia treatment.

The repair function is extended to modulate the DNA repair rate with the amount of inactive repair proteins:

$$r(H_i) = c_r \exp\left(-\mu_\Gamma \Gamma - \mu_\Lambda \Lambda\right) H_i. \tag{7}$$

This entails that the rate of repair is reduced both in the presence of inactive repair protein due to thermal effects (Λ) and after irradiation when the TBDE is high (Γ).

A temperature of $T = 42^\circ\mathrm{C}$ is set during the hyperthermia treatment. Before and after the treatment, the temperature is set to $T = 37^\circ\mathrm{C}$.

2.5. Model/Readout Mapping. Since the MHR model is describing radiobiological processes instead of assay readouts, methods need to be implemented to map the model to such readouts. For clonogenic assay, this is relatively straight forward and was introduced in [12]: $\mathscr{H}_0$ is tracking clonogenic cells by definition; thus, the surviving number of cells is readily available in H_0. Survival S is therefore found by evaluating H_0 at the end of the simulation, provided the simulation time is chosen such that the repair process has completed at the end of the simulation.

The mapping to comet data is somewhat more elaborate and was introduced in [27]: The comet readout at a given point in time consists of the quantification of DNA damage in a number of (typically $m = 100$) cells. Depending on the amount of DNA damage, each cell is assigned to a bin h_i: the first bin h_0 tracks the cells with little to no damage and the second bin h_1 tracks cells with more damage, etc. The cell count in each bin and population is normalized such that

$$\sum_{i=0}^{K} \tilde{h}_i = \sum_{i=0}^{K} \tilde{H}_i = 1. \tag{8}$$

Finally, the relative bins $\tilde{h}_i$ can be mapped directly to $\tilde{H}_i$ of the MHR model.

In Section 2.4, a hit was defined as an impact on the cell that bars it from mitosis until cured. The correct mapping between physical DNA damage as reported by the comet assay and the model populations $\mathscr{H}_i$ presumes knowledge about how much physical DNA damage constitutes one hit. In other words, the relative tail intensities quantifying DNA damage must be scaled prior to the mapping to H_i to maintain the semantics implied by the MHR model (i.e., the

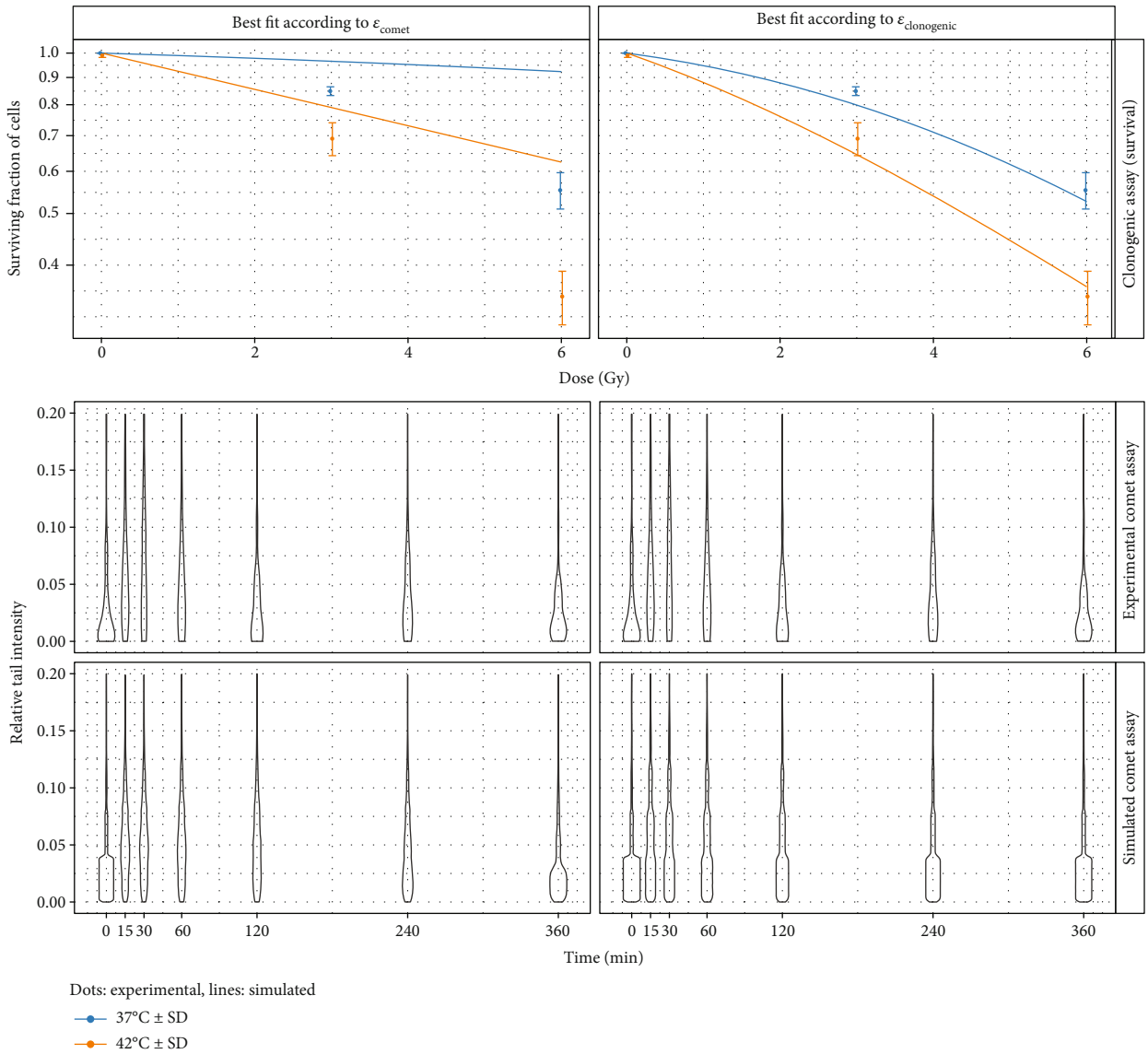

Figure 4: Top: cell survival curves after parameter search with Equation (11) as objective function: $\alpha = 0.19$, $c_r = 0.22$, $c_e = 0.00$, $\mu_\Gamma = 0.00$, $\gamma = 3.80$, $a = 1.00$, $k_2 = 0.01$, and $\mu_\Lambda = 3.50$ (left); $\alpha = 0.23$, $c_r = 5.80$, $c_e = 0.14$, $\mu_\Gamma = 1.62$, $\gamma = 0.26$, $a = 0.31$, $k_2 = 1.3 \cdot 10^{-4}$, and $\mu_\Lambda = 4.67$ (right). The plots at the left result from a parameter search where clonogenic assay data is not considered at all (i.e., comet data only as published and discussed in [27]). The plots at the right also show results from a parameter search from comet data alone, but the parameter set producing the best clonogenic cell survival curve (according to Equation (10)) is shown. Since information from clonogenic assay was used, the left plot exhibits a very poor prediction of experimental data ($\varepsilon_{clonogenic} = 0.12$). This shows that the data from comet assay alone do not capture all information required for a successful parameter search. However, some parameter sets are viable—the plot at the right does not suffer from this issue ($\varepsilon_{clonogenic} = 4.8 \cdot 10^{-4}$)—suggesting the use of a joint approach where data from both assays is used. Bottom: experimental and synthetic comet readout for the same parameter sets.

definition of a hit). In [27], the correct scaling factor was unknown, and thus, tail intensities between 0 and 4% were mapped to $\mathcal{H}_0$ arbitrarily (as discussed there, the model can still be used with a wrong scaling factor, but the parameters may lose the meaning they were originally designed for). In this work, the scaling factor is not fixed to a single, convenient value arbitrarily. Instead, the procedure is repeated with different scaling factors within a sensible range. In order to achieve this, the scaling is formalized by the variable σ which denotes the largest tail intensity that is still mapped to $\mathcal{H}_0$. Hence, $\sigma = 0.04$ in the above example.

Interestingly, the method failed to reproduce experimental comet data for small values of σ. For large values of σ, the resulting α parameter values were in violation of the lower bound stipulated by Equation (9) (see Figure S1). Only a small region around $\sigma = 0.03$ was free from these issues; thus, $\sigma = 0.03$ was used.

2.6. Approximate Bayesian Computation. Approximate Bayesian computation (ABC) [37] is used to estimate distributions of model parameters. The method works as follows:

for each parameter, the range of biologically meaningful parameter values is estimated. For example, with $\gamma = 10\ \mathrm{h}^{-1}$ (the upper boundary of this parameter), repair proteins reactivate very quickly from the irradiation event; the repair probability recovers to 94% 30 min post irradiation. This is unrealistically high given the typical delays observed experimentally (see Figure 4 and [38]). Since no prior information is available on a given parameter values' positions within the search space $[a\,;b]$, uniform prior distributions with boundaries a and b, $\mathcal{U}[a\,;b]$, are chosen. The boundaries are listed in Table 1 for each parameter. Determining the lower bound on α presents a special case: it is easy to show that in the absence of any repair (i.e., $r(H_1) = 0$),

$$H_0(t) = \exp\,(-\alpha R t), \tag{9}$$

for the duration of irradiation. After irradiation, $R = 0$, and thus, $H_0(t)$ remains constant. Because $H_0(t)$ is mapped to the fraction of surviving cells (see Section 2.5), a lower bound for α can be established by solving Equation (9) after substituting $H_0(t)$ for S as reported in the clonogenic assay and setting t to the point in time at which irradiation ends.

At the beginning of the parameter search, n sets of parameters are initialized by drawing from the prior distributions. Predictions are made by running the model in a forward fashion, extracting the predicted readout as described in Section 2.5 and comparing it to experimental data. This yields an error ε according to Equations (10) and (11) (see below).

In each iteration of the search, the parameters are perturbed; the new parameter values are kept if ε decreases and are discarded otherwise. In a simulated annealing fashion [39], the amount of perturbation is gradually decreased as the search progresses. A cut-off value of $\varepsilon = 10^{-2}$ was chosen. In the end, n sets of parameters are left; all of which provide a satisfactory error. In this work, $n = 1000$ was chosen with 250 iterations.

The objective function for the parameter search with cell survival data is

$$\varepsilon_{\text{clonogenic}} = \sum_{\mathrm{D}} \left(\log\,(S_D) - \log\,(S\wedge_D)\right)^2, \tag{10}$$

for the radiation doses D, the experimentally obtained surviving fraction of cells S_D, and the predicted surviving fraction of cells $\widehat{S}$.

Similarly, the objective function for the parameter search with comet data is

$$\varepsilon_{\text{comet}} = \sum_{t>0} \sum_{i=0}^{K} \left(\tilde{h}_i^{(t)} - \tilde{H}_i(t)\right)^2, \tag{11}$$

for time point t, normalized population $\tilde{H}_i$, and normalized comet readout $\tilde{h}_i$ as defined in Equation (8). A combined calibration was attempted with a combined objective function (see discussion in Section 4).

2.7. Software. The methods discussed above were implemented in python (version 3.5.2) using the abcpy module [40] for ABC (version 0.5.3). R version 3.6.0 was used to create the plots; the code and data are available online (https://github.engineering.zhaw.ch/weyl/synthetic_comet). The software can be configured to use either input data from clonogenic assay or input data from comet assay. Depending on this selection, the corresponding objective function $\varepsilon_{\text{clonogenic}}$ or $\varepsilon_{\text{comet}}$ is used. The results shown in Figure 5 are obtained with the software running on clonogenic mode, i.e., evaluating $\varepsilon_{\text{clonogenic}}$, while those in Figure 4 are obtained with the software running in comet mode, i.e., evaluating $\varepsilon_{\text{comet}}$.

3. Results

Two model outputs for cell survival are shown at the top of Figure 5, as produced by the software running in clonogenic mode. The examples were chosen according to similar $\varepsilon_{\text{clonogenic}}$: for both instances, $\varepsilon_{\text{clonogenic}} \approx 2.5 \times 10^{-3}$. Experimentally, it would be very challenging (if not impossible) to discriminate between the two curves. Yet, the parameters and the dynamics shown at the bottom are very different from each other: in the left case, most hits have vanished after 2 h, while the same requires 4 h in the right case.

With the software running in comet mode (i.e., minimizing $\varepsilon_{\text{comet}}$), results are shown in Figure 4. The data on the left represents a random pick from the parameter result set and produces a cell survival curve very different from cell survival found experimentally ($\varepsilon_{\text{clonogenic}}$=0.12). The ones on the right is the curve with the lowest error found in the set ($\varepsilon_{\text{clonogenic}} = 4.8 \cdot 10^{-4}$).

Figure 6 shows a histogram panel of the parameters unrelated to hyperthermia (see Figure S2 for parameters a, k_2, and μ_Λ). In the top row, parameters from the software in clonogenic mode are shown while in the middle row, parameters from the software in comet mode are shown. The bottom row shows the joint distribution, calculated from the previous two rows. Generally, values for α and c_e are centered around one or two peaks, while, e.g., μ_Γ is more uniformly distributed in the comet case, but clonogenic assay data suggests that the parameter peaks at low values.

In addition to joining the two posterior distributions for each parameter, a calibration was attempted where the two objective functions were combined with a weighting factor ξ:

$$\varepsilon_{\text{combined}} = \varepsilon_{\text{clonogenic}} + \xi\varepsilon_{\text{comet}} \tag{12}$$

In order not to prefer any assay source from the other, errors from the previous single-assay runs were used to select $\xi = 1.68 \times 10^{-3}$ such that the two terms are of the same order of magnitude. This attempt failed; the ABC solver never left its seeding state (see discussion in Section 4).

4. Discussion

The results shown in the previous section clearly call for a combined approach, where both clonogenic assay and comet assay data are used as sources of information for parameter search. However, the traditional approach of combining two objective functions failed. This is because in the seeding

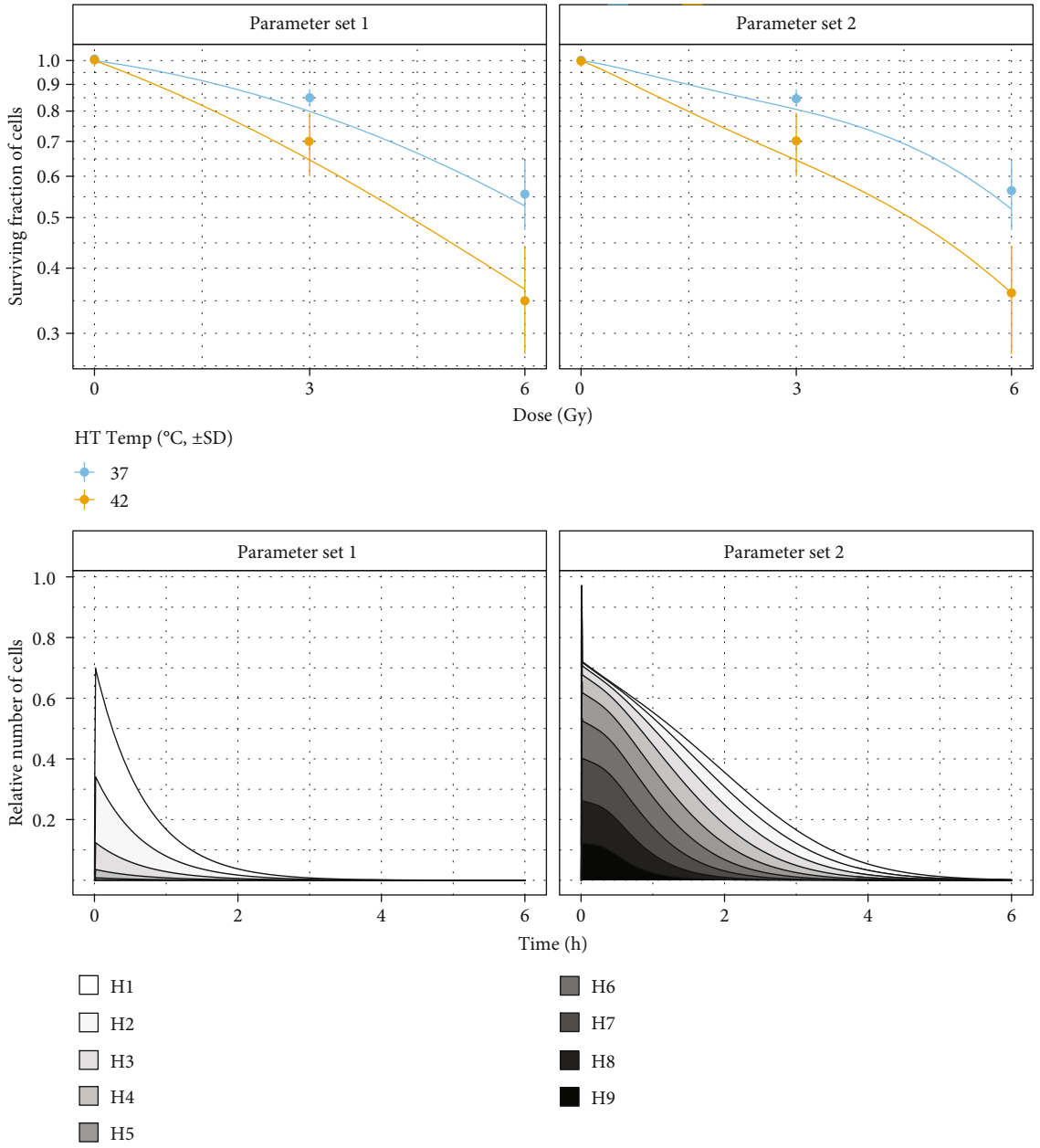

FIGURE 5: Top: cell survival curves for two different sets of parameters after parameter search with clonogenic assay data. Two sets with similar errors were chosen ($\varepsilon_{\text{clonogenic}} = 2.5 \cdot 10^{-3}$); the curves match experimental data (dots) relatively well and are very similar albeit having vastly different parameter values. Bottom: corresponding H_i values in time (no hyperthermia). While the two parameter sets produce similar survival curves, the dynamics of repair are very different. Because clonogenic assay captures only the state after repair has completed, no information about these dynamics is in the data. The parameters are $\alpha = 1.32$, $c_r = 6.89$, $c_e = 0.25$, $\mu_\Gamma = 1.60$, $\gamma = 6.75$, $a = 0.92$, $k_2 = 0.048$, and $\mu_\Lambda = 1.39$ (set 1) and $\alpha = 0.20$, $c_r = 4.58$, $c_e = 1.31$, $\mu_\Gamma = 0.25$, $\gamma = 0.20$, $a = 0.38$, $k_2 = 0.039$, and $\mu_\Lambda = 3.20$ (set 2).

state, ABC with simulated annealing rejects samples from the prior that are above a certain threshold (values up to $\varepsilon = 10$ were tried). Since it is difficult to find parameters that satisfy both objective functions, the seeding state never completed. Thus, the computationally much lighter approach with joint posteriors is proposed, allowing for additional flexibility in combining further calibration results.

The results in Figure 5 reveal that survival curves lack sufficient information for MHR model calibration. This is hardly surprising, as it was argued before that the clonogenic assay captures information very distant from the process that is being modeled. On a side-note, any attempt to calibrate a model with 8 parameters from 5 data points is likely going to fail, which is yet another reason to include additional data sources. However, even with this little information, the top row in Figure 6 reveals regions of interest for some parameters, e.g., for α and c_e. On a related note, the resulting posterior distributions for α and c_e are bimodal. This is an

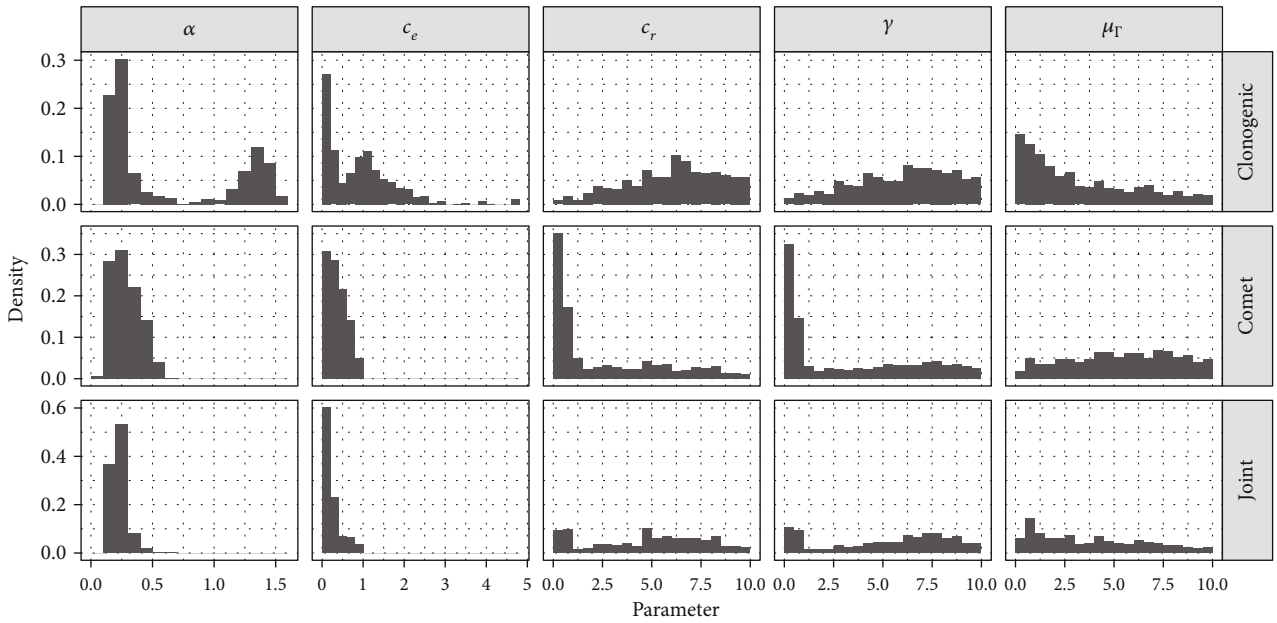

Figure 6: Histograms of parameter values after calibration with the software set to different modes, and at the bottom, the joint distribution obtained by combining the two posterior sets is shown. Of $n = 1000$ parameter sets, the 75% with the smallest error $\varepsilon_{\text{clonogenic}}$ is used to restrict outliers.

important finding that is concealed by a method aiming at point-estimates, such as differential evolution one used in [27]. Indeed for the α value, one peak of the histogram corresponds to the range of parameters found in [12], while the other peak corresponds to the range of parameters found in [27]. Interestingly, these two regimes also correspond to the two instances depicted in Figure 5.

Based on the aforementioned rationale, one may assume that the use of comet assay readouts would cure these issues. However, Figure 4 demonstrates that this is not the case. Otherwise, any parameter set would yield an adequate cell survival curve. Discussing potential explanations for this observation is critical since the resulting conclusions govern the choice of further data to address the open issues: for quantification of the damage, the relative tail intensity is assessed for approx. 100 cells per assay. This quantification does not discriminate between cells that have a chance to reach $\mathcal{H}_0$, cells that have already initiated apoptosis and will never reach $\mathcal{H}_0$, and cells that are on the brink of death for other reasons. In fact, the quantification may even contain cells that are already dead but still have DNA that is visible in the microscopy image. However, the ability to reach $\mathcal{H}_0$ is essential for producing a survival curve from the model. Thus, a possible explanation for the inability to achieve successful model calibration from comet assay readout alone could be that the readout does not carry sufficient information about the ability to reach $\mathcal{H}_0$. Furthermore, dead cells that have degraded so far as to not have any quantifiable DNA whatsoever would not be considered for comet assay, and the normalization of the 100 cells to a relative histogram would mostly masquerade their existence: the only way for dead cells to influence the results is in the ratio $\tilde{h}_0/\sum_{i\neq 0}\tilde{h}_i$, since a surviving cell would contribute to H_0 (thus increasing H_0), but if the same cell had died, it would not contribute to any H_i (thus increasing $\tilde{H}_i$ for $i \neq 0$).

For the parameters c_r, γ, and μ_Γ (Figure 6) as well as the parameters related to hyperthermia (Figure S2), uniform posterior distributions are obtained. The method thus reveals that more input data is required to identify these parameters. Parameters γ and μ_Γ relate to a transient repair inability due to the irradiation event. From Figure 4, it can be seen that this effect vanishes approx. 30 min. after irradiation. Thus, further data within that time frame could yield better estimates for those parameters. c_r could be identified by running a series of clonogenic assays at various dose rates. At low dose rates, irradiation would not be considered as an event but have a finite duration and repair may start already during irradiation. Such dose-rate-dependency was shown in the past to be reproduced by the MHR model [12], and the rate of repair c_r could become identifiable. The hyperthermia parameters could be refined with data from a study with varying time-gaps. Such data from clonogenic assay has been publishedI [9] but not from comet assay and with different cell lines. As mentioned in Introduction, assessing the repair-protein reactivation rate constant k_2 would be of great clinical use, as it would allow a better assessment about tolerable time-gaps (and variation thereof) between irradiation and hyperthermia. Since the order of the two treatments (i.e., hyperthermia prior to versus after irradiation) was shown to have minimal effect on cell survival [9], additional input data in this regard would likely not improve the calibration results. Investigating more cell lines would reveal which parameters may vary by how much between subjects.

Clonogenic cell survival and comet assay measurements were shown to be repeatable [14, 29]; thus, it is reasonable to expect repeatable results from patient biopsies [38]. This

would allow for a per-patient calibration, e.g., to improve the treatment plan on a per-patient basis. As mentioned in the previous paragraph, such an endeavour would require data from appropriate sources to identify the relevant parameters, rather than just more amounts of data.

In case the model cannot be calibrated at all despite these efforts, it could be simplified, for example by replacing the TBDE Γ with a fixed window of no repair after irradiation, removing the parameters μ_Γ and γ. Alternatively, it is conceivable to split the process at the time of the irradiation, yielding a hyperthermia process that sets up the initial conditions for a subsequent DNA damage and repair process. Splitting the model in this way could yield closed-form solutions or approximations thereof for some state variables, paving the way for a much simpler calibration strategy.

The model and the strategy presented in this work have a number of potential limitations. First, the model does not incorporate any mitosis, which occurs without doubt in $\mathcal{H}_0$ until the cells are fixed and the clonogenic assay is performed. However, one can argue that for a given cell line, any mitosis would occur at a fixed rate. While the number of cells would increase, their ratio would remain the same. Because the clonogenic cell survival assays used in this work are normalized, mitosis cancels out. Some cells may, however die only after a few cell cycles. This falls in the gap between the last comet assay and the point in time when clonogenic assay is performed and is not modeled in the MHR model. Second, the model does not incorporate any effects of direct cytotoxicity, i.e. thermal cell-killing. This is alleviated by the fact that such direct cytotoxicity was not observed in any of the control experiments performed with hyperthermia alone [29]. Third, the model does not correctly describe inhibition of DNA repair proteins above a temperature threshold of 42.5°C–43°C, since those proteins are believed to enter a different regime above that threshold [35]. While this is a limitation, it does not affect the work presented here since the highest temperature applied *in vivo* and in silico was 42°C.

5. Conclusions

This work demonstrates that a holistic approach is necessary to calibrate the MHR model parameters. Relying on clonogenic assay data or comet assay data alone, as it has been done in the past, proved to be insufficient to establish unambiguous model parameters. Even with this combined approach, some parameters remain unidentified. However, the ABC method has the advantage of joining existing posterior distributions with distributions obtained from calibration runs with new input data. This ability is critical since model calibration with ABC is, despite all its advantages, very slow. Combining posterior distributions from ABC, however, is fast. Following this approach, data from different assays can be combined in a modular fashion without the need of rerunning the full calibration.

While the application of the method presented is radiotherapy, hyperthermia, and treatment planning, the method presented here addresses a more general problem; thus, many other instances exist where the application of this method would be of value.

Data Availability

The data are available online (https://github.engineering.zhaw.ch/weyl/synthetic_comet) along with the software code required to perform the analyses shown in this work.

Conflicts of Interest

The authors declare that there are no conflicts of interest.

Acknowledgments

This work was supported by the Swiss National Foundation (grant number 320030_163435)—Stephan Scheidegger, Carla Rohrer Bley. This work was financially supported by a grant from the Marie-Louise von Muralt-Stiftung für Kleintiere.

Supplementary Materials

The supplementary materials contain (A) the full equation system of the multi-hit-repair (MHR) model and (B) supplementary figures with additional parameter histograms. *(Supplementary Materials)*

References

[1] N. van den Tempel, M. R. Horsman, and R. Kanaar, "Improving efficacy of hyperthermia in oncology by exploiting biological mechanisms," *International Journal of Hyperthermia*, vol. 32, no. 4, pp. 446–454, 2016.

[2] B. Eppink, P. M. Krawczyk, J. Stap, and R. Kanaar, "Hyperthermia-induced dna repair deficiency suggests novel therapeutic anti-cancer strategies," *International Journal of Hyperthermi*, vol. 28, no. 6, pp. 509–517, 2012.

[3] G. Iliakis, W. Wu, and M. Wang, "DNA double strand break repair inhibition as a cause of heat radiosensitization: Re-evaluation considering backup pathways of NHEJ," *International Journal of Hyperthermia*, vol. 24, no. 1, pp. 17–29, 2009.

[4] N. van den Tempel, H. Odijk, N. van Holthe et al., "Heat-induced BRCA2 degradation in human tumours provides rationale for hyperthermia-PARP-inhibitor combination therapies," *International Journal of Hyperthermia*, vol. 34, no. 4, pp. 407–414, 2017.

[5] P. M. Krawczyk, B. Eppink, J. Essers et al., "Mild hyperthermia inhibits homologous recombination, induces BRCA2 degradation, and sensitizes cancer cells to poly (ADP-ribose) polymerase-1 inhibition," *Proceedings of the National Academy of Sciences*, vol. 108, no. 24, pp. 9851–9856, 2011.

[6] I. Fotina, P. Winkler, T. Künzler, J. Reiterer, I. Simmat, and D. Georg, "Advanced kernel methods vs. Monte Carlo-based dose calculation for high energy photon beams," *Radiotherapy and Oncology*, vol. 93, no. 3, pp. 645–653, 2009.

[7] D. Thorwarth, "Biologically adapted radiation therapy," *Zeitschrift für Medizinische Physik*, vol. 28, no. 3, pp. 177–183, 2018.

[8] H. P. Kok, P. Wust, P. R. Stauffer, F. Bardati, G. C. van Rhoon, and J. Crezee, "Current state of the art of regional hyperthermia treatment planning: a review," *Radiation Oncology*, vol. 10, no. 1, 2015.

[9] C. M. van Leeuwen, A. L. Oei, R. ten Cate et al., "Measurement and analysis of the impact of time-interval, temperature and radiation dose on tumour cell survival and its application in thermoradiotherapy plan evaluation," *International Journal of Hyperthermia*, vol. 34, no. 1, pp. 30–38, 2017.

[10] C. M. van Leeuwen, J. Crezee, A. L. Oei et al., "3D radiobiological evaluation of combined radiotherapy and hyperthermia treatments," *International Journal of Hyperthermia*, vol. 33, no. 2, pp. 160–169, 2016.

[11] S. A. Sapareto, L. E. Hopwood, and W. C. Dewey, "Combined Effects of X Irradiation and Hyperthermia on CHO Cells for Various Temperatures and Orders of Application," *Radiation Research*, vol. 73, no. 2, pp. 221–233, 1978.

[12] S. Scheidegger, H. U. Fuchs, K. Zaugg, S. Bodis, and R. M. Füchslin, "Using State Variables to Model the Response of Tumour Cells to Radiation and Heat: A Novel Multi-Hit-Repair Approach," *Computational and Mathematical Methods in Medicine*, vol. 2013, Article ID 587543, 15 pages, 2013.

[13] L. J. Kuo and L.-X. Yang, "Gamma-H2AX - A Novel Biomarker for DNA Double-strand Breaks," *In Vivo*, vol. 22, no. 3, pp. 305–309, 2008.

[14] P. L. Olive and J. P. Banáth, "The comet assay: a method to measure DNA damage in individual cells," *Nature Protocols*, vol. 1, no. 1, pp. 23–29, 2006.

[15] N. A. P. Franken, H. M. Rodermond, J. Stap, J. Haveman, and C. van Bree, "Clonogenic assay of cells _in vitro_," *Nature Protocols*, vol. 1, no. 5, pp. 2315–2319, 2006.

[16] D. E. Lea, *Actions of radiations on living cells*, Cambridge University Press, Cambridge, 1946.

[17] R. G. Dale, "The application of the linear-quadratic dose-effect equation to fractionated and protracted radiotherapy," *The British Journal of Radiology*, vol. 58, no. 690, pp. 515–528, 1985.

[18] M. Guerrero and X. A. Li, "Extending the linear–quadratic model for large fraction doses pertinent to stereotactic radiotherapy," *Physics in Medicine & Biology*, vol. 49, no. 20, pp. 4825–4835, 2004.

[19] P. MÃ¸ller and S. Loft, "Statistical analysis of comet assay results," *Frontiers in Genetics*, vol. 5, p. 292, 2014.

[20] D. P. Lovell and T. Omori, "Statistical issues in the use of the comet assay," *Mutagenesis*, vol. 23, no. 3, pp. 171–182, 2008.

[21] L. Bodgi and N. Foray, "The nucleo-shuttling of the atm protein as a basis for a novel theory of radiation response: resolution of the linear-quadratic model∗," *International Journal of Radiation Biology*, vol. 92, no. 3, pp. 117–131, 2016.

[22] S. B. Curtis, "Lethal and Potentially Lethal Lesions Induced by Radiation — A Unified Repair Model," *Radiation Research*, vol. 106, no. 2, pp. 252–270, 1986.

[23] O. N. Vassiliev, "Formulation of the Multi-Hit Model With a Non-Poisson Distribution of Hits," *International Journal of Radiation Oncology • Biology • Physics*, vol. 83, no. 4, pp. 1311–1316, 2012.

[24] S. Scheidegger, G. Lutters, and S. Bodis, "Eine LQ-basierte kinetische Modellformulierung zur Untersuchung der Dynamik des Therapie-Ansprechverhaltens von Tumoren in vivo," *Zeitschrift für Medizinische Physik*, vol. 21, no. 3, pp. 164–173, 2011.

[25] S. C. Brüningk, J. Ijaz, I. Rivens, S. Nill, G. ter Haar, and U. Oelfke, "A comprehensive model for heat-induced radiosensitisation," *International Journal of Hyperthermia*, vol. 34, no. 4, pp. 392–402, 2017.

[26] S. Scheidegger, H. U. Fuchs, and R. M. Füchslin, "Computational methods for exploring the dynamics of cancer: the potential of state variables for description of complex biological systems," in *Proceedings of the international symposium on nonlinear theory and its applications : NOLTA2014*, pp. 168–171, Luzern, Switzerland, 2014.

[27] M. S. Weyland, P. Thumser-Henner, C. R. Bley et al., "Dynamic DNA Damage and Repair Modeling: Bridging the Gap Between Experimental Damage Readout and Model Structure," in *Communications in Computer and Information Science*, pp. 127–137, Springer, 2019.

[28] J. Maeda, C. E. Froning, C. A. Brents, B. J. Rose, D. H. Thamm, and T. A. Kato, "Intrinsic Radiosensitivity and Cellular Characterization of 27 Canine Cancer Cell Lines," *PloS one*, vol. 11, no. 6, article e0156689, 2016.

[29] K. J. Nytko, P. Thumser-Henner, M. S. Weyland, S. Scheidegger, and C. R. Bley, "Cell line-specific efficacy of thermoradiotherapy in human and canine cancer cells in vitro," *PloS one*, vol. 14, no. 5, article e0216744, 2019.

[30] S. Dressel, M.-C. Gosselin, M. H. Capstick et al., "Novel hyperthermia applicator system allows adaptive treatment planning: Preliminary clinical results in tumour-bearing animals," *Veterinary and Comparative Oncology*, vol. 16, no. 2, pp. 202–213, 2018.

[31] Y. Wang, C. Xu, L. Du et al., "Evaluation of the Comet Assay for Assessing the Dose-Response Relationship of DNA Damage Induced by Ionizing Radiation," *International Journal of Molecular Sciences*, vol. 14, no. 11, pp. 22449–22461, 2013.

[32] T. S. Kumaravel and A. N. Jha, "Reliable comet assay measurements for detecting dna damage induced by ionising radiation and chemicals," *Mutation Research/Genetic Toxicology and Environmental Mutagenesis*, vol. 605, no. 1-2, pp. 7–16, 2006.

[33] P. M. Corry, S. Robinson, and S. Getz, "Hyperthermic Effects on DNA Repair Mechanisms," *Radiology*, vol. 123, no. 2, pp. 475–482, 1977.

[34] A. L. Oei, L. E. M. Vriend, J. Crezee, N. A. P. Franken, and P. M. Krawczyk, "Effects of hyperthermia on DNA repair pathways: one treatment to inhibit them all," *Radiation Oncology*, vol. 10, no. 1, 2015.

[35] S. A. Sapareto and W. C. Dewey, "Thermal dose determination in cancer therapy," *International Journal of Radiation Oncology • Biology • Physics*, vol. 10, no. 6, pp. 787–800, 1984.

[36] E. K. Rofstad and T. Brustad, "Arrhenius analysis of the heat response *in vivo* and *in vitro* of human melanoma xenografts," *International Journal of Hyperthermia*, vol. 2, no. 4, pp. 359–368, 2009.

[37] J.-M. Marin, P. Pudlo, C. P. Robert, and R. J. Ryder, "Approximate Bayesian computational methods," *Statistics and Computing*, vol. 22, no. 6, pp. 1167–1180, 2012.

[38] N. Schulz, H. Chaachouay, K. Nytko et al., "Dynamic In Vivo Profiling of DNA Damage and Repair after Radiotherapy Using Canine Patients as a Model," *International Journal of Molecular Sciences*, vol. 18, no. 6, p. 1176, 2017.

[39] C. Albert, H. R. Künsch, and A. Scheidegger, "A simulated annealing approach to approximate bayes computations," *Statistics and Computing*, vol. 25, no. 6, pp. 1217–1232, 2015.

[40] R. Dutta, M. Schoengens, J.-P. Onnela, and A. Mira, "ABCpy: A User-Friendly, Extensible, and Parallel Library for Approximate Bayesian Computation," in *Proceedings of the Platform for Advanced Scientific Computing Conference (PASC '17)*, vol. 8, pp. 1–9, New York, NY, USA, 2017.

Hindawi
Computational and Mathematical Methods in Medicine
Volume 2020, Article ID 3267949, 5 pages
https://doi.org/10.1155/2020/3267949

Research Article

Identifying Methamphetamine Dependence Using Regional Homogeneity in BOLD Signals

Hufei Yu,[1,2] **Shucai Huang**,[1,3,4] **Xiaojie Zhang**,[1,3] **Qiuping Huang**,[1,3] **Jun Liu**,[5] **Hongxian Chen**,[1,3] **and Yan Tang**[2]

[1]*National Clinical Research Center for Mental Disorders, and Department of Psychiatry, The Second Xiangya Hospital of Central South University, Changsha, Hunan 410000, China*
[2]*School of Computer Science and Engineering, Central South University, Changsha, Hunan 410000, China*
[3]*Institute of Mental Health of the Second Xiangya Hospital, Central South University, Chinese National Technology Institute on Mental Disorders, Hunan Key Laboratory of Psychiatry and Mental Health, Hunan Medical Center for Mental Health, Changsha, Hunan 410000, China*
[4]*The Fourth People's Hospital of Wuhu, Wuhu, Anhui 214000, China*
[5]*Department of Medical Imaging, The Second Xiangya Hospital, Central South University, Changsha, Hunan 410000, China*

Correspondence should be addressed to Hongxian Chen; shenhx2018@csu.edu.cn and Yan Tang; tangyan@csu.edu.cn

Received 4 September 2019; Revised 23 April 2020; Accepted 11 May 2020; Published 28 May 2020

Guest Editor: Adam Konefal

Methamphetamine is a highly addictive drug of abuse, which will cause a series of abnormal consequences mentally and physically. This paper is aimed at studying whether the abnormalities of regional homogeneity (ReHo) could be effective features to distinguish individuals with methamphetamine dependence (MAD) from control subjects using machine-learning methods. We made use of resting-state fMRI to measure the regional homogeneity of 41 individuals with MAD and 42 age- and sex-matched control subjects and found that compared with control subjects, individuals with MAD have lower ReHo values in the right medial superior frontal gyrus but higher ReHo values in the right temporal inferior fusiform. In addition, AdaBoost classifier, a pretty effective ensemble learning of machine learning, was employed to classify individuals with MAD from control subjects with abnormal ReHo values. By utilizing the leave-one-out cross-validation method, we got the accuracy more than 84.3%, which means we can almost distinguish individuals with MAD from the control subjects in ReHo values via machine-learning approaches. In a word, our research results suggested that the AdaBoost classifier-neuroimaging approach may be a promising way to find whether a person has been addicted to methamphetamine, and also, this paper shows that resting-state fMRI should be considered as a biomarker, a noninvasive and effective assistant tool for evaluating MAD.

1. Introduction

Methamphetamine is a type of synthetic stimulant that often appears white or colorless, and chronic overuse may result in dependence. There are many researchers claimed that chronic overuse of methamphetamine brings about adverse physical reactions and severe psychiatric symptoms, such as depressive disorder and dysthymic disorder [1, 2], mental disease [3], and cognitive deficits [4–6], which may attribute to the reduction of dopamine transporter density that persists after use ceases [7, 8]. Currently, the clinical diagnosis of individuals with methamphetamine dependence (MAD) is based on the abnormal presence of MA users, self-reported symptoms that are subject to their own bias. There is a lack of validated biomarkers that are highly relative to MAD. So, we proposed a machine-learning-based method that may be an effective aided diagnosis system for MAD.

Based on the blood oxygen level-dependent (BOLD) signal, resting-state functional magnetic resonance imaging (rs-fMRI) is a useful method for the research of brain activity. ReHo is a promising method of the study of resting-state fMRI, which has been successfully used for a volume of researches of neurological diseases, such as the research of antisocial personality disorder [9], schizophrenia [10], and

depression [11]. Hence, in this study, we utilized ReHo to find the differences between individuals with MAD and control subjects, and using the abnormal ReHo value in subjects, we initially employed AdaBoost classifier to distinguish these two groups—individuals with MAD and control subjects. AdaBoost classifier is a greatly outstanding ensemble learning method of machine learning, which even often outperforms support vector machine (SVM) [12] in some situations due to the classification results that are decided by many classifiers instead of single. We hypothesized that the abnormal areas showing in ReHo may be biomarkers for evaluating the MAD.

2. Methods

2.1. Data Acquisition and Preprocessing. Our nuclear magnetic resonance data were collected on the same fMRI instrument in the Department of Medical Imaging, Second Xiangya Hospital of Central South University. Scanning was performed using a 3.0T magnetic resonance imaging system from Siemens. A sponge earplug is inserted into the ear of the subject, and a soundproof ear is worn to reduce noise. The subjects were placed in a supine position, the head was placed in a fixed hood, and a foam pad was used to fix the sides of the head to reduce head movement. And during data acquisition, the subjects were asked to relax their minds, to keep their eyes closed, and to move as little as possible. Functional scans of the whole brain were acquired using a gradient echo EPI sequence; the parameters are as follows: TR = 2000 ms, TE = 30 ms, FOV = 220 mm, matrix = 64 × 64, flip angle = 80°, voxel size = 3.4 × 3.4 × 4 mm, slice thickness = 4 mm, and number of slice = 36. We used interlayer scanning, even layers first and then odd layers, collecting 225 time points.

Data preprocessing was carried out employing Data Processing Assistant for Resting-State fMRI (DPARSF) [13] (http://www.restfmri.net) and Spm8 (https://www.fil.ion.ucl.ac.uk/spm/) on the Matlab R2017b. For each subject, because of the magnetic saturation and instability of participants, we removed the first ten scans of the fMRI time series. For the remaining images, the preprocessing procedure included slice timing, head motion correction, and spatial normalization to standard Montreal Neurological Institute template with a resampled voxel size of 3 × 3 × 3 mm. Subjects with translation more than 1.5 mm and rotation exceeding 1.5 degrees in any direction were excluded. And then, we carried out detrending for fMRI data.

2.2. ReHo Calculation. We used DPARSF advanced edition to carry out ReHo calculation for each subject. The main idea of ReHo can be summarized as using Kendall's coefficient concordance (KCC) to measure the degree of similarity of multiple time courses [14]. The exact details of the method can be found in [15]. The KCC calculation formula at a certain point is as follows:

$$W = \frac{\sum_{i=1}^{n} (Ri)^2 - n \times \left(\bar{R}\right)^2}{(1/12)k^2 \times (n^3 - n)}, \quad (1)$$

Table 1: The information of subjects. MAD means methamphetamine dependence. The average duration of MA means the average months of individuals with MAD took methamphetamine.

Types	Individuals with MAD	Control subjects
Age (years)	21~46	20~46
Average (years)	32.5	34.2
Left/right-handed	3/42	2/41
Average duration of MA (months)	60.4	—

where W represents the value of KCC, which is between 0 and 1, k means the number of voxels in a cluster, in our study, we set k equals to 27, and n represents the time points of fMRI data. Ri means the total number of 27 voxels at the i th time point, and obviously, $\bar{R}$means the average value of R i. A pipeline of DPARSF has the function to calculate the time series consistency of each voxel and its surrounding voxels in the brain and then obtain the KCC of the voxel. In this way, we get the KCC value of each voxel in the whole brain, and we obtained the ReHo map for every subject.

2.3. Discriminative Analysis. Between-group voxel-wise comparison of the ReHo was performed using the two-sample t -test. From the result of two-sample t-test, we got different brain areas between individuals with MAD and control subjects. These brain regions were definite as regions of interest (ROIs). Each ROI was defined as a sphere (a radius of 6 mm) whose center was at the voxel showing the highest statistical difference. Then, the mean ReHo value in each ROI for each individual participant was extracted as features to classify the MAD group and the control group. AdaBoost classification is a type of ensemble learning method of machine learning, which is proposed by Freund and Schapire [16]. The AdaBoost algorithm consists of many weak classifiers. In each iteration, a new weak classifier was added to the algorithm until the classifier reaches an expected result. During the training process, we set a value for each training sample, which represents the probability that the sample is selected by the new classifier. If the sample is accurately classified in the previous classifier, its weight will decrease, otherwise increase, so that we can pay more attention to the sample of the wrong classification. The final classification result is a linear combination of multiple classifiers, which is the fundamental reason why the AdaBoost classification algorithm is often better than others. Because of the small amount of data, we used the method of leave-one-out cross-validation to train the model, and the ultimate model accuracy is the average of multiple training.

3. Results

3.1. Subjects. In our study, 41 individuals with MAD come from The Forced Isolation and Detoxification Center in Pingtang, Hunan Province, China. 42 control subjects are recruited from society; we got rid of control subjects that are diagnosed with mental diseases or subjects that have

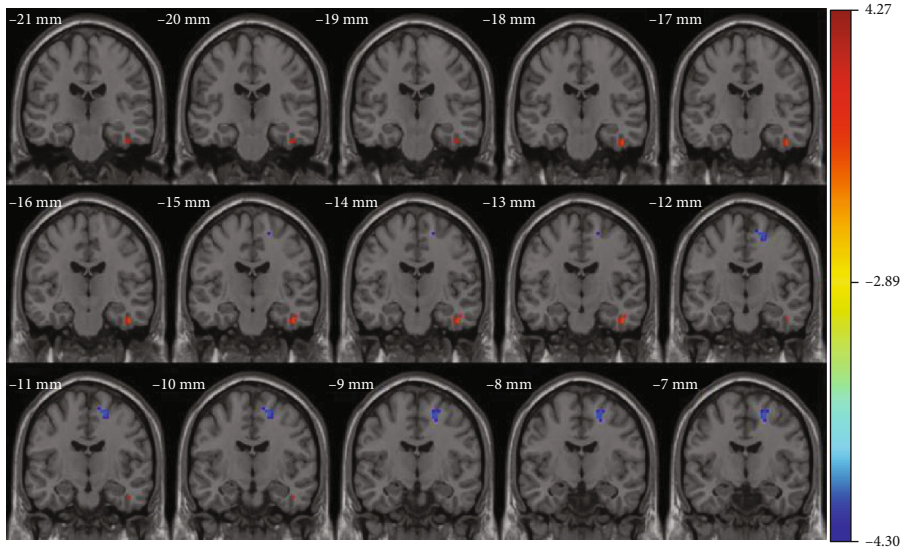

Figure 1: Significant differences in ReHo between individuals with MAD and control subjects. The parts of blue color show where ReHo value decreased in individuals with MAD compared with control subjects, and the parts of red show the increased ReHo value.

Table 2: Significant between-group differences in regional homogeneity.

Regions	L/R	Peak MNI location			Max t-value	Cluster size
		x	y	z		
Temporal IF	R	45	-15	-30	3.2546	14
Superior FG	R	18	-12	57	-3.2969	13

Abbreviations: R: right; L: left; MNI: Montreal Neurological Institute; IF: inferior fusiform; FG: frontal gyrus.

no ability to sign their names because of poor education. There are two left-handed subjects in control subjects and three left-handed subjects in individuals with MAD. For control subjects, they have no history of addictive substance dependence except nicotine. Participants who took part in the experiment were between 20 and 46 years old with an average age of 33.4. Before the data was collected, the doctor signed a written guarantee agreement with each subject, so this study was subject to approval by the ethics committee of Central South University. The relevant information about all the participants is given in Table 1.

3.2. ReHo Results. Figure 1 and Table 2 show meaningful differences between individuals with MAD and control subjects employing a two-sample t-test (after AlphaSim correction, $p = 0.05$, the minimum cluster size is 13). Compared with control subjects, individuals with MAD have lower ReHo values in the right medial superior frontal gyrus, instead, and they have higher ReHo values in the right temporal inferior fusiform.

3.3. Classification Results. We used AdaBoost classifier to discriminate individuals with MAD from control subjects by features that are significant differences in ReHo between two groups. The main idea of the AdaBoost classifier can be summarized as a linear combination of multiple weaker classifiers. We tested the number of weaker classifiers (n_estimators) from 2 to 20 and found that the best accuracy was 84.37% (Figure 2) when n_estimators equal to 4. Here, accuracy means the number of correctly classified subjects divide the total number of our subjects. From the classification result, we can reach the conclusion that AdaBoost classifier can better distinguish between normal people and individuals with MAD.

4. Discussion

Recently, methamphetamine has been becoming one of the most highly addictive drugs in the world and continues to be foremost public health problems [17]. There is an increasing number of people that are suffering from the overuse of MA, which highly affects their physical and mental health and brings misfortune to their families. Hence, it is meaningful to identify individuals with MAD and take certain procedures to alleviate their conditions.

In this paper, our purpose was to build an assistant diagnosis system for MAD based on resting-state fMRI and machine-learning methods. In our study, we exploited the approach of ReHo to research resting-state fMRI data, by computing the discernible differences between the MAD group and the control group. In addition, an effective machine-learning method—AdaBoost algorithm—was employed to distinguish individuals with MAD and control subjects with accuracy equal to 84.3%, which indicates that the AdaBoost classifier-neuroimaging approach can be a useful assistant diagnosis tool to identify individuals with MAD and help them alleviate their conditions in time. In our study, we found that individuals with MAD have lower ReHo values in their right medial superior frontal gyrus, which is consistent with the findings of Monterosso et al. and Schwartz et al. [18, 19]. On the other hand, we found that individuals with MAD have higher ReHo values in the right temporal

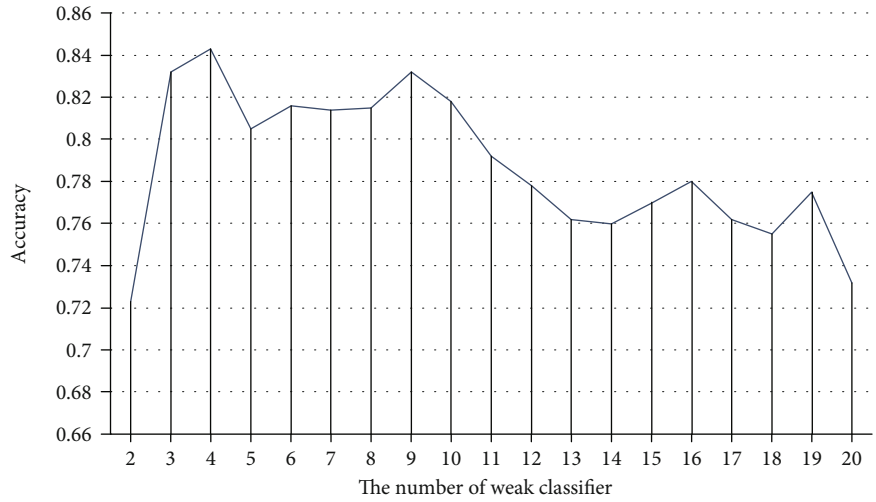

Figure 2: Relationship between the number of weak classifier and classify results.

inferior fusiform that is in accordance with Kim et al. [20]. Goldberg et al. found testimonies to prove that the superior frontal gyrus is relative to self-awareness [21, 22], and Fried et al. found that superior frontal gyrus is closely associated with laughter [23], which accord with clinical symptoms of individuals with MAD. And also, a series of researches proved that inferior fusiform gyrus is involved in higher processing of colors [24–26], which implies that it is often related to the visual pathway [27]; in other words, inferior fusiform gyrus is highly about face and body recognition and word recognition [28–30]; that is why most individuals with MAD often appear weird facial expressions and behaviors. Our research suggested that individuals with MAD have poor self-awareness such as compulsive behavior, anxiety, and poor ability to recognize face, body, and word [11]. In addition, we effectively distinguish individuals with MAD from control subjects using AdaBoost classifier that overrides support vector machine and KNN. Our results demonstrated a potential biomarker for evaluating MAD. There are many kinds of research showed that biomarkers might be employed to effectively diagnosis a variety of diseases in the medical domain [31]. Our results proved that ReHo could be a robust index for discriminating individuals with MAD from control subjects and machine learning could be a useful tool for the diagnosis of mental disease. Although we achieved 84.3% accuracy, we believe that we still have a big room to improve our model. And we only used regional homogeneity (ReHo) approach to estimate MAD; maybe we can transform our model in functional connectivity in the future. And also, deep learning outmatches traditional machine-learning algorithms in large sample data set in recent years, which may inspire us to get a more accurate result in the future.

Data Availability

All the data used in my paper are available; researchers who want to get data can email me at yuhufei@csu.edu.cn.

Conflicts of Interest

The authors declare that they have no conflicts of interest.

Authors' Contributions

Hufei Yu and Shucai Huang contributed equally to this work and should be considered co-first authors.

Acknowledgments

This work was supported by the National Natural Science Foundation of China (81971249), the National Basic Research Program of China (2015CB553504), and the National Research Program of China (2016YFC0800908-Z02).

References

[1] E. D. London, S. L. Simon, S. M. Berman et al., "Mood disturbances and regional cerebral metabolic abnormalities inrecently abstinent methamphetamine abusers," *Archives of General Psychiatry*, vol. 61, no. 1, pp. 73–84, 2004.

[2] T. F. Newton, A. D. Kalechstein, S. Duran, N. Vansluis, and W. Ling, "Methamphetamine abstinence syndrome: preliminary findings," *The American Journal on Addictions*, vol. 13, no. 3, pp. 248–255, 2004.

[3] K. M. Grant, T. D. LeVan, S. M. Wells et al., "Methamphetamine-associated psychosis," *Journal of Neuroimmune Pharmacology*, vol. 7, no. 1, pp. 113–139, 2012.

[4] A. C. Dean, S. M. Groman, A. M. Morales, and E. D. London, "An evaluation of the evidence that methamphetamine abuse causes cognitive decline in humans," *Neuropsychopharmacology*, vol. 38, no. 2, pp. 259–274, 2013.

[5] A. D. Kalechstein, T. F. Newton, and M. Green, "Methamphetamine dependence is associated with neurocognitive impairment in the initial phases of abstinence," *The Journal of Neuropsychiatry and Clinical Neurosciences*, vol. 15, no. 2, pp. 215–220, 2003.

[6] C. C. Cruickshank and K. R. Dyer, "A review of the clinical pharmacology of methamphetamine," *Addiction*, vol. 104, no. 7, pp. 1085–1099, 2009.

[7] Y. Sekine, M. Iyo, Y. Ouchi et al., "Methamphetamine-related psychiatric symptoms and reduced brain dopamine transporters studied with PET," *American Journal of Psychiatry*, vol. 158, no. 8, pp. 1206–1214, 2001.

[8] N. D. Volkow, L. Chang, G.-J. Wang et al., "Association of dopamine transporter reduction with psychomotor impairment in methamphetamine abusers," *American Journal of Psychiatry*, vol. 158, no. 3, pp. 377–382, 2001.

[9] Y. Tang, W. Liu, J. Chen, J. Liao, D. Hu, and W. Wang, "Altered spontaneous activity in antisocial personality disorder revealed by regional homogeneity," *Neuroreport*, vol. 24, no. 11, pp. 590–595, 2013.

[10] H. Liu, Z. Liu, M. Liang et al., "Decreased regional homogeneity in schizophrenia: a resting state functional magnetic resonance imaging study," *NeuroReport*, vol. 17, no. 1, pp. 19–22, 2006.

[11] Z. Ma, R. Li, J. Yu, Y. He, and J. Li, "Alterations in regional homogeneity of spontaneous brain activity in late-life subthreshold depression," *PloS one*, Y.-F. Zang, Ed., vol. 8, no. 1, 2013.

[12] C. Cortes and V. Vapnik, "Support-vector networks," *Machine Learning*, vol. 20, no. 3, pp. 273–297, 1995.

[13] Y. Chao-Gan and Z. Yu-Feng, "DPARSF: a MATLAB toolbox for "pipeline" data analysis of resting-state fMRI," *Frontiers in systems neuroscience*, vol. 4, 2010.

[14] J. L. Müller, S. Gänßbauer, M. Sommer et al., "Gray matter changes in right superior temporal gyrus in criminal psychopaths. Evidence from voxel-based morphometry," *Psychiatry Research: Neuroimaging*, vol. 163, no. 3, pp. 213–222, 2008.

[15] L. Ni, R. Qi, L. J. Zhang et al., "Altered regional homogeneity in the development of minimal hepatic encephalopathy: a resting-state functional MRI study," *PloS one*, vol. 7, no. 7, p. e42016, 2012.

[16] Y. Freund and R. E. Schapire, "A desicion-theoretic generalization of on-line learning and an application to boosting," in *European Conference on Computational Learning Theory*, pp. 23–37, Barcelona, Spain, 1995.

[17] E. D. London, M. Kohno, A. M. Morales, and M. E. Ballard, "Chronic methamphetamine abuse and corticostriatal deficits revealed by neuroimaging," *Brain Research*, vol. 1628, pp. 174–185, 2015.

[18] J. R. Monterosso, G. Ainslie, J. Xu, X. Cordova, C. P. Domier, and E. D. London, "Frontoparietal cortical activity of methamphetamine-dependent and comparison subjects performing a delay discounting task," *Human Brain Mapping*, vol. 28, no. 5, pp. 383–393, 2007.

[19] D. L. Schwartz, A. D. Mitchell, D. L. Lahna, et al., "Global and local morphometric differences in recently abstinent methamphetamine-dependent individuals," *NeuroImage*, vol. 50, no. 4, pp. 1392–1401, 2010.

[20] Y. T. Kim, H. J. Song, J. H. Seo et al., "The differences in neural network activity between methamphetamine abusers and healthy subjects performing an emotion-matching task: functional MRI study," *NMR in Biomedicine*, vol. 24, no. 10, pp. 1392–1400, 2011.

[21] I. I. Goldberg, M. Harel, and R. Malach, "When the brain loses its self: prefrontal inactivation during sensorimotor processing," *Neuron*, vol. 50, no. 2, pp. 329–339, 2006.

[22] S. M. Platek, J. P. Keenan, G. G. Gallup Jr., and F. B. Mohamed, "Where am I? The neurological correlates of self and other," *Cognitive Brain Research*, vol. 19, no. 2, pp. 114–122, 2004.

[23] I. Fried, C. L. Wilson, K. A. MacDonald, and E. J. Behnke, "Electric current stimulates laughter," *Nature*, vol. 391, no. 6668, pp. 650–650, 1998.

[24] V. S. Ramachandran, *The Tell-Tale Brain: Unlocking the Mystery of Human Nature: Random House*, 2012.

[25] M. Corbetta, F. Miezin, S. Dobmeyer, G. Shulman, and S. Petersen, "Attentional modulation of neural processing of shape, color, and velocity in humans," *Science*, vol. 248, no. 4962, pp. 1556–1559, 1990.

[26] W. K. Simmons, V. Ramjee, M. S. Beauchamp, K. McRae, A. Martin, and L. W. Barsalou, "A common neural substrate for perceiving and knowing about color," *Neuropsychologia*, vol. 45, no. 12, pp. 2802–2810, 2007.

[27] E. M. Hubbard and V. S. Ramachandran, "Neurocognitive mechanisms of synesthesia," *Neuron*, vol. 48, no. 3, pp. 509–520, 2005.

[28] N. George, R. J. Dolan, G. R. Fink, G. C. Baylis, C. Russell, and J. Driver, "Contrast polarity and face recognition in the human fusiform gyrus," *Nature Neuroscience*, vol. 2, no. 6, pp. 574–580, 1999.

[29] S. Bölte, D. Hubl, S. Feineis-Matthews, D. Prvulovic, T. Dierks, and F. Poustka, "Facial affect recognition training in autism: can we animate the fusiform gyrus?," *Behavioral Neuroscience*, vol. 120, no. 1, pp. 211–216, 2006.

[30] B. D. McCandliss, L. Cohen, and S. Dehaene, "The visual word form area: expertise for reading in the fusiform gyrus," *Trends in Cognitive Sciences*, vol. 7, no. 7, pp. 293–299, 2003.

[31] X. Chen, Y. Ba, L. Ma et al., "Characterization of microRNAs in serum: a novel class of biomarkers for diagnosis of cancer and other diseases," *Cell Research*, vol. 18, no. 10, pp. 997–1006, 2008.

Hindawi
Computational and Mathematical Methods in Medicine
Volume 2020, Article ID 5487168, 16 pages
https://doi.org/10.1155/2020/5487168

Research Article

Logarithmic Fuzzy Entropy Function for Similarity Measurement in Multimodal Medical Images Registration

Yu Miao[1], **Jiaying Gao**[1], **Ke Zhang**[1], **Weili Shi**[1], **Yanfang Li**[1], **Jiashi Zhao**[1], **Zhengang Jiang**[1], **Huamin Yang**[1], **Fei He**[1], **Wei He**[1], **Jun Qin**[1] and **Tao Chen**[2]

[1]*Changchun University of Science and Technology, School of Computer Science and Technology, WeiXing Road, Changchun 130022, China*
[2]*Department of General Surgery, Nanfang Hospital, Southern Medical University, Guangzhou 510515, Guangdong Province, China*

Correspondence should be addressed to Zhengang Jiang; jiangzhengang@cust.edu.cn and Huamin Yang; yhm@cust.edu.cn

Received 21 August 2019; Revised 16 November 2019; Accepted 14 December 2019; Published 12 February 2020

Guest Editor: Sebastian Adamczyk

Multimodal medical images are useful for observing tissue structure clearly in clinical practice. To integrate multimodal information, multimodal registration is significant. The entropy-based registration applies a structure descriptor set to replace the original multimodal image and compute similarity to express the correlation of images. The accuracy and converging rate of the registration depend on this set. We propose a new method, logarithmic fuzzy entropy function, to compute the descriptor set. It is obvious that the proposed method can increase the upper bound value from $\log(r)$ to $\log(r) + \Delta(r)$ so that a more representative structural descriptor set is formed. The experiment results show that our method has faster converging rate and wider quantified range in multimodal medical images registration.

1. Introduction

Multimodal medical images are important for observing tissue structures clearly in clinical practice, such as MRI/T1, MRI/T2, and MRI/PD images. To integrate multimodal information, multimodal registration is important in practical application [1, 2].

It is hard to find relevant information on multimodal medical images because of different weighting properties. To solve this problem, many research works try to find the potential relationship based on intensity value. Whereupon, mutual information (MI) [3] has been extensively applied for multimodal medical image registration. In 2004, Russakoff et al. used MI on medical images registration [4], while it is sensitive on implementation decisions as well as small convergence rate. In 2010, Loeckx et al. used conditional mutual information as a new similarity measure in nonrigid image registration [5]. However, it has an obvious drawback in time consumption. There is an alternative method to decrease the algorithmic complexity, which simulates one modality with the other. This needs a descriptor set to inherit the structure or richness of original modality with the other modality's character expressed. For example, in 2008, Wein et al. [6] registered ultrasound and CT with the simulation of ultrasound images. And In 2013, Xu et al. [7] registered CT image to ultrasound image with simulating the ultrasound image, which has many objective restrictions and the accuracy depends on manual landmark. We are interested in a general structural representation, so these specific approaches are not applicable. The universal adaptability and computational complexity seem incompatible. However, in 2012, Wachinger and Navab [8] proposed the descriptor set based on middle-type artificial modality. It has both general adaptability and low complexity, which is the method we will improve in this article. In the same year, Heinrich et al. computed third-type modality by MIND descriptor set [9]. The descriptor is suitable for different modality-group registration. However, it is affected by rotational variant and cannot recover strong rotations. The descriptor needs ability to express the

anatomical feature presented in both modalities. In 2015, Oktay et al. [10] presented a structural representation, which is trained by structured decision forest, namely, Probabilistic Edge Map (PEM). This method lacks a certain generalization ability, which requires manual intervention to adjust parameters and repeated training steps alone. In 2016, Simonovsky et al. [11] applied a deep convolutional neural network (CNN) algorithm to multimodal image registration and optimized it with a continuous framework. The trained network can output the convolutional descriptor set which can address the binary classification between aligned and misaligned, although it causes a huge computing cost in iteration. In 2017, Cao et al. [12] overcame the problem of CT-MRI pelvic image registration by establishing a bidirectional image synthesis. The shortcoming of synthesis methods is the feasibility in other image modalities, which limits their clinical applications. In 2018, Luo et al. computed the descriptor vector based on a novel variogram-based outlier screening method [13]. However, it focuses on space location relationship and loses sight of potential richness. Most recently, in 2019, Bashiri et al. [14] expressed the descriptor set in high dimensional space, studying potential structures of an image through Laplacian eigenmap. Nonlinear dimensionality reduction from manifold space will result in the loss of original potential information. Since the registration of medical images from different modalities is more affected by substantial intensity variations, we prefer the method that is based on pixel intensity distribution.

1.1. Motivations and Main Contributions. In clinical application, different modalities have different display emphases. In this case, a universally adaptable approach has significance in multimodal registration. An alternative method is transferring both different modalities into third-type artificial modalities with carrying original potential information. Wachinger and Navab computed third-type modality by entropy [8]. A structure descriptor set was applied to replace the original multimodal image. It has universality and lower computation complexity. However, we found that the above method (entropy function) is only used for quantifying the uncertainty of patches with limited range.

We propose a logarithmic fuzzy entropy function with wider quantified range, which increases the upper bound value from $\log(r)$ to $\log(r) + \Delta(r)$. The experimental results show that our method has faster converging rate and wider quantified range in multimodal medical image registration.

2. Structure Descriptor Set

Descriptor set is a medium to express substantial information of original image such as edge, corner, texture, and gradient. In this article, each descriptor is computed by the intensity distribution, which is generated by a local patch. Furthermore, we find that the descriptor contains the structure and richness information, where richness information exists in the form of quantifying its uncertainty, and then the structure descriptor set consists of these descriptors. Such structure descriptor sets can assist many image processing tasks. An accurate structure descriptor set can express the structure and intensity distribution information, reduce the redundant data, and improve the rate of convergence to the extremum value of algorithm. In addition to the above three advantages, we also transform the multimodal image into a third-type modality simultaneously. Finally, under the same modality, we obtain the similarity value by computing the L1 norm of two corresponding structure descriptor sets.

2.1. Entropy Image. Wachinger and Navab proposed a structural representation based on the entropy image [8]. The image is divided into many patches, and each patch has its structural descriptor. Structural descriptors are applied to form a completely new image, which are called structural representation. In the new image, every pixel can be calculated as follows:

$$D^I_{x,l} = H\left(I \mid N_{x,l}\right), \tag{1}$$

where H is the entropy calculation, I is image, $N_{x,l}$ is the square neighborhood, which takes x position as centre l as side length, and $D^I_{x,l}$ is structure descriptor value of $N_{x,l}$. This method quantifies the uncertainty value of the patch with entropy. But the quantification range is only from 0 to $\log(r)$, which needs to be optimized.

2.2. MIND Descriptor Set. Heinrich et al. proposed the MIND method (morphological independent neighborhood descriptor for multimodal registration) [9]. The characteristics of local self-similarity are used to describe structural information. In this descriptor set, each pixel value is calculated as follows:

$$\mathrm{MIND}(I, x, r) = \frac{1}{n}\exp\left(\frac{-D_p(I, x, x+r)}{V(I, x)}\right), \quad r \in R, \tag{2}$$

where r is the neighborhood block, D is the correlation between the neighborhoods, and n is the normalization constant. Each position x of image will be replaced by a vector of size $|R|$ when the MIND operation is performed.

3. The Method of Measurement Function

The method proposed in this article is based on intensity distribution. The essence is to find a function to compute the descriptors. Each descriptor contains the local information of original image, such as intensity richness of local neighborhood. Richness information exists in the form of quantifying the uncertainty value of local neighborhood. Some measurement functions can quantify the uncertainty of set. Buzug et al. adopted strict convex function instead of Shannon entropy [15]. Subsequently, Pluim et al. proposed F information measure instead of the entropy value in mutual information MI calculation [16]. Experiments showed that the registration results of these F information measurements (strict concave function) can imitate mutual information, and some of them have higher precision. These researches prove that there are some measurement functions that have good performance to quantify the uncertainty set, such as entropy function in chapter 3.1 and strict concave function in chapter 3.2.

3.1. The Entropy (M1). The Shannon entropy of a random variable "A" with a possible value "a" is defined as follows:

$$H(A) = -\sum_{i \in a} P(A = i) \times \log P(A = i). \tag{3}$$

When we calculate the variation of intensity, which occurs in the same position, image gradient is always used for image processing [17]. But, it depends on similarity value and is not suitable for describing the structure detail. A more general concept is to quantify the uncertainty content or, analogously, the bound for a lossless compression, as stated by Shannon's theorem. The entropy function originates from the field of thermodynamics at the earliest. It can measure the uncertainty of variable information. When there are intersections between two images, the correlation of the two images can be calculated with $I(A, B) = H(A) + H(B) - H(A, B)$. The above theory is derived from the mutual information MI algorithm [4].

Shannon pointed out that the measurement function of uncertainty should satisfy the following three prior conditions:

(1) Continuity condition: $f(p_1, p_2, \ldots, p_k)$ should be a continuity function of $(p_1, p_2, \ldots, p_k)$.

(2) Monotonicity: under the equal probability $f(1/r, 1/r, \ldots, 1/r) = g(r)$. $g(r)$ should be the increasing function of r.

(3) Additivity condition: when the value of a random variable is obtained from multiple trials rather than one trial, the uncertainty of the random variable in each experiment should be additive.

Condition 1 and 2 mean that the function must have the ability to quantify the uncertainty of the information. Condition 3 is used for multiple information sources. For example, we measure the occurrence probability of each event in set X as follows: $(p_1, p_2, \ldots, p_n)$. The probability of each event in set Y is as follows: $(q_1, q_2, \ldots, q_m)$. We statistic the entropy of the joint information source X, and Y is equal to the sum of the entropy of the information sources X and Y. $H(XY) = H(X) + H(Y)$.

$$\begin{aligned} &H_{nm}(p_1q_1, p_1q_2, \ldots, p_1q_m, p_2q_1, \ldots, p_nq_m) \\ &\quad = H_n(p_1, p_2, \ldots, p_n) + H_m(q_1, q_2, \ldots, q_m), \\ &\sum_{i=1}^{n} p_i = 1, \\ &\sum_{j=1}^{m} q_j = 1, \\ &\sum_{i=1}^{n} \sum_{j=1}^{m} p_i q_j = 1. \end{aligned} \tag{4}$$

The purpose of this article is simply to find a function that can count the uncertainty of a patch (i.e., satisfy conditions 1 and 2). So, it is not necessary to count the joint uncertainty between any patches.

Entropy is not the only function that can describe the uncertainty of information. Wierman studied the uncertainty measure of information entropy under a rough set [18]. Düntsch and Gediga studied the problem based on knowledge granularity measurement [19]. Yumin et al. proposed several uncertainty measures of neighborhood granule, which had good performance in neighborhood systems [20]. Huang and Wen found that the strict concave function can also calculate the uncertainty of the information and discussed the relationship between the entropy and strict concave function [21]. Wei et al. discussed the uncertainty metric based on fuzzy entropy systematically [22]. In this article, we have introduced three other strict concave functions for the coming experiment (see 3.2 for details).

3.2. Strict Concave Function. If function $f(x)$ is defined in the interval I, there are two points $x1$ and $x2$ in I. For any $\lambda \in (0, 1)$ it has

$$f(\lambda x_1 + (1 - \lambda) x_2) > \lambda f(x_1) + (1 - \lambda) f(x_2). \tag{5}$$

According to the definition and properties of strict concave functions, we propose three functions:

(1) $f_1(x) = -[x \log x + (1 - x) \log(1 - x)]$, $x \in (0, 1]$, assign $0 \times \log 0 \coloneqq 0$

(2) $f_2(x) = x * \exp(1 - x) + (1 - x) * \exp(x) - 1$, $x \in (0, 1]$

(3) $f_3(x) = x/(1 + x) - x/2$, $x \in (0, 1]$

$f1(x)$ and $f2(x)$ are fuzzy entropy in the strictly concave function. $f3(x)$ is just a strictly concave function rather than a fuzzy entropy function. $f1$ function was presented by De et al. and called logarithmic fuzzy entropy function [23]. $f2$ function was presented by Pal NR et al. and called exponential fuzzy entropy function [24]. The images of four functions are shown in Figure 1.

3.3. From Entropy Function to Strict Concave Function

Theorem 1 (see [25]). *The intensity value x_i $i \in \{1, 2, 3, \ldots, r\}$. According to the definition of entropy function, its range is $0 \le H(A) \le \log(r)$. For certain $i = [1, r]$, if $P(x_i) = 1$, the minimum $H(A) = 0$. For all $i = [1, r]$, if $P(x_i) = 1/r$, then maximum $H(A) = \log(r)$.*

Theorem 1 illustrates that the entropy function can distinguish the dispersion of the probability distribution. For example, a monochrome image contains the least amount of information. And its intensity probability is only distributed at one point, which proves that the set (i.e., image) contains the smallest uncertainty of information. So, the minimum of entropy is 0. We make the hypothesis that there are 256 gray levels ($r = 256$) in the image. Besides, the number of pixels in any gray level is equal, and the gray probability distribution of image satisfies the uniform distribution. At this time, the set (i.e., the image) contains the largest information uncertainty, and the maximum of entropy is $\log(256)$.

Theorem 2 (see [15]). *If $f(x)$ is a differentiable strict concave function, then $f(x)$ has the generalized subadditivity. When $\forall x_1, x_2, \theta \in R^+$ and $0 < \theta \le x_1 \le x_2$, the following inequality is established:*

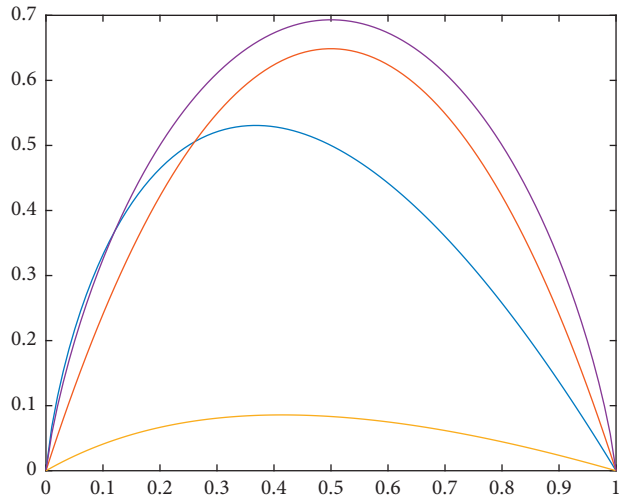

FIGURE 1: Yellow curve: $y = x/(1+x) - x/2$; blue curve: $y = -x\log(x)$; purple curve: $y = -[x\log(x) + (1-x)\log(1-x)]$; orange curve: $y = x * \exp(1-x) + (1-x)\exp(x) - 1$.

$$f(x_1 - \theta) + f(x_2 + \theta) < f(x_1) + f(x_2), \tag{6}$$

the variable x in the function f(x) represents the probability in medical image registration, so $x \in [0,1], \sum x_i = 1, i \in \{1,2\}$; $0 \le x_1 - \theta < x_1 \cap x_2 < x_2 + \theta \le 1$; *formula (6) shows that* $f(x_1) + f(x_2)$ *has the maximum value at* $x_1 = x_2 = 1/2$ *and minimum value at* $x_1 = 0$, $x_2 = 1$. *So,* $f(x_1) + f(x_2)$ *can express the measure of the probability distribution. Theorem 3 is obtained when the two sums of the above strictly concave functions are generalized to the sum of the r terms.*

Theorem 3. *If the function f(x) has the strict generalized subadditivity,* $x_i\,(i = 1, 2 \ldots, n)$ *indicates the probability of gray value (i) in the image, and* $\sum_{i=1}^{n} x_i = 1$. *Then uncertainty measurement* $M = \sum_{i=1}^{n} f(x_i)$ *can get the maximum value at* $x_i = 1/n$, $(x_1 = x_2 = x_i = \cdots = x_n)$ *and minimum value at* $x_i = 1, i \in \{1, 2, 3 \ldots, n\}$.

Theorem 2 and Theorem 3 illustrate that the strict concave function can discriminate the probability distribution. When the histogram of the probability distribution is closer to a uniform distribution, the measured value of the strict concave function is the largest; if the distribution is concentrated on an individual point, the measure of the strict concave function is the smallest.

3.4. Advantage of Logarithmic Fuzzy Entropy Function. This new function improves the performance by extending the quantification range of patch. Through mathematical derivation, Wachinger and Navab used entropy to quantify a single patch, the upper bound is $\log(r)$ [8]. However, logarithmic fuzzy entropy function has better symmetry, and it can increase the upper bound from $\log(r)$ to $\log(r) + \Delta(r)$, where $r = \min(l^2, 2^n)$ is the variety degree in patch; l is the side length of patch; n is the bit depth of image; $\Delta(r)$ is monotone increasing function of r. In most situation, the magnitude of l^2 and 2^n is depending on the requirement of performance. No matter in which situation, logarithmic fuzzy entropy function has good performance in quantifying the uncertainty of the patch. Experiments 5.2 and 5.3 show that logarithmic fuzzy entropy function brings faster convergence rate than entropy in multimodal registration, and the convergence rate will increase as r increases.

Logarithmic fuzzy entropy function can bring a more representative structure descriptor set. First of all, we need assume that when probability $p = 1$ in logarithmic fuzzy entropy function, namely, $M_2(1) = 0 \times \log 0$. This situation means the patch we calculated is a monochrome patch, so we assign $0 \times \log 0 := 0$. The medical image is stored by two bytes per pixel and the bit depth is n $(n \le 16)$, so the variety degree of the patch $r = \min(l^2, 2^n)$. When probabilities of intensity $p_1 = p_2 = \cdots = p_r = 1/r$, the uncertainty value of patch can reach the upper bound. We make a comparison among the entropy function (M1), logarithmic fuzzy entropy function (M2), exponential fuzzy entropy function (M3), and strict concave function (M4) in Table 1.

We compare the rate of two functions tending to infinity:

$$\lim_{r \longrightarrow +\infty} \frac{\log(r)}{\log(r) + (r-1)\log(r/r-1)} = 0, \quad (r = 2^n, n = 0, 1, 2, \ldots), \tag{7}$$

$$\lim_{r \longrightarrow +\infty} \Delta(r) = \lim_{r \longrightarrow +\infty} B_2(r) - B_1(r) = \lim_{r \longrightarrow +\infty} (r-1)\log\left(\frac{r}{r-1}\right) = 1, \quad (r = 2^n, n = 0, 1, 2, \ldots). \tag{8}$$

The curve diagram is showed in Figure 2. There are no much differences between the two function curves when r is less than 256. But in medical image, r is more than 256. The $\Delta(r)$ becomes more bigger as variety degree r (i.e., $r = 2^n$) increases; however, that difference value $\Delta(r)$ will converge at 1 as shown in formula (8). The larger upper bound brings the wider quantification range, for example, in 256 gray-scale images, the M2 can increase 18% quantification range than M1. Thus, we can compute more representative structure descriptor set under logarithmic fuzzy entropy function (M2).

Theoretically, logarithmic fuzzy entropy function M_2 can compute more representative structure descriptor set because of the larger quantification upper bound. But, the upper bound function B_3 and B_4 converge at 2.705 and 0.496 early. That means before the convergence, M_3 and M_4 can quantify the uncertainty of the image, but when r approaches the value of convergence, the upper bound cannot increase as r increases.

4. Experiment Process

Figure 3 shows the process of the experiment, where we use L1 norm to calculate S. The similarity equation can be abstracted as follows:

$$S = \mathrm{MAD}(A, T(B)). \tag{9}$$

Table 1: Upper bound table for 4 strict concave functions.

Function	Upper bound	$B_{(r\longrightarrow\infty)}$
$M_1(p_i) = \sum_r p_i \log p_i$	$B_1(r) = \log(r)$	$+\infty$
$M_2(p_i) = \sum_r -[p_i \log p_i + (1-p_i)\log(1-p_i)]$	$B_2(r) = \log(r) + (r-1)\log r/r - 1$	$+\infty$
$M_3(p_i) = \sum_r [p_i \exp(1-p_i) + (1-p_i)\exp(p_i) - 1]$	$B_3(r) = \exp(r-1/r) + (r-1)\exp(1/r) - r$	2.705
$M_4(p_i) = \sum_r [p_i/1 + p_i - p_i/2]$	$B_4(r) = r/r + 1 - 1/2$	0.496

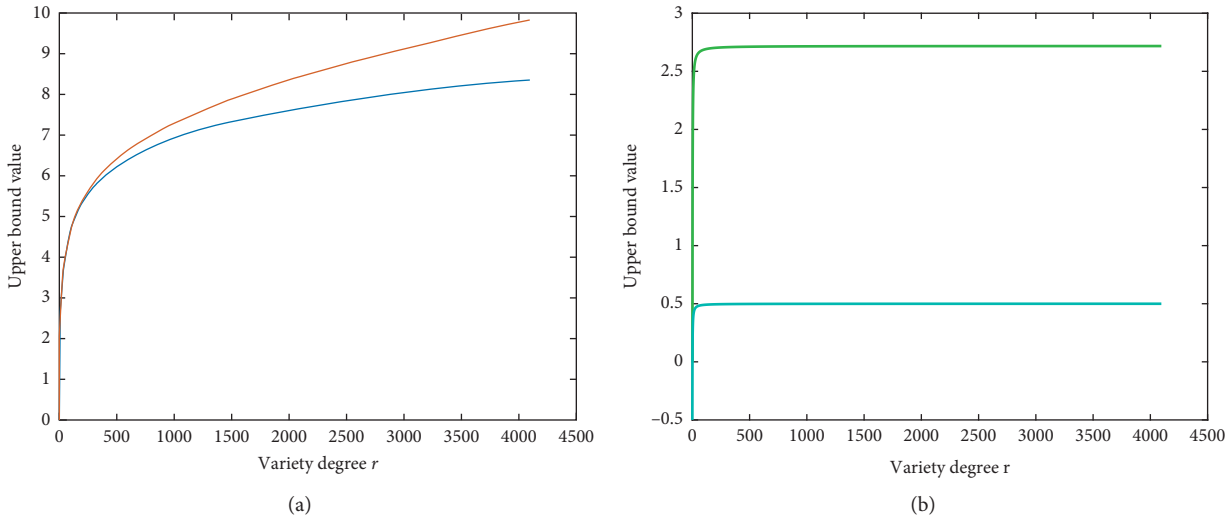

(a) (b)

Figure 2: Upper bound function curve. Blue: $B_1(r)$; orange: $B_2(r)$; green: $B_3(r)$; cyan: $B_4(r)$, r is variety degree.

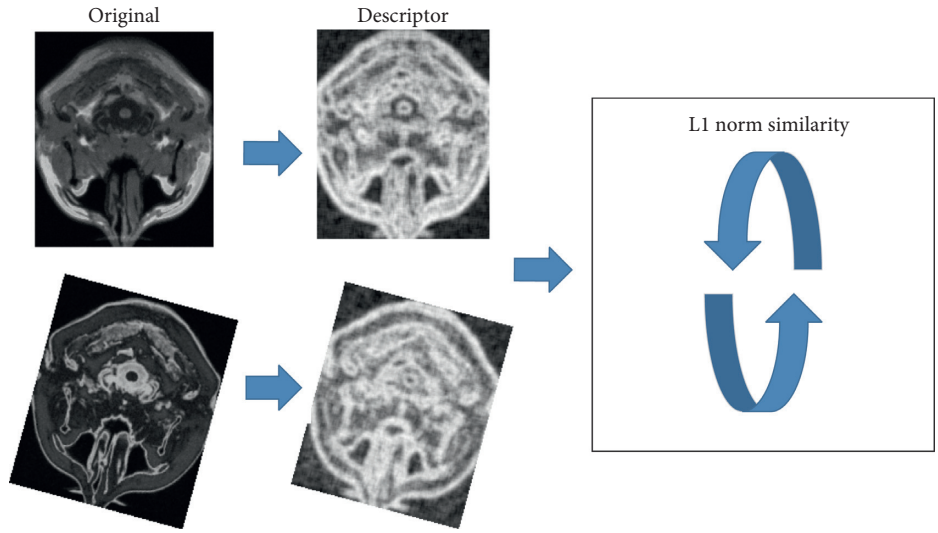

Figure 3: This figure shows the process from the original image to registration. We use L1 norm as similarity measure.

The most similarity status of images A and B is found by using the spatial transformation T and the "MAD" similarity is measured by using the L1 norm. Our target is to find the structure descriptor set D^A, D^B to replace A and B. The similarity equation is converted to

$$S = \mathrm{MAD}\left(D^A, D^{T(B)}\right). \tag{10}$$

4.1. Calculate Descriptor Set. A patch $N_{x,l}$ is formed by taking pixel x as a centre and l as the side length. Taking Figure 4 as an example, patch Y has 81 pixels and the side length l equals 9. We statistic the intensity histogram and substitute the probability of intensity value into four strict concave functions.

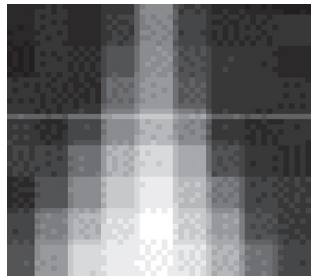

Figure 4: 9×9 patch Y.

$$M_1(x) = \sum_i -x\log(x), \quad x \in (0,1],$$

$$M_2(x) = \sum_i -[x\log(x) + (1-x)\log(1-x)], \quad x \in (0,1],$$

$$M_3(x) = \sum_i \left[xe^{1-x} + (1-x)e^x - 1\right], \quad x \in (0,1],$$

$$M_4(x) = \sum_i \left[\frac{x}{1+x} - \frac{x}{2}\right], \quad x \in (0,1]. \tag{11}$$

M_1 is entropy function, M_2 is based on logarithmic fuzzy entropy function, M_3 is based on exponential fuzzy entropy function, and M_4 is based on normal strictly concave function. We replace (1) with the above four functions and get (12).

$$D_{x,l}^A = M_k\left(A \mid N_{x,l}\right), \quad k = 1,2,3,4. \tag{12}$$

It is available to calculate the uncertainty value of patch Y by formula (12). The process from original to descriptor set is shown in Figure 5.

According to the thought of Wachinger and Navab [8], an image is decomposed into several patches, and the respective descriptor values of each patch are calculated by entropy function. In this article, we want to improve the quantification range of descriptor values by the logarithmic fuzzy entropy function and verify the relationship between the quantification range and the speed of convergence. Logarithmic fuzzy entropy function and other strict concave functions have already been discussed in chapters 3.2–3.4.

4.2. The Weighting and Patch. If two patches have the same intensity value histogram but the structure is different, it will result in the same descriptor value such as in Figure 6. To distinguish that situation, we quote Gaussian weights and modified weighting (Figure 7) from the original author's article [8]. There is a spatial weighting function $\omega: N_{x,l} \longrightarrow \mathbb{R}$. Assigning a weight to each patch location, the histogram update changes to

$$\forall y \in N_{x,l}: h_x[I(y)] \longleftarrow h_x[I(y)] + \omega(y). \tag{13}$$

Gaussian weighting formula is $\omega(y) = G_\sigma(y-c)$. The modified Gaussian weighting does not have symmetry compared with the former. In the experiment, these two weights improve the performance of computing descriptor values. It can reflect the local specificity of each point and, at the same time, keep the structure information in the original image. The result is shown in Figure 8.

5. Results and Discussion

5.1. Experimental Result of Structure Descriptor Set. We use all the descriptor values $D_{x,l}^I$ to replace the x position. Structural descriptor sets are shown in Figure 9:

In Figure 9, three different modalities are turned into a third-type artificial modality, and under this modality, we find that they retain the structural information of the original image. The structure descriptor set is computed by four kinds of measurement function. The first row is the result under MRI/T1 modality; second row is the result under MRI/T2 modality; and third row is the result under MRI/PD modality. Each column is the set of structure descriptors calculated under the corresponding measure function. These structure descriptor sets are computed by patch $N_{x,l}$, where l is 7.

In Figure 10, we alter the side length l of the patch, where l equals 3, 7, 11, 15, and 19, to calculate the variation of the structure descriptor set. It is found that the image becomes blurred as the l increases, which has a similar effect to Gaussian blur. Structurally, the smaller the l is, the more sufficient the detail will be. However, statistically, the smaller the l is, the duplicate values $D_{x,l}^A$ will get more because the probability distribution of repetition will get more. The bigger the l is, the more accurate the value will be because the phenomenon of repeating the probability distribution will be greatly reduced. We inspect pixel value in Figure 10 T1-M1($l = 3$), there are many duplicate values in it. On the other hand, considering the influence of the local noise, a large patch has a strong ability to suppress that influence.

5.2. Anti-Rotation Experiment of Changing the Size of Patch ($l^2 < 2^n, r = l^2$). In Figure 11, we verify the relationship between the patch size and convergence rate. We selected the size of patch from $3 * 3$ to $19 * 19$, and the upper bound will change as patch size changes. In this experiment, we use entropy function (M1) and logarithmic fuzzy entropy function (M2) simultaneously. The dashed and solid curves show that the rate of converging to extremum increases as patch size increases. For each color pair (i.e., in the same patch size), the solid curve is faster than the dashed curve. In this experiment, we keep one image fixed, and the other one rotates along the centre from -25 to 25 degrees. At each angle, the similarity of the two images is measured by M1 and M2. We obtain these data sets from DICOM Library (https://www.dicomlibrary.com). In this data set, there are two different MRI modalities. The image size is $512 * 512$ and stored by 13 effective bit depths. There are 47 layers in each modality, so each curve is an average result of 47 layers in two different modalities.

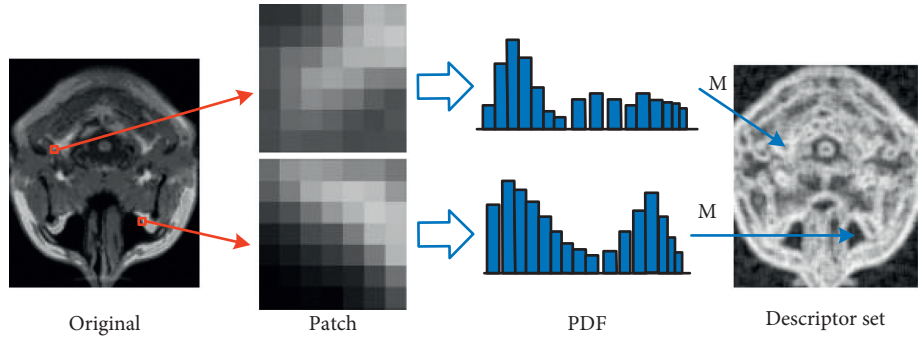

Figure 5: Illustration of the process of computing structure descriptor set. The original image is divided into many patches, and the centre and neighborhood are selected in each patch. The PDF is generated by the statistical histogram of the patch. All the grayscale probabilities of single patch are substituted into the measure function M to obtain uncertainty values, namely, descriptor value. Finally, the descriptor value is stored in the corresponding location to create descriptor set [8].

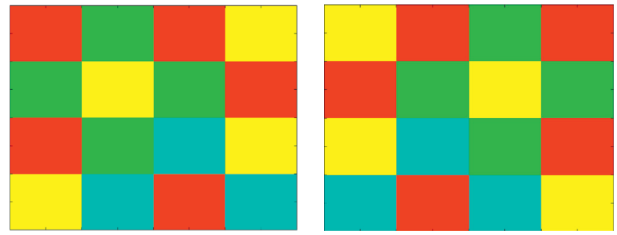

Figure 6: Two patches with symmetrical structure will generate duplicate values because they have the same histogram.

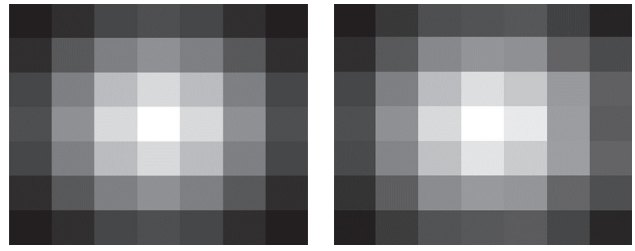

Figure 7: (a) Gaussian weight map; (b) modified weight map.

When $l^2 < 2^n$, according to Table 1, the upper bound of M1 and M2 are $B_1(l^2) < B_2(l^2)$, where each upper bound has a monotonically increasing relationship with patch size. This experiment proves that the M2 function has faster convergence rate than M1 in the small patch. It can satisfy the requirement of decreasing code running time with the small patch.

5.3. Anti-Rotation Experiment of Compressing the Effective Bit Depth ($\mathbf{l^2 > 2^n}$, $\mathbf{r = 2^n}$). In Figure 12, we verify the performance of M2 function when the intensity bit depth n decrease from 13 to 7. This time, we select the patch size as $65 * 65$, because it can contain richer variety. In such a large patch size, the upper bound will change as the bit depth changes. According to Figure 2, the difference of the upper bound of two functions will increase as the variety degree increases. That means, the M2 function's result is better than the M1 function's result in a lager bit depth. There are two different MRI modalities. Each modality has 47 layer images, and each layer is stored in $512 * 512$, two bytes, 13 effective bits (i.e., bit depth n is 13). So, we make an experiment about decreasing the bit depth n from 13 down to 7. They are equal when compressing the intensities down to 1/64, 1/32, 1/16, 1/8, 1/4, and 1/2 of the original image.

We consider one pair color as one group experiment, which contains one dashed curve (M1 function) and one solid curve(M2 function). The different color means different bit depths. For example, the red pair is the original

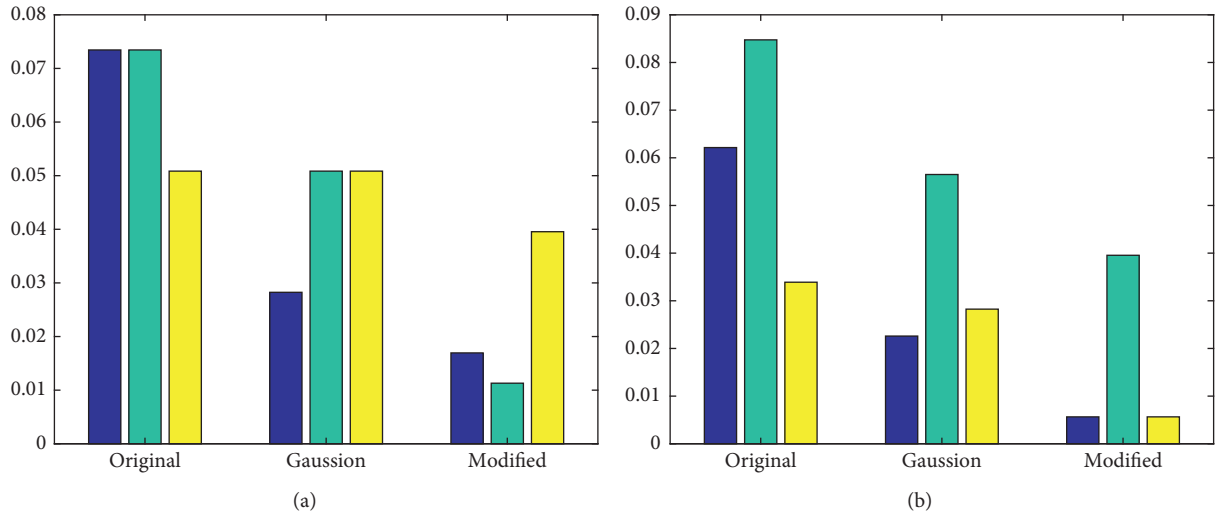

Figure 8: Accuracy error histogram obtained using three weighting methods, blue: T1-T2 data set; green: T1-PD data set; yellow: T2-PD data set, y label is accuracy. (a) M1. (b) M2.

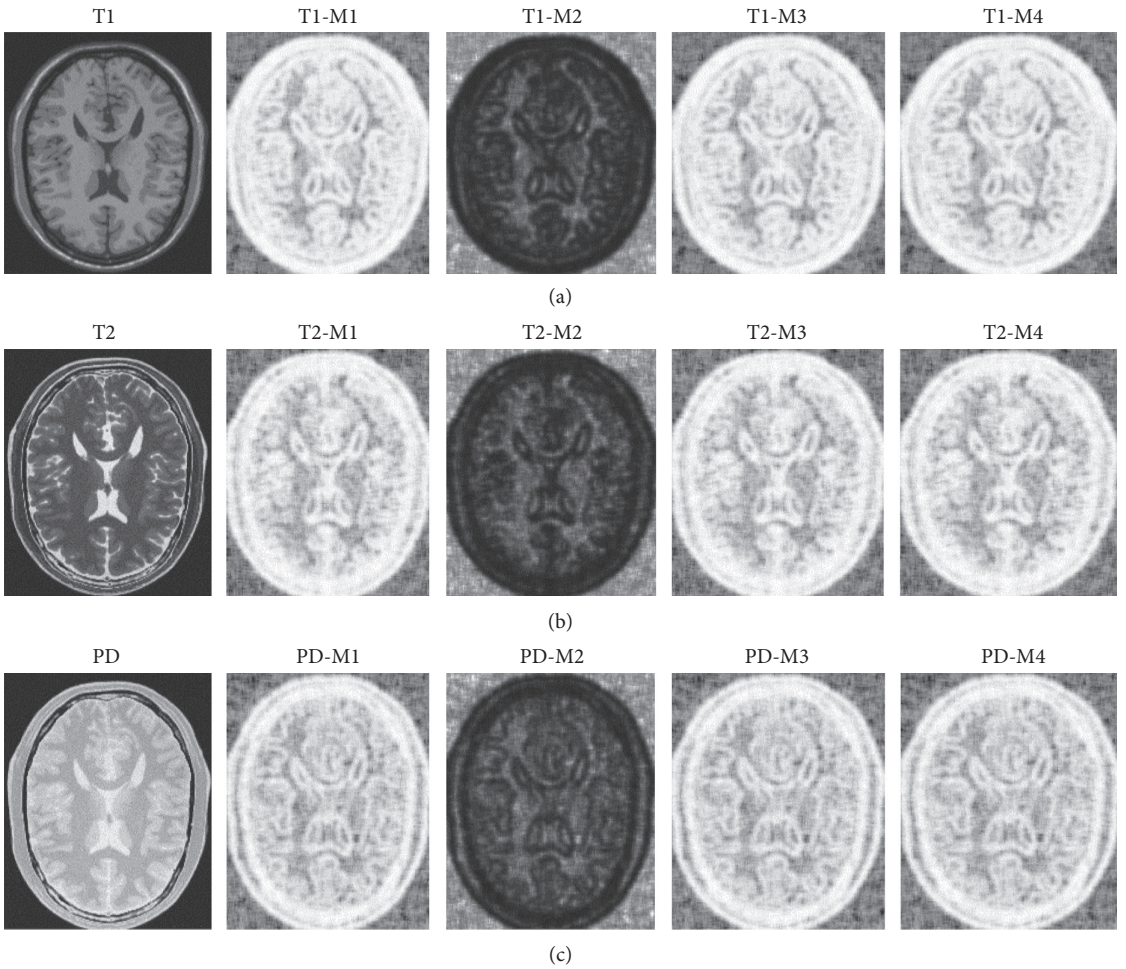

Figure 9: Descriptor set calculated by M1, M2, M3, and M4 under multimodal (T1, T2, and PD).

image, the blue pair is using 12 effective bits; the green pair is using 11 effective bits; the cyan pair is using 10 effective bits; the magenta pair is using 9 effective bits; the yellow pair is using 8 effective bits, and the black pair is using 7 effective bits to express the image. Each curve is the average result of 47 couple, and each couple images contain two different

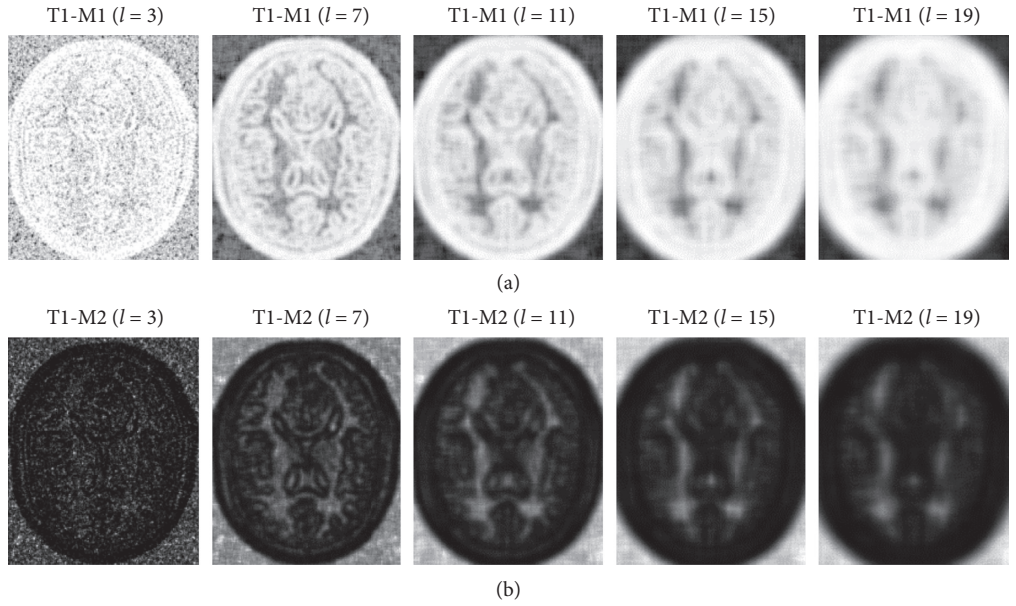

Figure 10: The first row computes T1 modality with M1 function, and the second row computes T1 modality with M2 function. Each column has different patch side length, from left to right $l = 3$, 7, 11, 15, and 19, respectively.

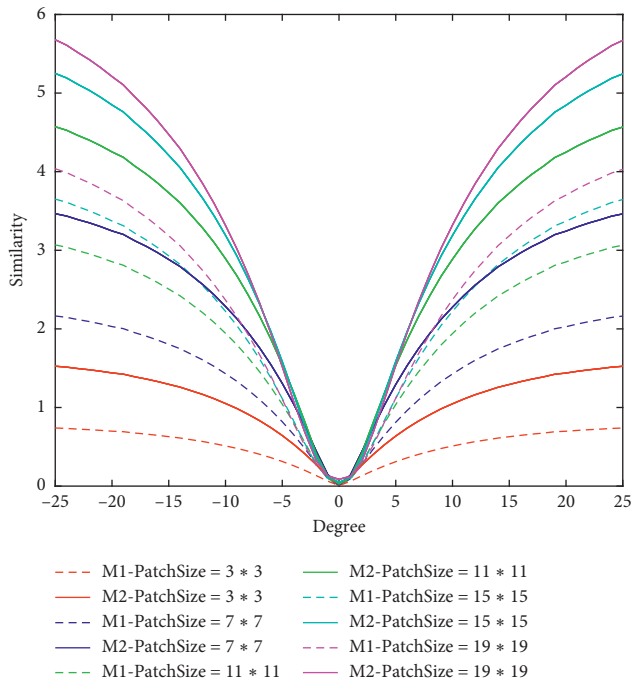

Figure 11: The similarity curves under different patch sizes, red curve $l = 3$, blue curve $l = 7$, green curve $l = 11$, cyan curve $l = 15$, and magenta curve $l = 19$. l is the side length of the patch. The dashed curve is M1 function and solid curve is M2 function. x label is rotation degree; y label is similarity value.

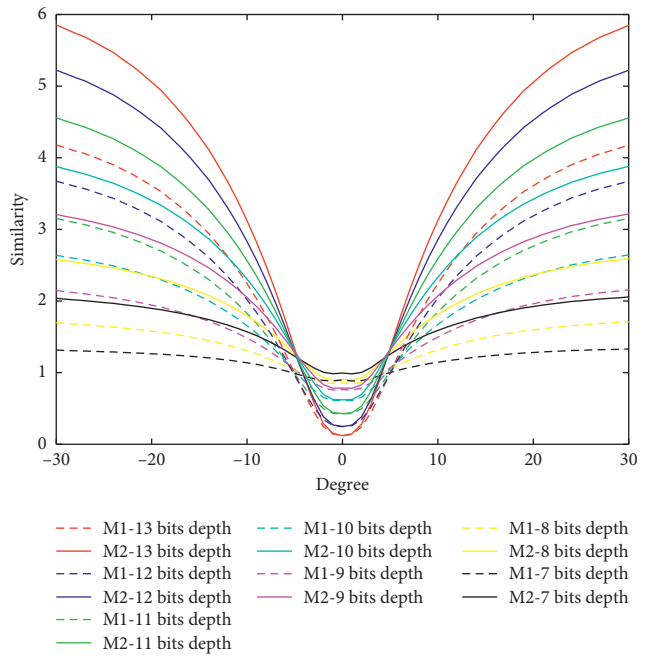

Figure 12: The similarity curves under the condition of different bit depths. The dashed curve is M1 function and solid curve is M2 function; x label is rotation degree; y label is similarity value.

modalities. We compute the similarity when rotating one modality image along the centre of the other modality image from −30 degree to 30 degree.

Figure 12 shows, as the bit depth decreases (from 13 to 7), the rate of converging to extremum is going to decrease. No matter what bit depth is, the M2 function can bring a faster converging rate than the M1 function when quantifying the uncertainty of the patch. There are some differences in minimum part when comparing Figure 12 with Figure 11. The minimum increases as the bit depth decreases, which causes the standard deviation of M2 curve to be larger than M1 curve, especially when the bit depth is large. The red pair and black pair curves prove that M2 function can quantify the value of uncertainty in a wider range, which can bring a

more representative structure descriptor set. This structure descriptor set is a key point in fast convergence.

5.4. Modality-Group Similarity Experiment on Rigid Deformation. The purpose of this experiment is to verify the sensitivity of the algorithm. As slice spacing decreases, it is hard to distinguish adjacent slices, which results in the deviation of many multimodal similarity algorithms. To verify our method's validation, we performed modality-group similarity experiment with 4 different methods: (1) the proposed method in [8] using entropy (M1 function) images, (2) the method using Laplacian method in manifold learning [14], (3) multimodal registration with mutual information (MI) [4], and (4) traditional method with mean absolute differences (MAD). The above result of the experiment is illustrated on Tables 2–4.

Finally, we evaluate the performance relationship between these four functions under the condition of side length $l = 15$, Parzen-window estimation, and modified weighting. This data set is from http://www.bic.mni.mcgill.ca/brainweb/. It includes three modalities: T1, T2, and PD. The brain MR image we selected on BrainWeb contains 3% noise and 20% intensity nonuniformity. There are 177 images in each of the three modalities, and we search an image in one of the modalities and then traverse all the images in the remaining modality. We make a comparison by group experiments to reflect the superiority of M1, M2, M3, and M4. All data sets provide standard alignment. Each data set makes 177 times registrations under each function. The experiment process is shown in Figure 13.

The blue point moves from left to right, and each action we calculate $177x$ values (i.e. similarity values). Finding the minimum value to judge that if the extreme value position ($P_{x_{\text{ext}}}^{\text{search}}$) is corresponding to the given original image position ($P_{x_{\text{ext}}}^{\text{reference}}$) or not. The ground truth of each data set is available on downloading the data set. It can be our reference standard state to compare with our experiment results. And we divide the results of comparison into 3 levels within the permissible margin of the error. If the position distance fulfils $P_{x_{\text{ext}}}^{\text{search}} - P_{x_{\text{ext}}}^{\text{reference}} = +1$, it is called the right deflection; if $P_{x_{\text{ext}}}^{\text{search}} - P_{x_{\text{ext}}}^{\text{reference}} = -1$, it is called the left deflection; if $P_{x_{\text{ext}}}^{\text{search}} - P_{x_{\text{ext}}}^{\text{reference}} = 0$, it is called the zero deflection (best match) in Figure 14. That means, the extreme value location should be the same or close as another modal location. Take the PD modality no. 3 layer as an example, we find the most similar image with PD modal from the T1 modal. If the result belongs to any one of no. 2, 3, and 4 layers, we consider these results are in the reasonable error range. And if $2 - 3 = -1$, it deflects one layer toward the superior; $3 - 3 = 0$, it does not deflect to any layers; the last $3 - 2 = 1$, it deflects one layer toward the inferior. If $|P_{x_{\text{ext}}}^{\text{search}} - P_{x_{\text{ext}}}^{\text{reference}}| > 1$, it means the registration is failed. So, the results are shown in Tables 2–4. (R-right; L-left; D-deflection; N-number; P-probability; Z-zero. For example, LDN is an abbreviation for "left deflection number" SUM = RDN + LDN + ZDN). We make 177 times experiments by each method.

According to the result in Tables 2–4, ZDP has more strict restriction than SUM probability. For M2, it can reach 92.66% in ZDP part, whereas M1 can only reach 84.16%. For MI, it has a slight trend in deflection, which makes LDN and RDN reaching 15 and 12, respectively. For manifold learning, it has a similar result with MI in LDN and RDN. For MAD, it is the worst method in modality-group experiments. The ZNP and SUM probability in MAD only reach 2.26% and 24.86%, respectively.

In contrast to the M2 method, it can be seen that the method has less number in RDN and LDN, which means has stronger ability to distinguish the adjacent slices. The result proves that the MAD method is unsuitable to compute the L2 norm of original multimodal image pairs, especially in M1-M2 group.

5.5. Modality-Group Similarity Experiment on Nonrigid Deformation. On the Brainweb databases, we deform one image in each pair with a deformation d_g regarded as the ground truth. Then, we estimate deformation d_c by registering the deformed image and another remained image with different modality one. We calculate the average Euclidean difference of the deformation fields $\tau = 1/|\Omega| \sum_{x \in \Omega} \| d_c(x) - d_g(x) \|$ for computing the residual error of the registration.

In Table 5, the configuration for M2 method for deformable registration is: $25 * 25$ patches, 16 bins, modified Gaussion weighting, local normalization, Parzen-window estimation and logarithmic fuzzy entropy core function. It can be seen that M2 has the lowest errors in 3 group registration. The results for the M1 (entropy) images are comparable, while the MAD does not perform well.

To test the effect of our method in nonrigid deformation, we used abdominal image of MRI-T1 and MRI-T2. The size of image pair is $384 * 384$ and a pixel is stored as 12 bits. The result is shown in Figure 15. In each method, we use a common slice (T1 modality) as fixed image, and the other corresponding slice is deformed by 200 manually warping operations such as TPS or affine. In these many fixed deformations, we use 5 methods (M1, M2, MI, manifold ling, and MAD) to find the most similar deformed image of their own. Their most similar result is shown in the Registered (T2) row of Figure 15. We can see that the M2 method has better performance on the image fusion from checkboard.

5.6. Translation Experiment. For the next translation experiment, we compared the performance of M2 (logarithmic fuzzy entropy function) with M1 (entropy function), MI (mutual information), and MAD (L1 norm). The results of the translational experiments under four methods can be seen in Figure 16.

Table 2: In the T1-T2 data set, the accuracy is within 5 methods.

Method	RDN	LDN	ZDN	SUM	ZDP (%)	SUM probability (%)
M1	7	15	149	171	84.18	96.61
M2	2	8	164	174	**92.66**	98.31
MI	15	12	121	148	68.36	83.26
Manifold learning	10	11	139	160	79.66	90.40
MAD	22	18	4	44	2.26	24.86

Table 3: In the T1-PD data set, the accuracy is within 5 methods.

Method	RDN	LDN	ZDN	SUM	ZDP (%)	SUM probability (%)
M1	9	21	140	170	79.10	96.05
M2	3	6	166	175	**93.79**	98.87
MI	29	24	110	163	62.15	92.09
Manifold learning	21	18	125	164	70.62	92.66
MAD	40	72	18	130	10.17	73.45

Table 4: In the T2-PD data set, the accuracy is within 5 methods.

Method	RDN	LDN	ZDN	SUM	ZDP (%)	SUM probability (%)
M1	13	20	136	169	76.84	95.48
M2	3	3	169	175	**95.48**	98.87
MI	35	29	99	163	55.93	92.09
Manifold learning	29	29	108	166	61.02	93.78
MAD	42	71	15	128	8.47	72.32

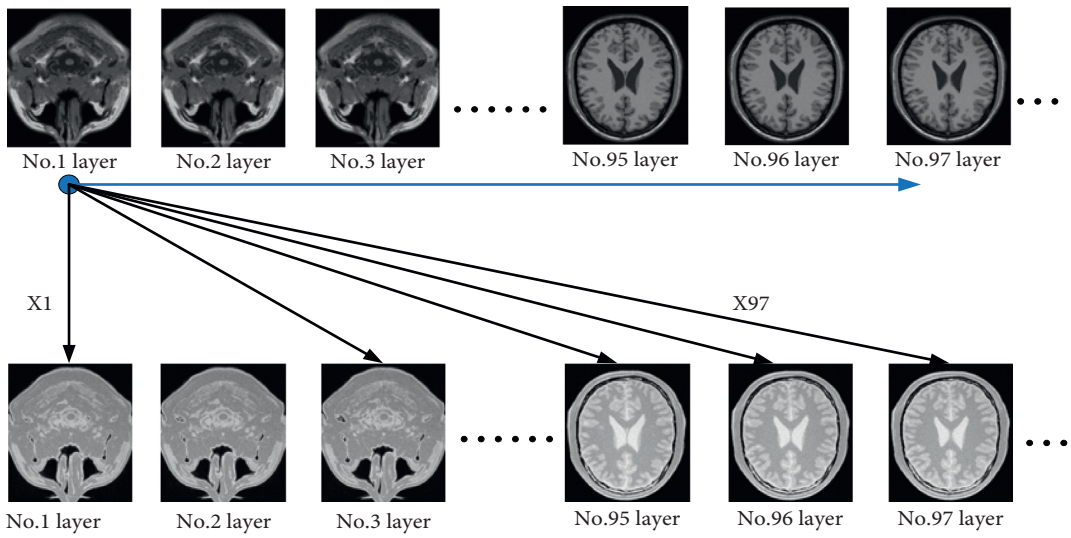

Figure 13: Experiment on accuracy verification.

As two images are translated along the x and y axes in [−40, 40] degrees, the similarity values are calculated by four methods for each degree. For M1 M2 and MAD, as the result is closer to 0, we obtained a stronger correlation between the two images. For MI, as the result is closer to 1, we obtained a stronger correlation between the two images. It can be seen from the smoothness of a curve that M1 M2 and MI are superior to MAD at stability. MI shows a very sharp peak when the translation difference is in the interval [−20, 20], and the system is relatively sensitive. But in [−40, −20] ∪ [20, 40], the method MI is not in our expectations because the similarity between the two images cannot distinguish clearly.

5.7. Running Time. Finally, we test the average time of 100 experiments during the normal registration. We select Parzen-windows estimation, modified weighting, and

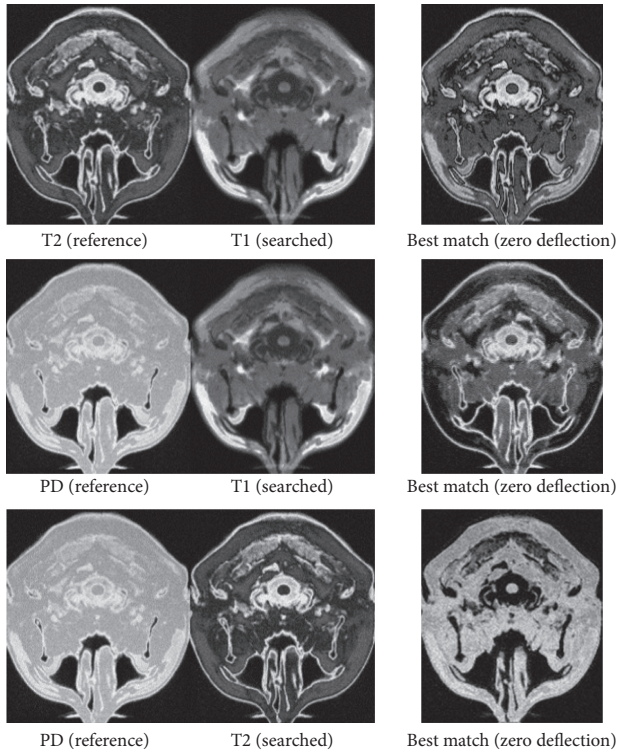

Figure 14: Optimal registration status under each data set.

Table 5: Registration errors τ in mm for various configurations for M2 method.

Sim	T1-T2	T1-PD	T2-PD
M1	0.52	0.61	0.58
M2	0.39	0.43	0.38
MI	0.68	0.76	0.70
Manifold learning	0.71	0.75	0.69
MAD	0.99	2.01	1.25

11×11 patch size at the experiment. Running time table is shown in Table 6:

We use MatlabR2016(b) to run code in a normal configuration environment (the process is from the descriptor set to the L1 norm registration). From Table 6, we can see the time of M1-M4 are shorter than MAD, which proves that using structure descriptor sets to calculate the L1 norm similarity is more efficient than using the original image directly. Besides, the M2 function has the shortest running time.

6. Discussion

Our proposed logarithmic fuzzy entropy function has a certain contribution on "transform multimodal into third modality." In this process, the ability of quantified patch is especially important. In Figure 2, we can see that the upper bound of our function is greater than the original function, especially in the large intensity level such as medical images, which can bring us a wide range for quantification. During the rigid and nonrigid registration experiments, the proposed method has good performance in measuring the similarity with an outstanding sensitivity. Regarding 3D, it is inevitable that the computational cost will increase as the dimension increases from 2D to 3D; however, it is not what our method worried about because it is not a complicate job for estimating the PDF (probability density function) of 3D patches. However, in this article, our method is to express the richness of the 2D patch with quantifying the uncertainty by a 1D number. From that view, our method will lose the location information, so we make it up by modified Gaussion weighting in chapter 4.2. If we apply this method on 3D situation, the quantifying process will plunge from 3D to 1D. Besides, there is no suitable 3D weighing that can offset the location information. So, this method does not have robustness in 3D multimodal image registration.

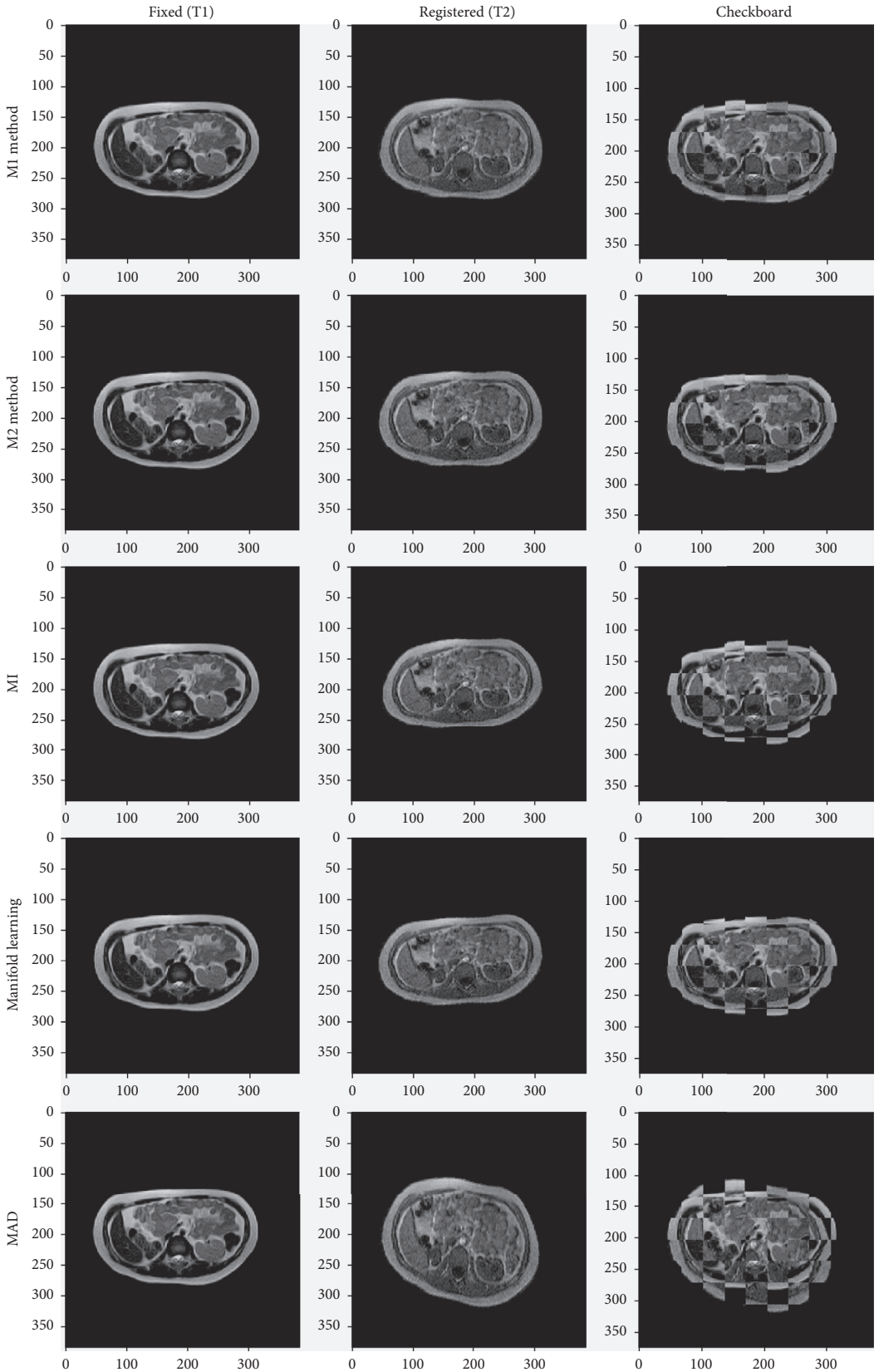

Figure 15: The experiment about one pairwise multimodal (T1-T2) image registration based on abdominal images.

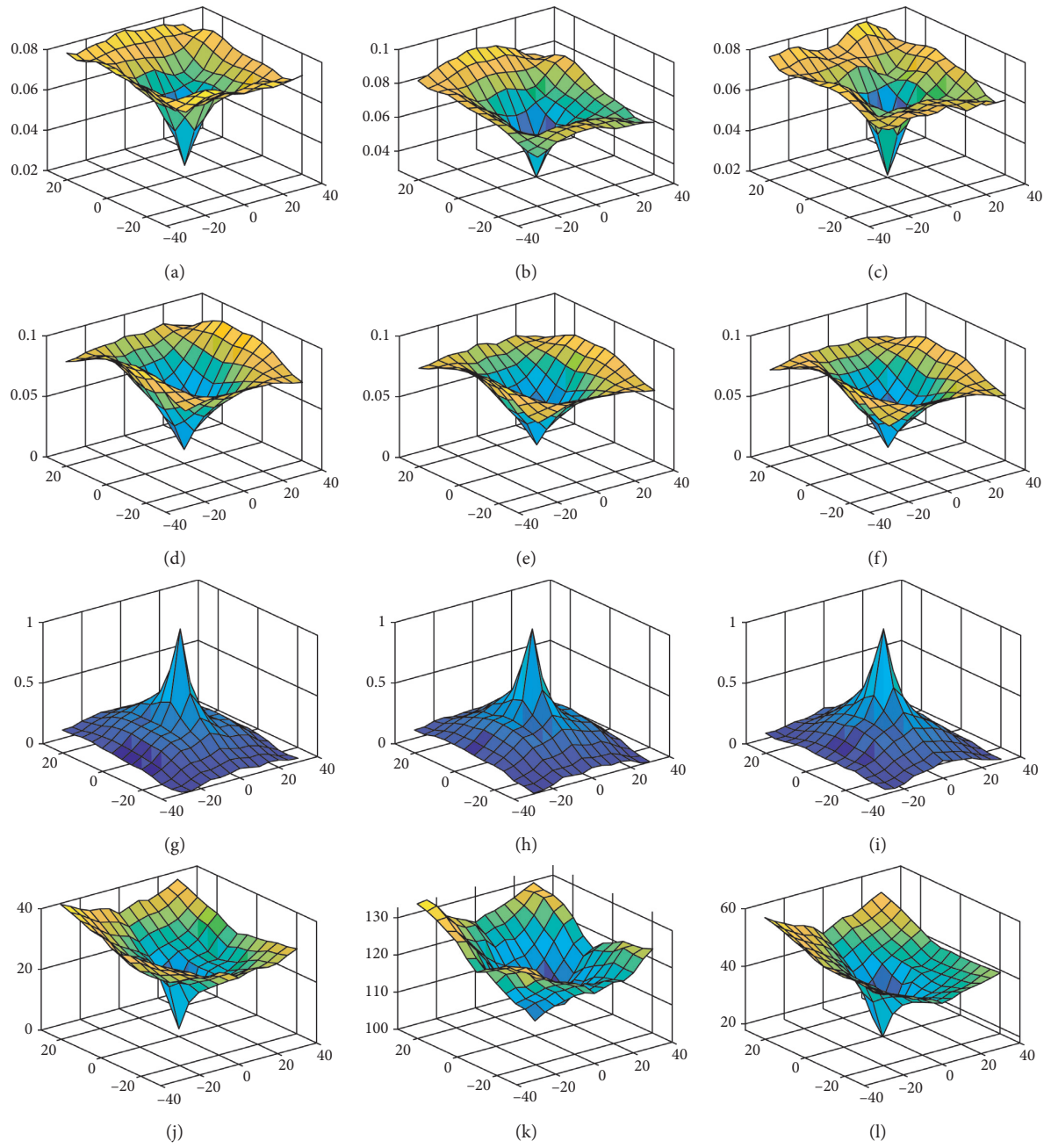

Figure 16: Plot of similarity measures for translation in the x and y directions. (a) M1, T1-T2. (b) M1, T1-PD. (c) M1, T2-PD. (d) M2, T1-T2. (e) M2, T1-PD. (f) M2, T2-PD. (g) MI, T1-T2. (h) MI, T1-PD. (i) MI, T2-PD. (j) MAD, T1-T2 (k) MAD, T1-PD. (l) MAD, T2-PD.

Table 6: Running time table.

Method	Use normal registration framework's time(s)
M1	0.0048
M2	0.0039
MI	0.0070
Manifold learning	0.0096
MAD	0.0672

7. Conclusion

This article focuses on using the structure descriptor sets (third-type artificial modality) to perform the L1 norm in multimodal registration. We propose logarithmic fuzzy entropy function in the computing structure descriptor set. Through the mathematical derivation and experimental result, this function is more suitable than entropy in

multimodal registration. We also tried out other two strict concave functions such as M3 and M4, but they performed worse because of their upper bound curve.

When we quantify the value of a patch by its intensity distribution, the advantages of logarithmic fuzzy entropy function are as follows:

(1) Mathematically, it can bring a larger quantification range.

(2) Experimentally, it can bring a faster convergence rate in similarity curve.

According to the experiments in chapter 5.4 to 5.6, our proposed method is an effective evaluating approach in similarity of multimodal medical images. It has the following advantages:

(1) Inferior computational complexity, which is the process from core function to L2 norm.

(2) Universal adaptability, which can work on any modality pair.

(3) Higher accuracy, which has strong ability to distinguish similar slices.

This algorithm has an obvious effect when the medical images are stored by high effective bit depth. Because the upper bound of quantification range is monotone, the function of variety degree r increases. To avoid duplicated values of different patches which have the same intensity distribution, the patch size will be as large as possible. However, the patch size influences not only the converging rate of similarity value but also the running time; a large patch can increase the running time. Ideally, we want l^2 and 2^n to be equal. But in practice, patch size depends on many factors such as, original image size, effective bit depth, noise, and requirement of running time. Whatever size it is, the logarithmic fuzzy entropy function is a good choice in the "transfer of multimodal into third-type modality" medical image registration.

Data Availability

Data link available: Brain Web (http://www.bic.mni.mcgill.ca/brainweb/) DICOM Library (https://www.dicomlibrary.com).

Conflicts of Interest

There is no conflicts of interest regarding the publication of this paper.

Acknowledgments

This work is supported by the Science and Technology Development Program of Jilin Province, China (Nos. 20170-204031GX, 20180201037SF, 20190201196JC and 201903-02112GX), the National Key Research and Development Program of China under Grant no. 2017YFC0108303, and the Science and Technology Development Program of Jilin Province, China (No. 2018C039-1).

References

[1] J. Zhou and Q. Liu, "A combined similarity measure for multimodal image registration," in *Proceedings of the 2015 IEEE International Conference on Imaging Systems and Techniques (IST)*, pp. 1–5, Macau, China, September 2015.

[2] F. P. M. Oliveira and J. M. R. S. Tavares, "Medial image registration: a review," *Computer Methods in Biomechanics and Biomedical Engineering*, vol. 17, no. 8, pp. 73–93, 2014.

[3] F. Maes, D. Vandermeulen, and P. Suetens, "Medical image registration using mutual information," *Proceedings of the IEEE*, vol. 91, no. 10, pp. 1699–1722, 2003.

[4] D. B. Russakoff, C. Tomasi, T. Rohlfing, and C. R. Maurer, "Image similarity using mutual information of regions," in *Computer Vision—ECCV 2004*, T. Pajdla and J. Matas, Eds., pp. 596–607, Springer, Berlin, Heidelberg, 2004.

[5] D. Loeckx, P. Slagmolen, F. Maes, D. Vandermeulen, and P. Suetens, "Nonrigid image registration using conditional mutual information," *IEEE Transactions on Medical Imaging*, vol. 29, no. 1, pp. 19–29, 2010.

[6] W. Wein, S. Brunke, A. Khamene, M. R. Callstrom, and N. Navab, "Automatic CT-ultrasound registration for diagnostic imaging and image-guided intervention," *Medical Image Analysis*, vol. 12, no. 5, pp. 577–585, 2008.

[7] L. Xu, J. Liu, W. Zhan, and L. Gu, "A novel algorithm for ct-ultrasound registration," in *Proceedings of the 2013 IEEE Point-of-Care Healthcare Technologies (PHT)*, pp. 101–104, Bangalore, India, January 2013.

[8] C. Wachinger and N. Navab, "Entropy and laplacian images: structural representations for multi-modal registration," *Medical Image Analysis*, vol. 16, no. 1, pp. 1–17, 2012.

[9] M. P. Heinrich, M. Jenkinson, M. Bhushan et al., "Mind: modality independent neighbourhood descriptor for multi-modal deformable registration," *Medical Image Analysis*, vol. 16, no. 7, pp. 1423–1435, 2012.

[10] O. Oktay, A. Schuh, M. Rajchl et al., "Structured decision forests for multi-modal ultrasound image registration," in *Proceedings of the International Conference on Medical Image Computing and Computer-Assisted Intervention*, pp. 363–371, Munich, Germany, October 2015.

[11] M. Simonovsky, B. Gutiérrez-Becker, D. Mateus, N. Navab, and N. Komodakis, "A deep metric for multimodal registration," in *Proceedings of the International Conference on Medical Image Computing and Computer-Assisted Intervention*, pp. 10–18, Athens, Greece, October 2016.

[12] X. Cao, J. Yang, Y. Gao, Y. Guo, G. Wu, and D. Shen, "Dual-core steered non-rigid registration for multi-modal images via bi-directional image synthesis," *Medical Image Analysis*, vol. 41, pp. 18–31, 2017.

[13] J. Luo, S. Frisken, I. Machado, and M. Zhang, "Using the variogram for vector outlier screening: application to feature-based image registration," *International Journal of Computer Assisted Radiology and Surgery*, vol. 13, no. 2, pp. 1871–1880, 2018.

[14] F. Bashiri, A. Baghaie, R. Rostami, Z. Yu, and R. D'Souza, "Multi-modal medical image registration with full or partial data: a manifold learning approach," *Journal of Image*, vol. 5, no. 1, p. 5, 2019.

[15] T. M. Buzug, J. Weese, C. Fassnacht, and C. Lorenz, "Image registration: convex weighting functions for histogram-based similarity measures," in *CVRMed-MRCAS'97*, J. Troccaz, E. Grimson, and R. Mösges, Eds., pp. 203–212, Springer, Berlin, Germany, 1997.

[16] J. P. W. Pluim, J. B. A. Maintz, and M. A. Viergever, "<><>f-information measures in medical image registration," *IEEE Transactions on Medical Imaging*, vol. 23, no. 12, pp. 1508–1516, 2004.

[17] E. García, Y. Diez, O. Diaz et al., "Breast MRI and X-ray mammography registration using gradient values," *Medical Image Analysis*, vol. 54, pp. 76–87, 2019.

[18] M. J. Wierman, "Measuring uncertainty in rough set theory," *International Journal of General Systems*, vol. 28, no. 4-5, pp. 283–297, 1999.

[19] I. Düntsch and G. Gediga, "Uncertainty measures of rough set prediction," *Artificial Intelligenceficial Intelligence*, vol. 106, no. 1, pp. 109–137, 1998.

[20] C. Yumin, X. Yu, M. Ying, and X. Feifei, "Measures of uncertainty for neighborhood rough sets," *Knowledge Based Systems*, vol. 120, pp. 226–235, 2017.

[21] G. S. Huang and H. Wen, "Uncertainty measures of rough set based on strictly concave functions," *Ruan Jian Xue Bao/ Journal of Software*, vol. 29, pp. 3484–3499, 2018.

[22] W. Wei, J. Liang, Y. Qian, and C. Dang, "Can fuzzy entropies be effective measures for evaluating the roughness of a rough set?," *Information Sciences*, vol. 232, pp. 143–166, 2013.

[23] L. De and S. Termini, "A definition of a non-probabilistic entropy in the setting of fuzzy sets theory," *Information and Control*, vol. 20, no. 4, pp. 301–312, 1972.

[24] N. R. Pal and S. K. Pal, "Entropy: a new definition and its applicationsfinition and its applications," *IEEE Transactions on Systems, Man, and Cybernetics*, vol. 21, no. 5, pp. 1260–1270, 1991.

[25] R. McEliece, "The theory of information and coding," *Encyclopedia of Mathematics and its Applications*, Vol. 86, Cambridge University Press, Cambridge, UK, 2nd edition, 2002.

Hindawi
Computational and Mathematical Methods in Medicine
Volume 2020, Article ID 3290136, 13 pages
https://doi.org/10.1155/2020/3290136

Research Article

Research of Multimodal Medical Image Fusion Based on Parameter-Adaptive Pulse-Coupled Neural Network and Convolutional Sparse Representation

Jingming Xia,[1] Yi Lu ,[1] and Ling Tan [2]

[1]*School of Electronics and Information Engineering, Nanjing University of Information Science & Technology, Nanjing 210044, China*
[2]*School of Computer and Software, Nanjing University of Information Science & Technology, Nanjing 210044, China*

Correspondence should be addressed to Yi Lu; luyi0423@nuist.edu.cn

Received 12 September 2019; Revised 7 December 2019; Accepted 2 January 2020; Published 24 January 2020

Guest Editor: Adam Konefal

Visual effects of medical image have a great impact on clinical assistant diagnosis. At present, medical image fusion has become a powerful means of clinical application. The traditional medical image fusion methods have the problem of poor fusion results due to the loss of detailed feature information during fusion. To deal with it, this paper proposes a new multimodal medical image fusion method based on the imaging characteristics of medical images. In the proposed method, the non-subsampled shearlet transform (NSST) decomposition is first performed on the source images to obtain high-frequency and low-frequency coefficients. The high-frequency coefficients are fused by a parameter-adaptive pulse-coupled neural network (PAPCNN) model. The method is based on parameter adaptive and optimized connection strength β adopted to promote the performance. The low-frequency coefficients are merged by the convolutional sparse representation (CSR) model. The experimental results show that the proposed method solves the problems of difficult parameter setting and poor detail preservation of sparse representation during image fusion in traditional PCNN algorithms, and it has significant advantages in visual effect and objective indices compared with the existing mainstream fusion algorithms.

1. Introduction

The diversity of image capture mechanisms allows different patterns of medical images to reflect different organ and tissue information categories. For example, computed tomography (CT) is very sensitive to blood vessels and bones and thus its imaging is more clearly. Magnetic resonance imaging (MRI) images provide richer soft-tissue information but lack boundary information and blur the bone imaging [1]. Emission computed tomography (ECT), which includes positron emission tomography (PET) and single-photon emission computed tomography (SPECT), captures projected data and reconstructs tomography images with high sensitivity but low resolution. The purpose of pixel-level medical image fusion technology is to obtain more useful and accurate medical information for the same target by combining the complementary information in multimodal medical images through composite image.

In recent years, medical image fusion algorithms have been greatly developed. However, most medical image fusion methods adopt the framework of multiscale transform (MST) to achieve better results. The image transformation method and the fusion strategy of high-frequency coefficients and low-frequency coefficients are the two key issues of MST-based fusion methods. A large number of studies have shown that the performance of MST-based fusion methods can be significantly improved by selecting appropriate image transform methods and designing effective fusion strategies. Singh et al. [2] proposed to add the pulse-coupled neural network (PCNN) to the fusion rule under the NSST framework to effectively extract the gradient features and preserve the edge and detail information of the source

images, but many parameter settings in PCNN are also a major challenge. Liu et al. [3] raised a convolutional sparse representation algorithm, which properly solved the two problems of sparse representation arising in image fusion, i.e., limited ability to preserve details and high sensitivity to registration errors [4, 5] and accomplished the image fusion by implementing a sparse representation of the entire image. Chen et al. [6] proposed an image segmentation method based on a simplified PCNN model (SPCNN). This model can automatically set the size of PCNN-free parameters to achieve higher segmentation accuracy. Ming et al. [7] improved the SPCNN model and obtained an improved parameter-adaptive PCNN model (PAPCNN) and applied it to image fusion. Experiments showed that the PAPCNN model has a faster convergence rate as well as a preferable effect when applied to the image fusion experiment.

Aiming at the problems existing in the current PCNN and NSST methods, an NSST-PAPCNN-CSR algorithm combining NSST, CSR, and PAPCNN models was proposed. The innovations of this paper are outlined as follows:

(1) We adopt the parameter-adaptive PCNN (PAPCNN) to fuse high-frequency coefficients with all the PCNN parameters adaptively calculated based on the input bands, which can overcome the difficulty of setting free parameters in the conventional PCNN models. Besides, we propose an improved implicit parameter β of PAPCNN, and the synchronous ignition characteristics in the PAPCNN model were coordinated to achieve a better fusion effect.

(2) We introduce the convolutional sparse representation (CSR) model into the fusion of low-frequency coefficients. The CSR model overcomes the two key issues of sparse representation arising in image fusion, i.e., limited ability to preserve details and high sensitivity to registration errors. In addition, the CSR is expected to solve the sparseness problem of the low-frequency coefficients in the NSST domain.

The rest of this paper is organized as follows. In Section 2, materials and methods used in the paper are briefly introduced. Section 3 gives the experiments and analysis. Finally, this paper is concluded in Section 4.

2. Materials and Methods

2.1. Related Materials

2.1.1. Non-Subsampled Shearlet Transform (NSST). The NSST decomposes the source image through the non-subsampled pyramid filter (NSPF) and the shift-invariant shear filter bank (SFB). NSPF can guarantee the shift-invariance and suppress the pseudo-Gibbs phenomenon, and SFB can achieve the directional localization. Figure 1 is a schematic diagram of the NSST decomposition. NSST is recognized as a very reliable image fusion method with good local time-domain features, multidirectionality, and translation invariance. It can effectively extract the edge and detail information in the source image [2, 8]. On account of this, NSST was selected as the MST method of image fusion.

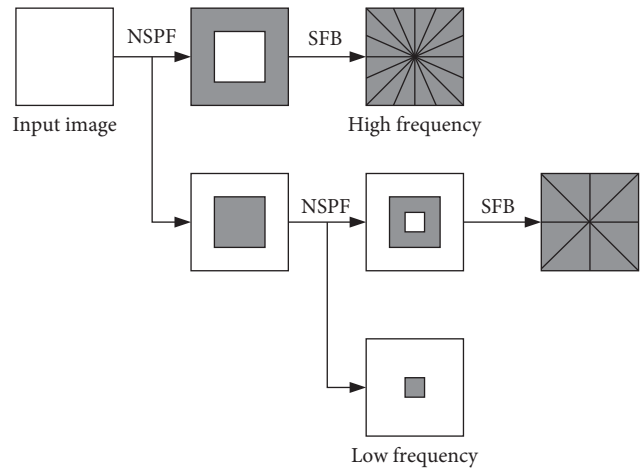

Figure 1: Schematic diagram of NSST decomposition.

2.1.2. Parameter-Adaptive Pulse-Coupled Neural Network (PAPCNN) and Improvement of the Parameter β. The key challenge in the traditional PCNN model is how to set free parameters such as connection strength, various amplitudes, and attenuation coefficients. To avoid difficulties in manually setting free parameters, in this paper, a parameter-adaptive PCNN (PAPCNN) model [7] was proposed to fuse the high-frequency coefficients obtained by NSST decomposition.

The PAPCNN model is described as follows:

$$F_{ij}[n] = S_{ij}, \tag{1}$$

$$L_{ij}[n] = V_L \sum_{kl} W_{ijkl} Y_{kl}[n-1], \tag{2}$$

$$U_{ij}[n] = e^{-\alpha_f} U_{ij}[n-1] + F_{ij}[n]\left(1 + \beta L_{ij}[n]\right), \tag{3}$$

$$Y_{ij}[n] = \begin{cases} 1, & \text{if } U_{ij}[n] > E_{ij}[n-1], \\ 0, & \text{otherwise}, \end{cases} \tag{4}$$

$$E_{ij}[n] = e^{-\alpha_e} E_{ij}[n-1] + V_E Y_{ij}[n]. \tag{5}$$

In the PAPCNN model mentioned above, $F_{ij}[n]$ and $L_{ij}[n]$ represent the input and connection input of the neurons at the position of the iteration n, respectively. Figure 2 shows the structure of the PAPCNN model.

There are five parameters in the PAPCNN model: the attenuation coefficient α_f of the dynamic threshold E, the connection strength β, the amplitude V_L of the connected input, the attenuation coefficient α_e of the internal activity U, and the amplitude V_E of the dynamic threshold E. Also, it can be observed from (1) to (5) that β or V_L only serves as the weight of $\sum_{kl} W_{ijkl} Y_{kl}[n-1]$, so they can be treated as a whole βV_L in the PAPCNN model. Supposing that $\lambda = \beta V_L$ represents the weighted connection strength, we analyze the value of parameter V_L according to the literature [6] and assume $V_L = 1$ without influence on the final experimental results; therefore, there are four parameters: α_f, α_e, V_E, and λ.

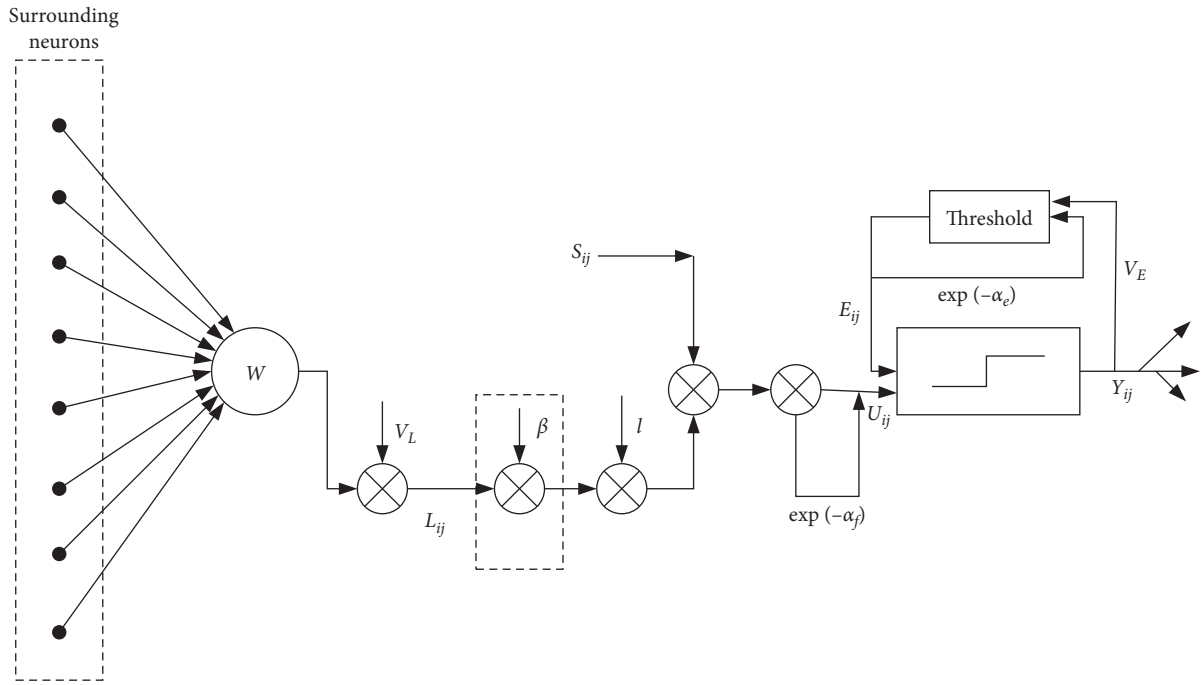

Figure 2: Structure of the PAPCNN model.

In this paper, we have adjusted the parameter β, i.e., the connection strength between neurons. Because the value of V_L is fixed, the larger the value of β is, the greater the neuron is affected by its neighboring neurons, and the more intense the fluctuation of its internal activity $U_{ij}[n]$. Generally, the larger value of β tends to cause low-light neurons to ignite; conversely, the smaller value of β may reduce the ability to capture the neighboring neurons. To coordinate the synchronous ignition characteristics of the PAPCNN model, an optimization method is introduced in this paper to search the value of β [9]:

$$\begin{aligned} &\min_{\beta} \quad \sum_{c=1}^{2} \lambda_c \sum_{x \in X_c} \left(I_x - m_c(n)\right)^2, \\ &\text{s.t.} \quad \mathrm{X}_1 = \left\{y \mid U_y(n) \le E_y(n-1)\right\} \cap X, \\ &\qquad \mathrm{X}_2 = \frac{X}{X_1}, 0 \le \beta \le 1, \end{aligned} \tag{6}$$

where λ_1 and λ_2 are the weight coefficients, set to 1 and X indicates the set of neighboring neurons and is generally calculated by

$$X = \left\{ij \mid L_{ij}(n) > 0\right\} \cap \left\{ij \mid Y_{ij}(n) = 0\right\}, \tag{7}$$

where $m_1(n)$ and $m_2(n)$ indicate, respectively, the mean value corresponding to the unfired and ignition areas, as shown in the following equation:

$$m_c(n) = \frac{\sum_{ij \in \Omega_c} F_{ij}}{\sum_{ij \in \Omega_c} 1}, \quad c = 1, 2, \tag{8}$$

where $\Omega_1 = \left\{ij \mid Y_{ij}(n-1) = 0\right\}$ and $\Omega_2 = \left\{ij \mid Y_{ij}(n-1) = 0\right\}$. It can be seen from equation (6) that β, as an implicit parameter, changes the optimal value of the objective function. It essentially regulates the internal ignition activity U of the neighboring neurons, and later, by comparison with the threshold E, the neighboring neurons divided into two categories: X_1 and X_2. To this end, its corresponding gray value information and the dispersion degree of mean value in equation (8) were considered to determine the optimal connection coefficient β. To facilitate the calculation, the search method of increasing the step size $\Delta\beta$ was adopted.

2.1.3. Convolutional Sparse Representation (CSR). Convolutional sparse representation is a convolutional form of sparse representation, that is, the convolutional sum of the filter dictionary and the characteristic response is used instead of the product of the redundancy dictionary and the sparse coefficient, so that the image is sparsely coded in the unit of "entirety." The convolutional sparse representation model can be expressed as

$$\arg\min_{x_m} \frac{1}{2} \left\| \sum_m d_m \otimes x_m - s \right\|_2^2 + \lambda \sum_m \left\| x_m \right\|_1, \tag{9}$$

where $\{d_m\}$ represents the M-dimensional convolution dictionary; $\otimes$ represents the symbol of the convolution operation; $\{x_m\}$ represents the characteristic response; s represents the source image; the alternating direction method of multipliers (ADMMs) is a dual convex optimization algorithm, which can solve the convex programming problem with separable structure by solving alternately several subproblems. In [10], considering that the ADMM algorithm could desirably solve the problem of Basis Pursuit De-Noising (BPDN), a Fourier domain ADMM algorithm was proposed to solve the solving problem of the

convolutional sparse model. Among them, dictionary learning is defined as the optimization problem of

$$\arg\min_{\{d_m\},\{x_m\}} \frac{1}{2}\left\| \sum_{m-1}^{M} d_m \otimes x_m - s \right\|_2^2 + \lambda \sum_{m-1}^{M} \left\| x_m \right\|_1, \quad \text{s.t.} \quad \left\| d_m \right\|_2 = 1. \tag{10}$$

The first application of the convolutional sparse representation to image fusion is described in the literature [5], which regards CSR as an alternative form of SR, to achieve sparse representation of the entire image, rather than partial image patches. The convolutional sparse representation algorithm overcomes the shortcomings of traditional sparse representation with limited ability to preserve details and high sensitivity to registration errors. We believe that it is also effective for the fusion of low-frequency coefficients. In particular, the application of the CSR model is very effective for the fusion of the low-frequency coefficients obtained by MST. The low-frequency coefficients obtained after the NSST decomposition represent the approximate description of the image, and there is a large number with the approximation of 0, which can sparsely represent the low-frequency information of the image. Based on the above considerations, the CSR model was introduced into the fusion of MST low-frequency coefficients.

2.2. Implementation of NSST-PAPCNN-CSR. Figure 3 shows the specific steps of image fusion. The preregistered multimodal source images were fused, and the detailed fusion method includes four steps: NSST decomposition, fusion of high-frequency coefficients, fusion of low-frequency coefficients, and NSST reconstruction.

Step 1. NSST decomposition.

The L-level NSST was used to decompose the source images A and B to obtain their coefficients $\{H_A^{l,k}, L_A\}$ and $\{H_B^{l,k}, L_B\}$, respectively, where $H_A^{l,k}$ is a high-frequency coefficient of image A in the decomposition order l and the decomposition direction k and L_A is the low-frequency coefficient of image A. For image B, $H_B^{l,k}$ and L_B had the same meaning.

Step 2. Fusion of high-frequency coefficients.

The PAPCNN model proposed in Section 2.1.2 was applied to the fusion of high-frequency coefficients [11]. Based on the discussion in Section 2.1.2, the absolute value graph of high-frequency coefficients was taken as the network input, namely, the feed input was $F_{ij}[n] = |H_s^{l,k}|$, $S \in \{A, B\}$. The activity level of high-frequency coefficients was measured by the total emission time throughout the iteration. According to the PAPCNN model described by Formulas (1)–(5), the trigger time was accumulated by adding the following steps at the end of each iteration:

$$T_{ij}[n] = T_{ij}[n-1] + Y_{ij}[n]. \tag{11}$$

The excitation time of each neuron was $T_{ij}[n]$ and N is the total number of iterations, corresponding to high-frequency coefficients $H_A^{l,k}$ and $H_B^{l,k}$. Their PAPCNN time could be calculated and expressed as $T_{A,ij}^{l,k}[n]$ and $T_{B,ij}^{l,k}[n]$. The fused coefficient was obtained in the following way:

$$H_F^{l,k}(i,j) = \begin{cases} H_A^{l,k}(i,j), & \text{if } \mathrm{T}_{A,ij}^{l,k}[N] \geq T_{B,ij}^{l,k}[N], \\ H_B^{l,k}(i,j), & \text{otherwise.} \end{cases} \tag{12}$$

The above formula shows that the coefficient with the larger number of ignitions was the final high-frequency fusion coefficient. The optimal value of the object function was acquired by adjusting the size of the implicit parameter β, to obtain the optimal high-frequency fusion coefficient.

Step 3. Fusion of low-frequency coefficients.

The fusion strategy of low-frequency coefficients also has a great influence on the final fusion quality. The convolutional sparse representation method was used to fuse low-frequency coefficients [12]. Suppose there were low-frequency coefficients after the decomposition of k source images and they were set L_k, $k \in \{1, \ldots, K\}$ and suppose a set of dictionary filters d_m, $m \in \{1, \ldots, M\}$. The specific implementation steps of the low-frequency coefficients fusion based on CSR are shown in Figure 3.

Step 4. NSST reconstruction.

Finally, the inverse NSST reconstruction was performed on the fusion band $\{H_F^{l,k}, L_F\}$ to obtain the fused image F.

3. Experiments and Analysis

3.1. Experimental Settings

3.1.1. Source Images. To verify the effectiveness of the proposed algorithm, 70 pairs of source pictures were used in the experiment. All of these source images are collected from the database of the Whole Brain Atlas of Harvard Medical School [13] and the Cancer Imaging Archive (TCIA) [14]. 50 pairs of source images from the database of Whole Brain Atlas include 10 pairs of CT and MR images, 10 pairs of T1-weighted (MR-T1) and T2-weighted (MR-T2) images, 15 pairs of MR and PET images, and 15 pairs of MR and SPECT images. 20 pairs of source images from the database of TCIA include 10 pairs of CT and MR images and 10 pairs of T1-weighted (MR-T1) and T2-weighted (MR-T2) images. All the source images have the same spatial resolution of 256×256 pixels. The source images in each pair have been accurately registered.

3.1.2. Objective Evaluation Metrics. The evaluation of image fusion quality is divided into subjective visual evaluation and objective index evaluation. The objective evaluation metrics is to select relevant indices to measure the effect of human visual system on image quality perception. To quantitatively evaluate the performance of different methods, six accepted

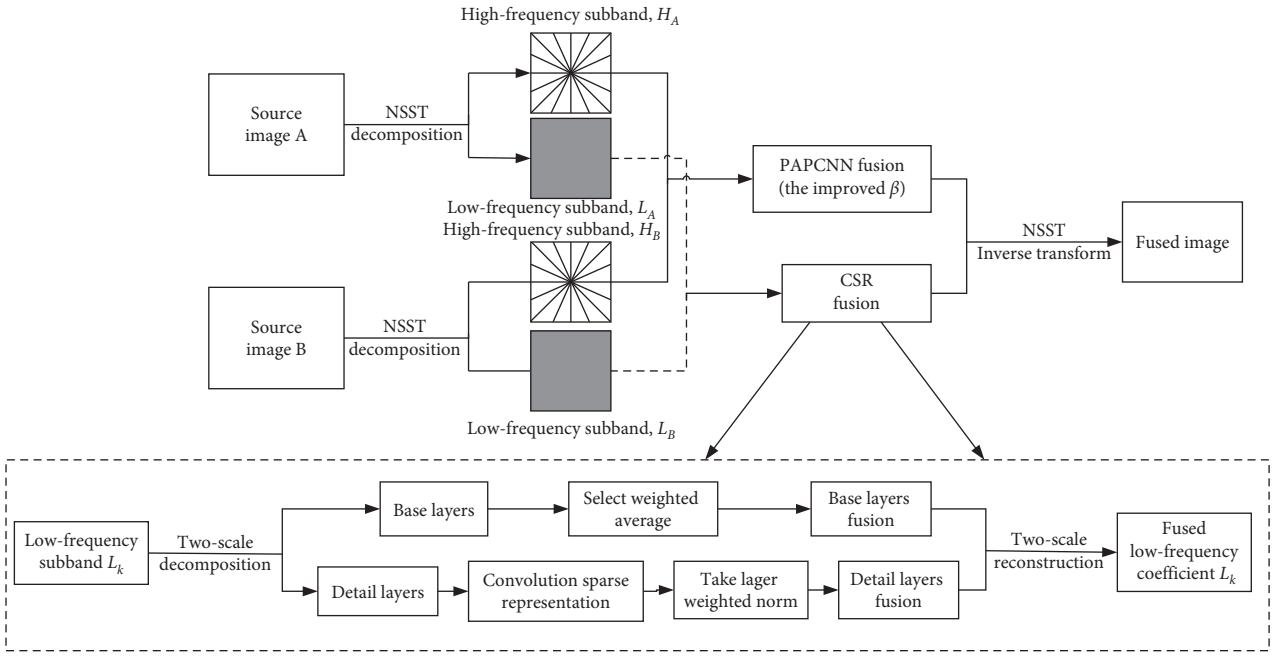

Figure 3: NSST-PAPCNN-CSR algorithm flow chart.

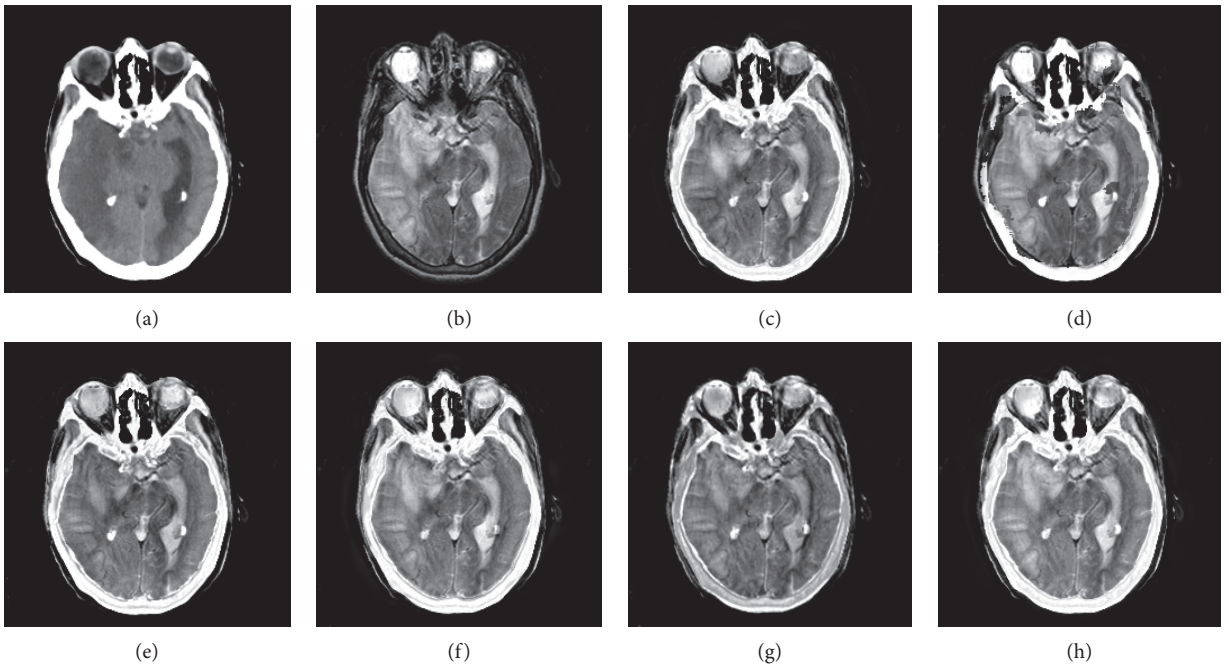

Figure 4: CT and MR medical image fusion results. (a) CT original image. (b) MR original image. (c) NSST-PAPCNN. (d) CSR. (e) MST-SR. (f) NSCT-SR-PCNN. (g) SR-PCNN. (h) Proposed.

objective fusion evaluation indices were selected in the experiment, i.e., entropy (EN) [15], edge information retention ($Q^{AB/F}$) [16], mutual information (MI), average gradient (AG), space frequency (SF), and standard deviation (SD) [17]. Entropy characterizes the amount of information available in the source image and the fused image; edge information retention characterizes the transfer amount of edge detail information in the source images injected into the fused image; mutual information is used to measure the information of the fused image contained in the used image; average gradient can be used to represent the sharpness of the image, and the larger the value, the clearer the image; space frequency reflects the overall activity of the image in the space domain, and its size is proportional to the image fusion effect; standard deviation reflects the dispersion degree of the pixel value and mean value of the image, and the greater the deviation, the better the quality of the image. In general, for all the above six metrics, a larger score indicates a better performance.

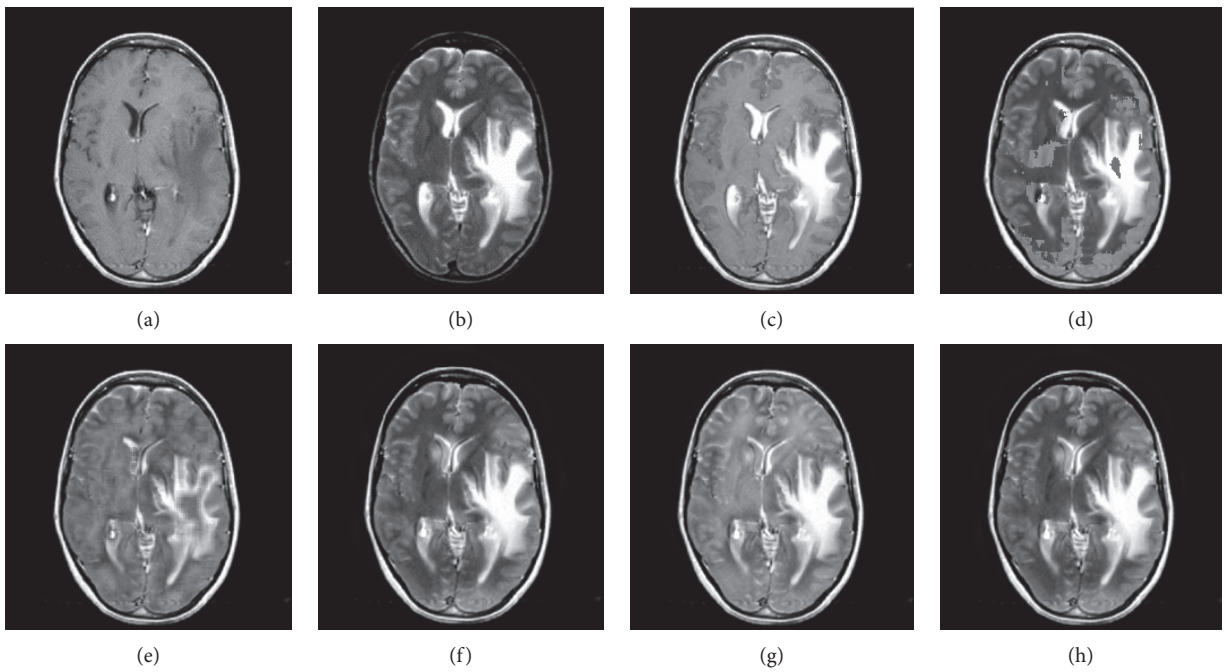

Figure 5: CT and MR medical image fusion results. (a) CT original image. (b) MR original image. (c) NSST-PAPCNN. (d) CSR. (e) MST-SR. (f) NSCT-SR-PCNN. (g) SR-PCNN. (h) Proposed.

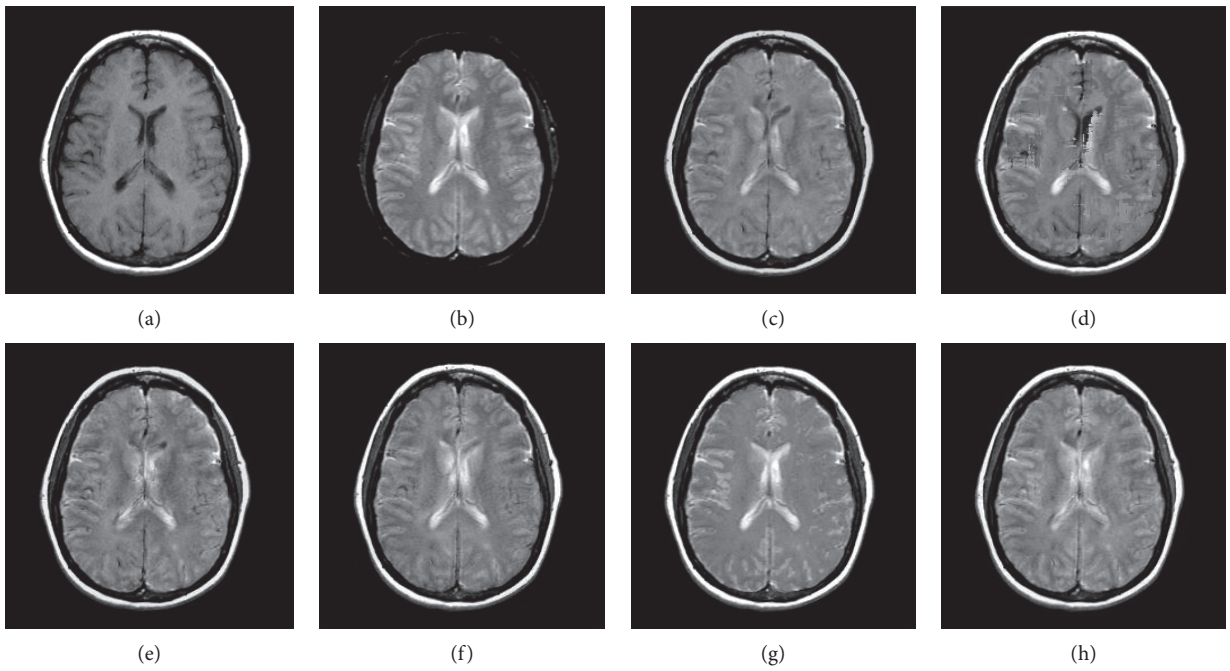

Figure 6: MR-T1 and MR-T2 medical image fusion results. (a) MR-T1 original image. (b) MR-T2 original image. (c) NSST-PAPCNN. (d) CSR. (e) MST-SR. (f) NSCT-SR-PCNN. (g) SR-PCNN, (h) Proposed.

3.1.3. Methods for Comparison. The proposed fusion method was compared with the existing five representative methods: the multimodal image fusion based on parameter-adaptive pulse-coupled neural network (NSST-PAPCNN) [7], the multimodal image fusion based on convolutional sparse representation (CSR) [5], the multimodal image fusion based on multiscale transform and sparse representation (MST-SR) [18], the multimodal image fusion based on sparse representation and pulse-coupled neural network (SR-PCNN) [19], and the multimodal image fusion based on non-subsampled contourlet transform and sparse representation and pulse-coupled neural network (NSCT-SR-PCNN) [10].

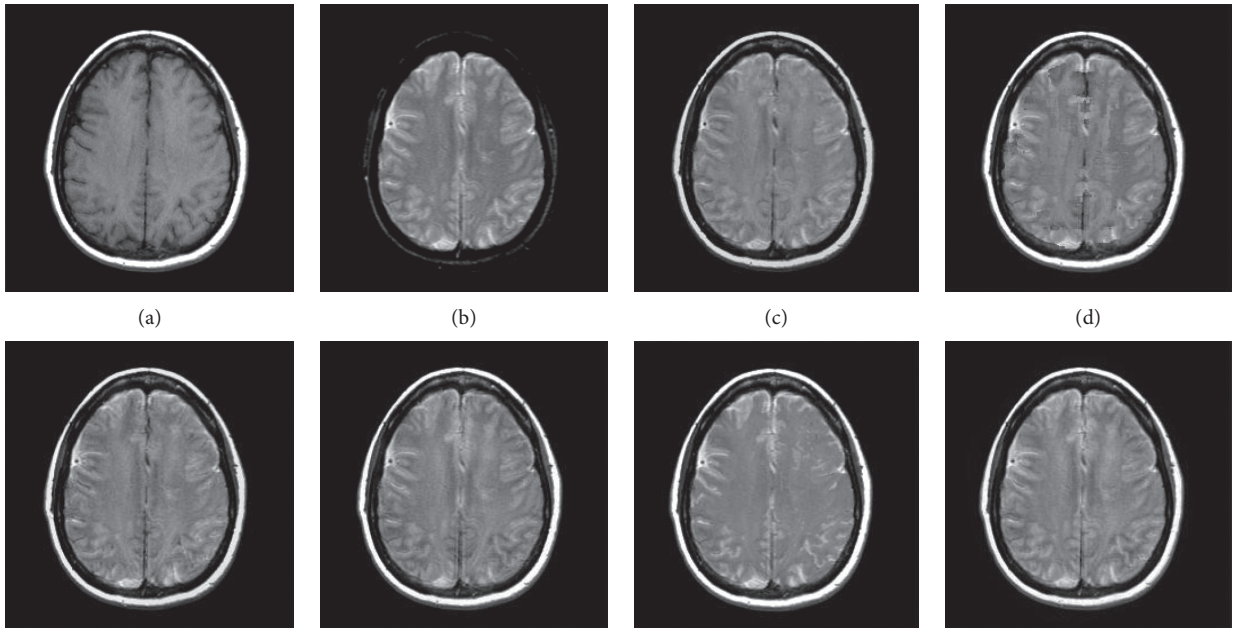

Figure 7: MR-T1 and MR-T2 medical image fusion results. (a) MR-T1 original image. (b) MR-T2 original image. (c) NSST-PAPCNN. (d) CSR. (e) MST-SR. (f) NSCT-SR-PCNN. (g) SR-PCNN, (h) Proposed.

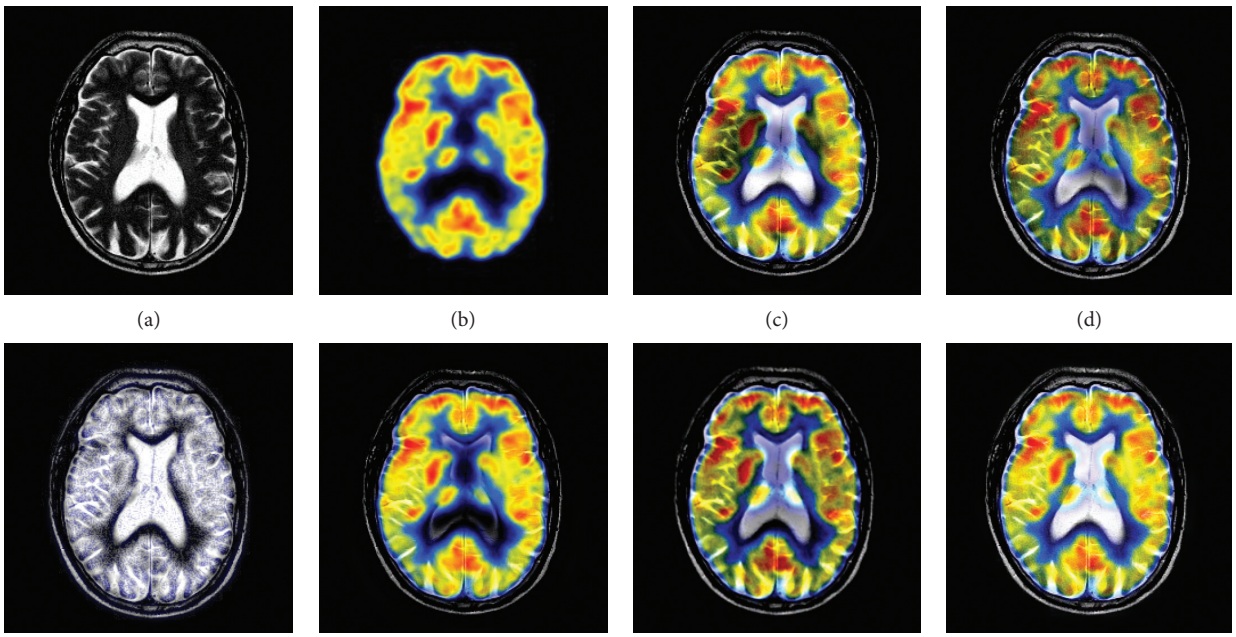

Figure 8: MR and PET medical image fusion results. (a) MR original image. (b) PET original image. (c) NSST-PAPCNN. (d) CSR. (e) MST-SR. (f) NSCT-SR-PCNN. (g) SR-PCNN. (h) Proposed.

3.1.4. Clinical Significance. The four types of medical image fusion have different clinical application value. For example, the fusion of CT and MR images can clearly display the location image of lesions and significantly reduce the surgical risk of visualized craniocerebral operation and the side effect of radiotherapy for craniocerebral lesions; the fusion of MR and SPECT images can determine epilepsy lesions in the neocortex of the brain based on local cerebral blood flow changes. Therefore, medical image fusion can combine the advantages of various imaging techniques and is of great significance in the diagnosis and treatment of diseases.

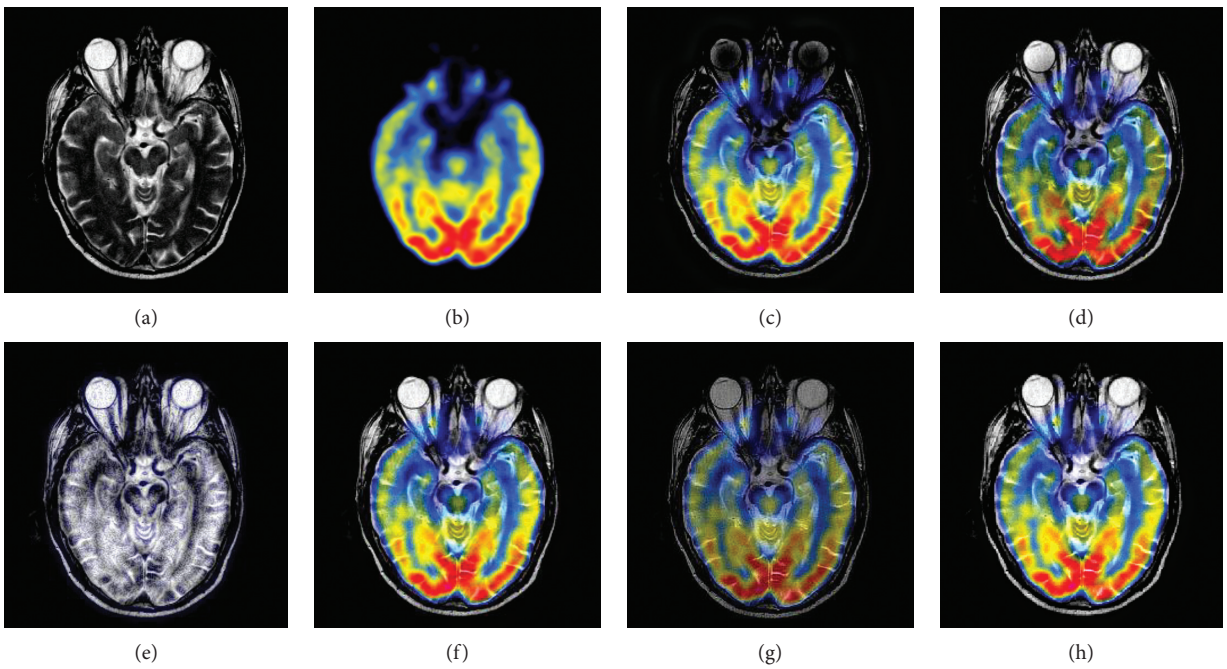

Figure 9: MR and PET medical image fusion results. (a) MR original image. (b) PET original image. (c) NSST-PAPCNN. (d) CSR. (e) MST-SR. (f) NSCT-SR-PCNN. (g) SR-PCNN. (h) Proposed.

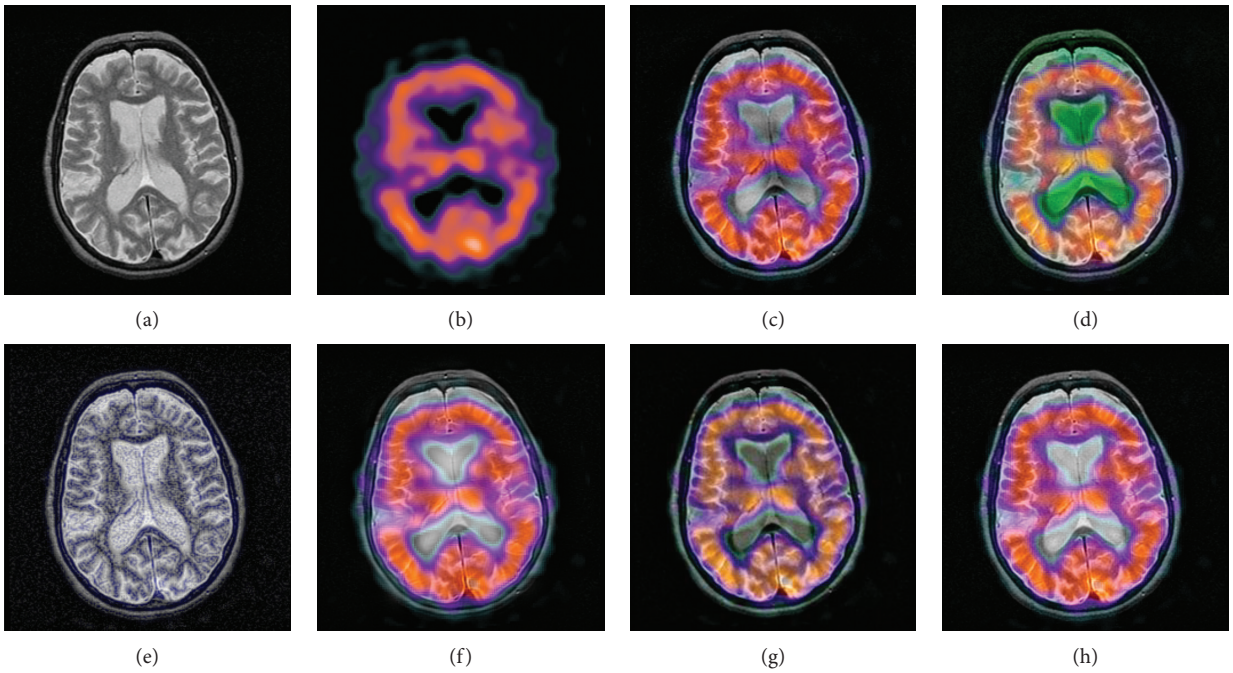

Figure 10: MR and SPECT medical image fusion results. (a) MR original image. (b) SPECT original image. (c) NSST-PAPCNN. (d) CSR. (e) MST-SR. (f) NSCT-SR-PCNN. (g) SR-PCNN. (h) Proposed.

3.2. Comparison with Other Image Fusion Methods. In this section, the proposed method (NSST-PAPCNN-CSR) is compared with other approaches on visual quality and objective assessment.

3.2.1. Source Images from the Whole Brain Atlas of Harvard Medical School. The whole brain Atlas of Harvard Medical School is created by Keith and Johnson from Harvard Medical School. It includes brain samples of normal brain, cerebrovascular disease, brain tumor, degenerative disease, and other brain diseases. The same slice of the same brain is equipped with the registered CT, MR or MR-T1, MR-T2 or PET, and SPECT images. Each pair of source images used in this section are obtained by different imaging methods for the same slice (slice thickness is generally 3 mm or 5 mm) in the same brain at the same angle.

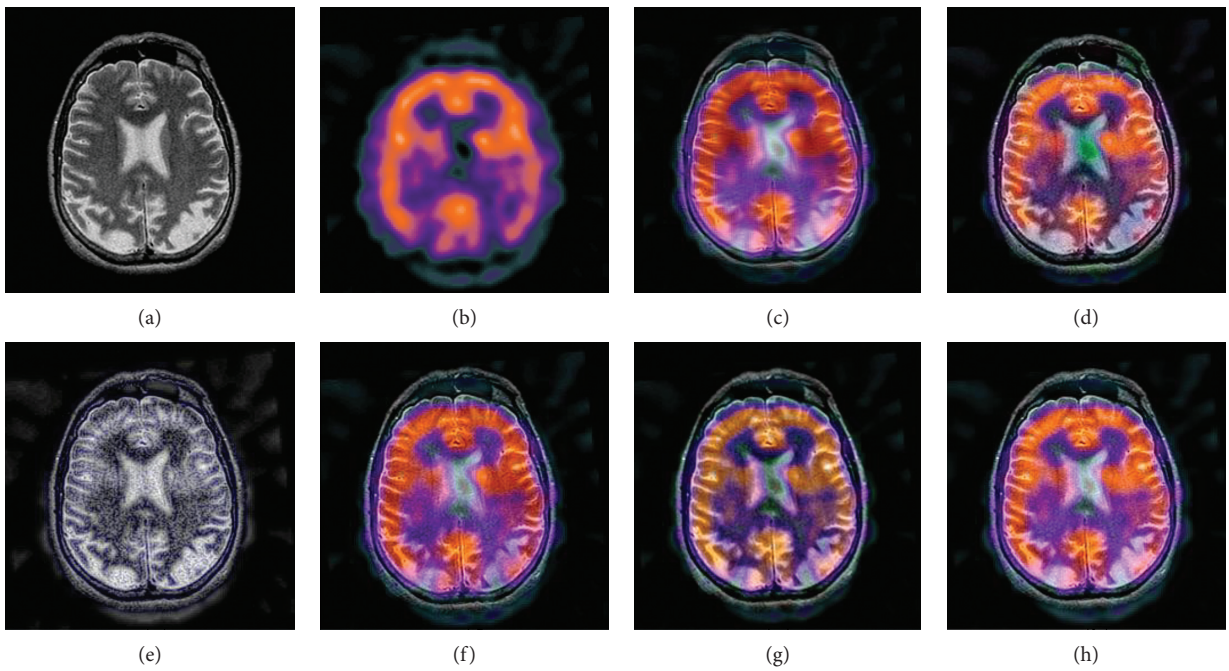

Figure 11: MR and SPECT medical image fusion results. (a) MR original image. (b) SPECT original image. (c) NSST-PAPCNN. (d) CSR. (e) MST-SR. (f) NSCT-SR-PCNN. (g) SR-PCNN. (h) Proposed.

In this experiment, 50 pairs of brain source images in different states were selected for fusion, including 10 pairs of CT/MR images, 10 pairs of MR-T1/MR-T2 images, 15 pairs of MR/PET images, and 15 pairs of MR-SPECT images. We show the fusion results of some of the source images. The fused images are shown in Figures 4–11, and their objective quality evaluation indicators are listed in Table 1.

When the source images come from the whole brain Atlas of Harvard Medical School, the proposed method performs well better than other five contrast methods on both energy preservation, detail extraction, and color preservation, as shown in Figures 4–11. Table 1 lists the objective assessment of different fusion methods on four categories of medical image fusion problems. The average score of each method over all the testing images in each fusion problem is reported. For each index, its maximum value is denoted in bold and italics, and the second biggest value is underlined. In this paper, the RMSE (root-mean-square error) of each index mean of the algorithm is calculated to verify the validity of the data of each index mean of the proposed algorithm. It can be seen from Table 1 that when the source image comes from the whole brain Atlas of Harvard Medical School, the RMSE of each index of the proposed algorithm does not fluctuate more than 1, which has strong data validity. It is known from the objective indices listed in Table 1 that the proposed algorithm had better performance in the MI and SD indices than the other five contrast algorithms. Among them, MI was 8.6% higher and SD 17.5% higher than the average of the five contrast algorithms. NSST-PAPCNN-CSR is not always the best one among the five contrast algorithms in each individual evaluation indicator, but it never ranked less than the top two.

Overall, for the various source images from the whole brain Atlas of Harvard Medical School, the NSST-PAPCNN-CSR algorithm not only achieved better fusion performance visually in edge sharpness, change intensity, and contrast but also performed excellently in objective fusion indicators.

3.2.2. Source Images from the Cancer Imaging Archive (TCIA). The Cancer Imaging Archive (TCIA) is an open-access database of medical images for cancer research. It is usually composed of common diseases (such as lung cancer and brain cancer). The image morphology includes CT, MR, and so on. It also provides image related supporting data, such as the number and date of brain slices. Each pair of source images used in this section are obtained by different imaging methods for the same slice in the same brain at the same angle.

In this experiment, because TCIA has few suitable PET and SPECT images to do fusion experiments, 10 pairs of CT/MR and 10 pairs of MR-T1/MR-T2 brain source images in different states were selected for fusion. We show the fusion results of some of the source images. The fused images are shown in Figures 12–15, and their objective quality evaluation indicators are listed in Table 1.

When the source images come from the Cancer Imaging Archive (TCIA), the proposed method performs well better than other five contrast methods on both energy preservation and detail extraction and color preservation, as shown in Figures 12–15. The objective assessments of different fusion methods on two categories of medical image fusion problems are listed in Table 1. The average score of each method over all the testing images in each fusion problem is reported. In this paper, the RMSE (root-mean-square error) of each index mean of the algorithm is calculated to verify the validity of the data of each index mean of the proposed algorithm. It can be seen

Table 1: Objective assessment of different methods on medical image fusion.

The database	Images	Metrics	NSST-PAPCNN	CSR	MST-SR	NSCT-SR-PCNN	SR-PCNN	Proposed	RMSE (proposed)
The Whole Brain Atlas Of Harvard Medical School	CT/MR	EN	3.1249 (1)	2.9919	2.8641	3.0749	2.7759	3.0767 (2)	0.0262
		$Q^{AB/F}$	0.4587	0.4427	0.4325	0.4801 (2)	0.4408	**0.4839 (1)**	0.0304
		MI	0.8093	0.8079	0.7779	0.8333 (2)	0.7396	**0.8599 (1)**	0.0156
		SF	27.8907	28.4779 (2)	27.6372	27.9712	27.4416	**29.3626 (1)**	0.6256
		AG	6.9390	7.1364 (2)	7.1117	6.9873	6.5669	**7.1671 (1)**	0.0392
		SD	110.4631	110.6766 (2)	109.7036	109.4976	108.0036	**111.0203 (1)**	0.3939
	MR-T1/ MR-T2	EN	3.0751	3.0954	3.1193	3.1564 (2)	2.9382	3.2436 (1)	0.0593
		$Q^{AB/F}$	0.4223	0.4428	**0.5345 (1)**	0.4327	0.4241	0.4926 (2)	0.0587
		MI	1.0879	1.0932	1.1119	1.1247 (2)	1.0830	**1.1675 (1)**	0.1132
		SF	26.8878	**27.8143 (1)**	27.4827	27.3243	22.6816	27.6630 (2)	0.7533
		AG	4.4525	4.9000 (2)	4.8198	4.7360	3.1408	**4.9541 (1)**	0.3882
		SD	109.2559	109.3714	109.2907	109.0063	110.1740 (2)	**111.4005 (1)**	0.2773
	MR/PET	EN	3.2575	3.1860	3.2732 (2)	3.1620	3.1728	3.3962 (1)	0.3524
		$Q^{AB/F}$	0.5213	0.5783	0.6148 (2)	0.5216	0.6125	0.6621 (1)	0.2436
		MI	1.6716 (2)	1.6604	1.6708	1.5385	1.6688	1.7078 (1)	0.3849
		SF	27.0508	29.2171	**31.8184 (1)**	28.1990	29.5717	30.0488 (2)	0.0968
		AG	5.1704	6.3783	6.8126 (2)	5.8611	6.5209	**7.8436 (1)**	0.7054
		SD	112.5116	112.5743 (2)	111.8941	110.2727	111.9179	**114.7089 (1)**	0.8578
	MR/ SPECT	EN	3.5580	3.5357	3.8857 (1)	3.6305	3.4818	3.6897 (2)	0.5361
		$Q^{AB/F}$	0.4561	0.5465	0.7211 (2)	0.5564	0.5521	**0.7426 (1)**	0.0389
		MI	1.3484	1.3491	1.3511	1.3663 (2)	1.3658	**1.4261 (1)**	0.4157
		SF	23.9815	25.2731	**27.7746 (1)**	25.1314	24.6361	25.4938 (2)	0.3981
		AG	4.1747	4.7093	4.7542	4.8058 (2)	4.5293	**4.9342 (1)**	0.6432
		SD	**109.8246 (1)**	108.6124	109.4126	109.3390	108.6478	109.5151 (2)	0.8745
The Cancer Imaging Archive	CT/MR	EN	2.3873	2.5588 (1)	2.4780	2.5250	2.4138	2.5412 (2)	0.0348
		$Q^{AB/F}$	0.2823	0.3242	0.3400 (2)	0.3022	0.3083	**0.3461 (1)**	0.0452
		MI	0.4202	0.4998	0.5359 (2)	0.5328	0.5302	**0.5680 (1)**	0.0799
		SF	23.5399	**27.1924 (1)**	25.3864	24.4104	23.8955	25.5036 (2)	0.5346
		AG	5.5653	5.0692	5.5261	5.6596 (2)	5.5149	**5.6693 (1)**	0.0569
		SD	101.6034	111.2382 (2)	103.4071	102.6671	103.8596	**112.3046 (1)**	0.4832
	MR-T1/ MR-T2	EN	3.0059	3.0495	3.0649 (2)	2.9463	2.9340	3.1736 (1)	0.6203
		$Q^{AB/F}$	0.3183	0.4462	0.4928 (2)	0.4385	0.4061	**0.5103 (1)**	0.1108
		MI	0.8798	1.0100	**1.1441 (1)**	1.0069	0.9576	1.1064 (2)	0.7673
		SF	22.3876	26.9720 (2)	26.0597	26.9641	26.1218	**27.4718 (1)**	0.8564
		AG	3.4087	5.0089 (2)	4.9964	5.0070	5.0174	**5.1650 (1)**	0.1694
		SD	106.2062	108.2755	107.4503	109.2019 (2)	108.0475	**109.3821 (1)**	0.8521

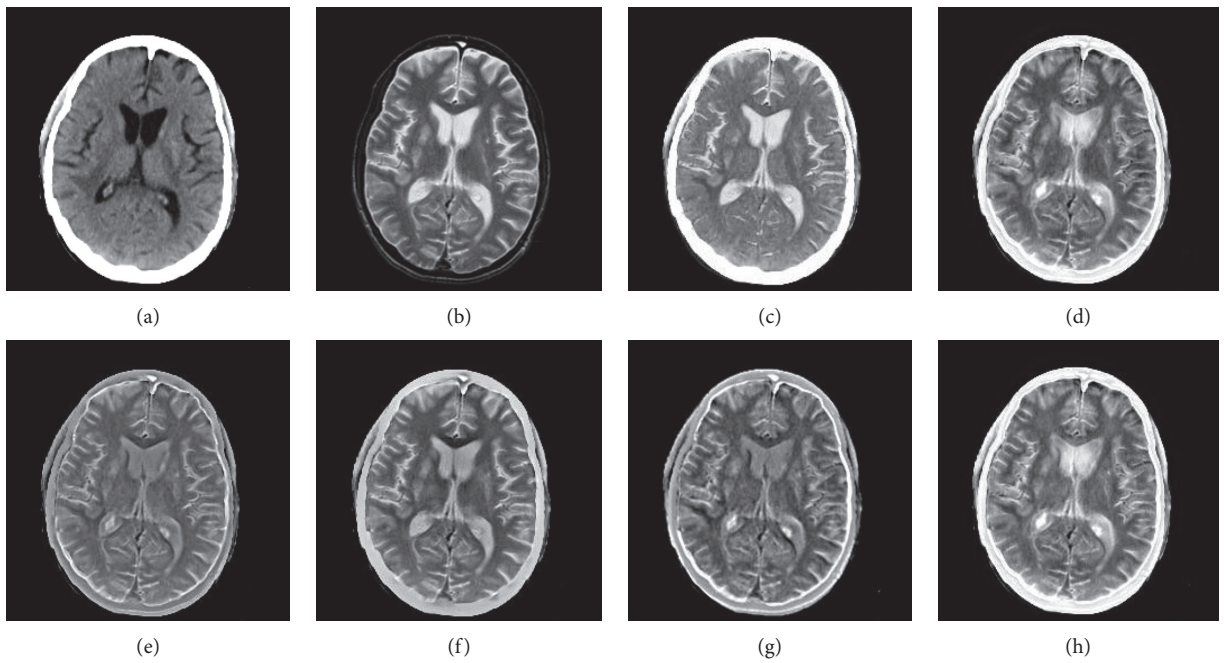

Figure 12: CT and MR medical image fusion results. (a) CT original image. (b) MR original image. (c) NSST-PAPCNN. (d) CSR. (e) MST-SR. (f) NSCT-SR-PCNN. (g) SR-PCNN. (h) Proposed.

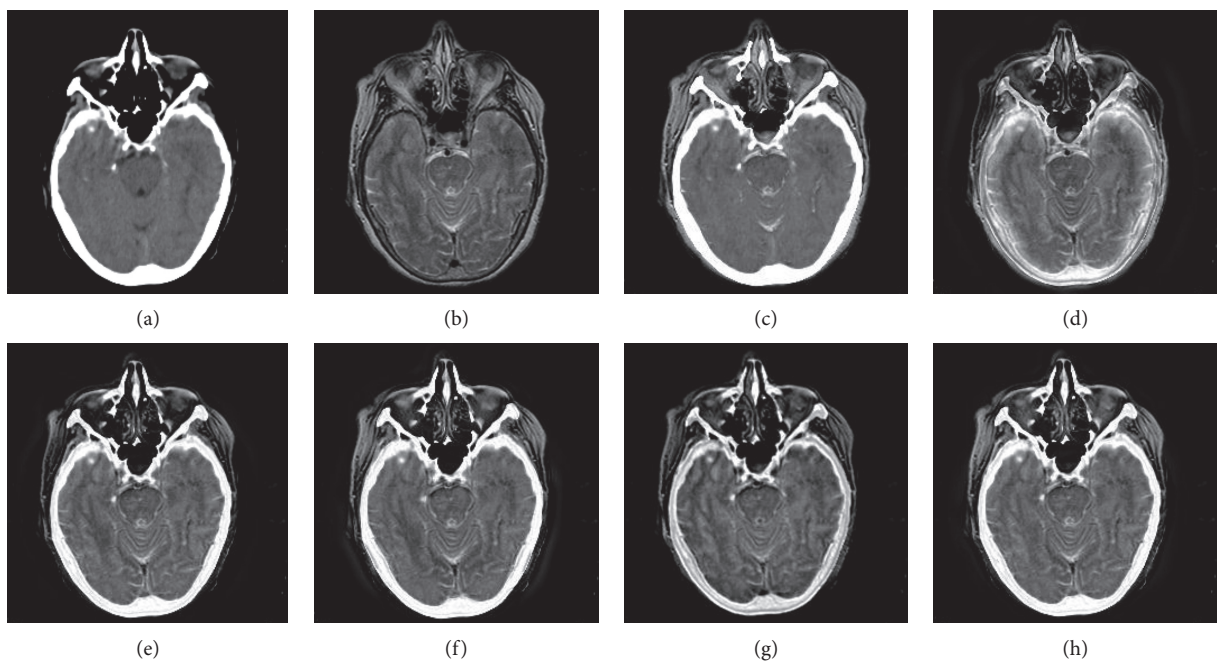

Figure 13: CT and MR medical image fusion results. (a) CT original image. (b) MR original image. (c) NSST-PAPCNN. (d) CSR. (e) MST-SR. (f) NSCT-SR-PCNN. (g) SR-PCNN. (h) Proposed.

from Table 1 that when the source image comes from the Cancer Imaging Archive (TCIA), the RMSE of each index of the proposed algorithm does not fluctuate more than 1, which has strong data validity. It is known from the objective indices listed in Table 1 that the proposed algorithm had better performance in the $Q^{AB/F}$ and AG and SD indices than the other five contrast algorithms. Among them, $Q^{AB/F}$ was 17.9% higher, AG 8.8% higher, and SD 7.7% higher than the average of the five contrast algorithms. NSST-PAPCNN-CSR is not always the best one among the five contrast algorithms in each individual evaluation indicator, but it never ranked less than the top two.

In summary, for the various source images from the Whole Brain Atlas of Harvard Medical School and the

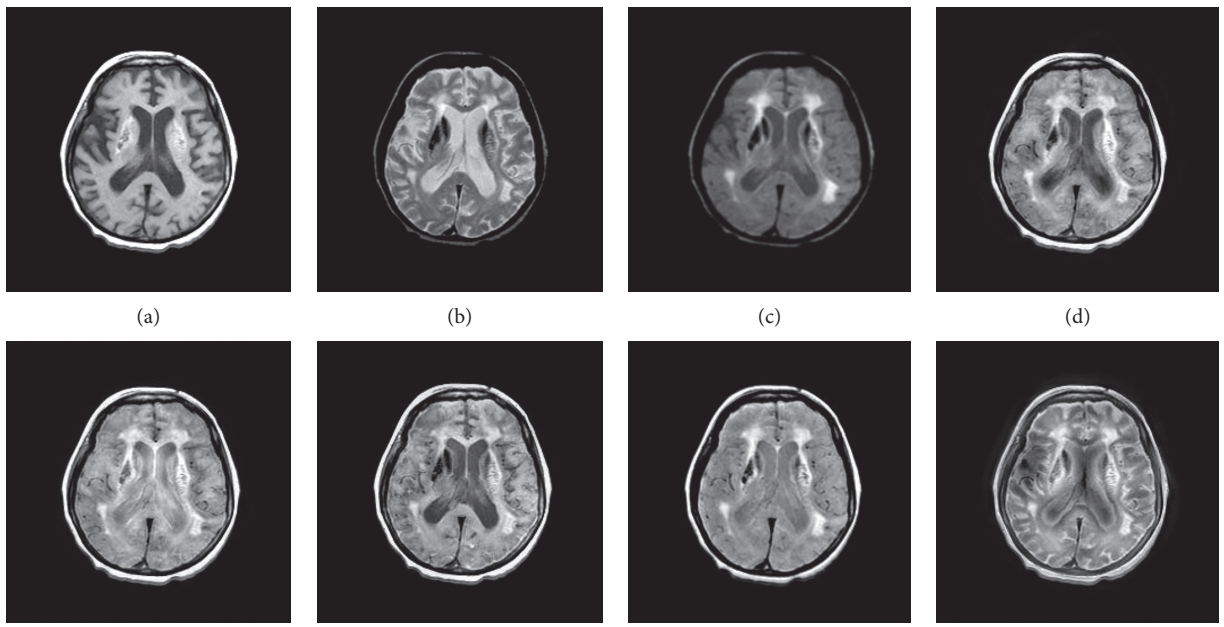

Figure 14: MR-T1 and MR-T2 medical image fusion results. (a) MR-T1 original image. (b) MR-T2 original image. (c) NSST-PAPCNN. (d) CSR. (e) MST-SR. (f) NSCT-SR-PCNN. (g) SR-PCNN. (h) Proposed.

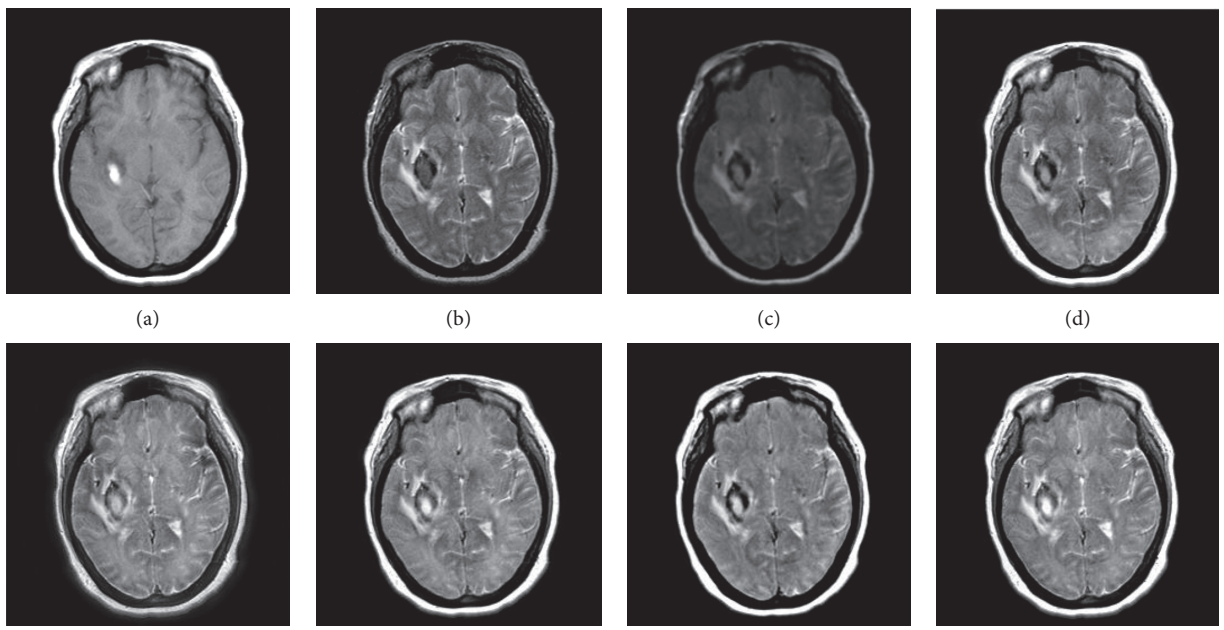

Figure 15: MR-T1 and MR-T2 medical image fusion results. (a) MR-T1 original image. (b) MR-T2 original image. (c) NSST-PAPCNN. (d) CSR. (e) MST-SR. (f) NSCT-SR-PCNN. (g) SR-PCNN. (h) Proposed.

Cancer Imaging Archive (TCIA), the NSST-PAPCNN-CSR algorithm not only achieved good fusion effect visually in terms of edge sharpness, change intensity, and contrast but also performed excellently in objective fusion indicators.

4. Conclusion

A novel NSST domain medical image fusion method was proposed and there were mainly two innovations. First, a

PAPCNN model was introduced into the fusion of high-frequency coefficients. All free parameters in the model were calculated adaptively according to the input high-frequency coefficients; furthermore, the parameter β was adjusted to its optimal value and the synchronous ignition characteristics of the PAPCNN model were coordinated even better. Second, convolutional sparse representation was applied to low-frequency coefficient fusion. It solved two problems existing in sparse representation, namely, limited ability of detail preservation and high sensitivity to mismatch. Thus, it was able to fuse low-frequency coefficients better. 70 pairs of multimodal source images and five kinds of contrast algorithms were used to conduct experiments. The results show that the proposed method has excellent performance in terms of visual perception and objective effect evaluation. The NSST-PAPCNN-CSR algorithm still has potential applications in multifocus image fusion, infrared/visible image fusion, and other image fusion problems.

Data Availability

The data used to support the findings of this study are included within the article.

Conflicts of Interest

The authors declare that they have no conflicts of interest.

References

[1] B. Song, F. Miao, and Q. Zhang, "Research on multi-modal medical image fusion algorithm based on MSVD and MPCNN models," *China Digital Medicine*, vol. 14, no. 2, pp. 9–12, 2007.

[2] S. Singh, D. Gupta, R. S. Anand, and V. Kumar, "Non-subsampled shearlet based CT and MR medical image fusion using biologically inspired spiking neural network," *Biomedical Signal Processing and Control*, vol. 18, pp. 91–101, 2015.

[3] Y. Liu, X. Chen, R. K. Ward, and Z. J. Wang, "Image fusion with convolutional sparse representation," *IEEE Signal Processing Letters*, vol. 23, no. 12, pp. 1882–1886, 2016.

[4] B. Yang and S. Li, "Multi-focus image fusion and restoration with sparse representation," *IEEE Transactions on Instrumentation and Measurement*, vol. 59, no. 4, pp. 884–892, 2010.

[5] Y. Liu and Z. Wang, "Simultaneous image fusion and denoising with adaptive sparse representation," *IET Image Processing*, vol. 9, no. 5, pp. 347–357, 2015.

[6] Y. Chen, S.-K. Park, and D. Ma, "A new automatic parameter setting method of a simplified PCNN for image segmentation," *IEEE Transactions on Neural Networks*, vol. 22, no. 6, pp. 880–892, 2011.

[7] Y. Ming, N. Liu, and Y. Liu, "Medical image fusion with parameter-adaptive pulse coupled neural network in non-subsampled shearlet transform domain," *IEEE Transactions on Instrumentation and Measurement*, vol. 68, no. 1, pp. 49–64, 2019.

[8] G. Easley, D. Labate, and W.-Q. Lim, "Sparse directional image representations using the discrete shearlet transform," *Applied and Computational Harmonic Analysis*, vol. 25, no. 1, pp. 25–46, 2008.

[9] G. Zhou, C. Gao, and C. Guo, "A parametric adaptive simplified PCNN image segmentation method," *Acta Automatica Sinica*, vol. 40, no. 6, pp. 1191–1197, 2014.

[10] M. Chen, M. Xia, and C. Chen, "Infrared and visible image fusion based on sparse representation and NSCT-PCNN," *Electronics Optics & Control*, vol. 25, no. 6, pp. 1–6, 2018.

[11] W. Kong, B. Wang, and Y. Lei, "Technique for infrared and visible image fusion based on non-subsampled shearlet transform and spiking cortical model," *Infrared Physics & Technology*, vol. 71, pp. 87–98, 2015.

[12] B. Wohlberg, "Efficient algorithms for convolutional sparse representations," *IEEE Transactions on Image Processing*, vol. 25, no. 1, pp. 301–315, 2015.

[13] The whole brain atlas of harvard medical School, 2015, http://www.med.harvard.edu/AANLIB/.

[14] The cancer imaging archive (TCIA), https://www.cancerimagingarchive.net/.

[15] B. Wohlberg, "Efficient algorithms for convolutional sparse representations," *IEEE Transactions on Image Processing*, vol. 25, no. 1, pp. 301–315, 2016.

[16] G. Piella and H. Heijmans, *A New Quality Metric for Image Fusion*, in *Proceedings of the IEEE Conference Publications on Image Processing*, pp. 173–176, Santa Barbara, CA, USA, August 2003.

[17] L. Xu, Z. Dai, and F. Li, "Medical image fusion algorithm based on lifting wavelet transform and PCNN," *Journal of Zhejiang Sci-Tech University (Natural Sciences Edition)*, vol. 35, no. 6, pp. 891–898, 2016.

[18] Y. Liu, S. Liu, and Z. Wang, "A general framework for image fusion based on multi-scale transform and sparse representation," *Information Fusion*, vol. 14, 2014.

[19] M. Chen, M. Xia, C. Chen, and G. Zhou, "Medical image fusion based on sparse representation and neural network," *Journal of Henan University of Science and Technology (Natural Science)*, vol. 39, no. 2, pp. 40–47, 2018.

Hindawi
Computational and Mathematical Methods in Medicine
Volume 2019, Article ID 8639825, 11 pages
https://doi.org/10.1155/2019/8639825

Research Article

Unpaired Low-Dose CT Denoising Network Based on Cycle-Consistent Generative Adversarial Network with Prior Image Information

Chao Tang, Jie Li, Linyuan Wang, Ziheng Li, Lingyun Jiang, Ailong Cai, Wenkun Zhang, Ningning Liang, Lei Li, and Bin Yan

PLA Strategy Support Force Information Engineering University, Zhengzhou, Henan Province 450001, China

Correspondence should be addressed to Bin Yan; ybspace@hotmail.com

Received 1 July 2019; Revised 2 September 2019; Accepted 16 September 2019; Published 7 December 2019

Guest Editor: Adam Konefal

The widespread application of X-ray computed tomography (CT) in clinical diagnosis has led to increasing public concern regarding excessive radiation dose administered to patients. However, reducing the radiation dose will inevitably cause server noise and affect radiologists' judgment and confidence. Hence, progressive low-dose CT (LDCT) image reconstruction methods must be developed to improve image quality. Over the past two years, deep learning-based approaches have shown impressive performance in noise reduction for LDCT images. Most existing deep learning-based approaches usually require the paired training dataset which the LDCT images correspond to the normal-dose CT (NDCT) images one-to-one, but the acquisition of well-paired datasets requires multiple scans, resulting the increase of radiation dose. Therefore, well-paired datasets are not readily available. To resolve this problem, this paper proposes an unpaired LDCT image denoising network based on cycle generative adversarial networks (CycleGAN) with prior image information which does not require a one-to-one training dataset. In this method, cyclic loss, an important trick in unpaired image-to-image translation, promises to map the distribution from LDCT to NDCT by using unpaired training data. Furthermore, to guarantee the accurate correspondence of the image content between the output and NDCT, the prior information obtained from the result preprocessed using the LDCT image is integrated into the network to supervise the generation of content. Given the map of distribution through the cyclic loss and the supervision of content through the prior image loss, our proposed method can not only reduce the image noise but also retain critical information. Real-data experiments were carried out to test the performance of the proposed method. The peak signal-to-noise ratio (PSNR) improves by more than 3 dB, and the structural similarity (SSIM) increases when compared with the original CycleGAN without prior information. The real LDCT data experiment demonstrates the superiority of the proposed method according to both visual inspection and quantitative evaluation.

1. Introduction

X-ray computed tomography (CT) is one of the most significant imaging modalities in modern hospitals and clinics. However, the risk of radiation in CT induces genetic, cancerous, and other diseases and has become a critical concern to patients and operators [1–3]]. A common and effective strategy to alleviate the risk is to achieve low-dose CT (LDCT) imaging by reducing the tube current during scanning and consequently decreasing the number of photons received by the detector. The dose reduction increases noise and artifacts in reconstructed CT images, thereby severely degrading the image quality and jeopardizing the clinical diagnosis. To solve this problem, researchers have proposed various noise-reduction strategies, including iterative reconstruction (IR) [4, 5], sinogram domain denoising [6–9], and image domain postprocessing [10–12].

Over the past decades, researchers have focused on developing new iterative algorithms for LDCT image reconstruction. In general, these algorithms optimize an objective function, which incorporates a system model [13, 14],

a statistical noise model, and prior information in the image domain [4, 15, 16]. Well-known image priors consist of total variation (TV) and its variants [17–19], dictionary learning [20, 21], and wavelet frame [22]. These iterative reconstruction algorithms exhibit satisfactory performance in improving image quality, but their computational burden and sensitive parameters limit their practical applications.

Image postprocessing is more computationally efficient compared with iterative reconstruction, which has spawned a lot of simple and effective methods. Nonlocal means (NLM) filtering methods estimate noise components by using multiple patches extracted at different locations in the image [23] and have been widely used for CT [24]. Motivated by compressed sensing methods, an adaptive K-SVD method [25] was proposed to reduce artifacts in CT reconstructions. The block matching 3D (BM3D) method is also an outstanding method for image postprocessing in CT imaging fields [26, 27]; this method exploits similarities in image blocks. These traditional postprocessing methods have improved the quality of CT images; however, the results often undergo edge blurring and/or residual artifacts given the nonuniform distribution of reconstruction noise.

More recently, several supervised machine learning approaches have been proposed for noise reduction in LDCT. These methods usually reveal a relation between the pixel value in the LDCT image and the pixel value at the same location in a corresponding NDCT image by training with paired images. Chen et al. [28] designed a deep convolutional neural network (CNN) to map LDCT images toward its relative normal-dose counterparts in a patch-by-patch manner. Kang et al. [29] used a similar method but adopted CNN to directional wavelet transform of CT images. Then, more complex networks were proposed to handle the LDCT denoising problem such as the residual encoder-decoder convolutional neural network (RED-CNN) in [30], which achieves competitive performance relative to state-of-the-art methods in clinical cases.

Although the abovementioned networks presented impressive denoising results, they all belong to the end-to-end network, which typically utilizes mean squared errors (MSE) between the network output and the ground truth as loss function. However, recent studies [31, 32] indicated that this per-pixel MSE often suffers from oversmoothed edges and loss of details. MSE-based approaches tend to take the mean of high-resolution patches by using Euclidean distance rather than geodesic distance. Given that the medical images usually lie in a highly nonlinear manifold [33], the algorithm is prone to neglect subtle details that are vital for clinical diagnosis when it tries to minimize per-pixel MSE. To overcome the limitations of per-pixel regression in noise reduction, the generative adversarial network (GAN) [34] based on adversarial loss is introduced to medical image reconstruction. In 2017, Wolterink et al. [35] were the first to apply the GAN for cardiac CT image reconstruction. And, Yang et al. [36] utilized a GAN with Wasserstein distance (WGAN). In order to enhance the capability of noise reduction, perceptual loss is simultaneously used to optimize the loss function. Yi and Babyn [37] combined an adversarial trained network and a sharpness detection network to mitigate noise in LDCT and achieved satisfactory performance. Hence, a general framework for estimating generative models by using an adversarial process has shown outstanding performance in medical image reconstruction.

The above-mentioned denoising networks usually require spatially paired counterparts. However, in medical imaging, well-paired counterparts are difficult to obtain. For example, in LDCT imaging, continuously scanning a patient twice in normal and low dose is impossible under normal circumstances. The shortage of paired data has been one of the factors that restrict the wide application of deep learning in low-dose CT reconstruction. Recently, unsupervised variants of GANs, such as CycleGAN [38] and DualGAN [39], have been proposed for mapping different domains without matching data pairs. Motivated by their success in image processing, unpaired GANs have been successfully applied to CS-MRI reconstruction [40] and CT synthesis based on MR images [41, 42]. For LDCT reconstruction, well-paired clinical scans acquired at different dose levels are not readily available. Even if we obtain the same patient data at different dose levels, the data are difficult to match perfectly due to physical activity and the inevitable slight movement of the scanning position, which may affect the denoising ability of the networks.

In this study, we propose an unpaired LDCT denoising network based on CycleGAN with prior image information. In the proposed network, the design of cycle-consistent structure impels the network to learn the mapping relationship between the LDCT image collection and NDCT image collection (Figure 1(a)), rather than an image pair of an LDCT image and NDCT image (Figure 1(b)). Therefore, the proposed network does not need a one-to-one corresponding training dataset and can learn with the unpaired dataset. Meanwhile, the prior image information extracted from the preprocessed image by using LDCT is introduced into the network to supervise the generation of content and ensure correspondence of the image content. The map of image collections through cyclic loss and the supervision of content through prior image loss confer our proposed method to produce results that have not only lower noise but also accurate details.

2. Methods

2.1. Noise Reduction Model. In LDCT imaging, serious noise typically occurs in CT images as the number of photons received by the detector decreases. One of the effective ways to improve the image quality is designing a tailored network to make the input LDCT images as close as possible to the NDCT images. This process can be classified as an image denoising problem, which can be described by the following model:

$$G : x \longrightarrow y, \tag{1}$$

where $x \in R^{N\times N}$ denotes an LDCT image and $y \in R^{N\times N}$ denotes the corresponding NDCT image. The goal of the noise reduction process is to obtain a transformation G that maps x to y.

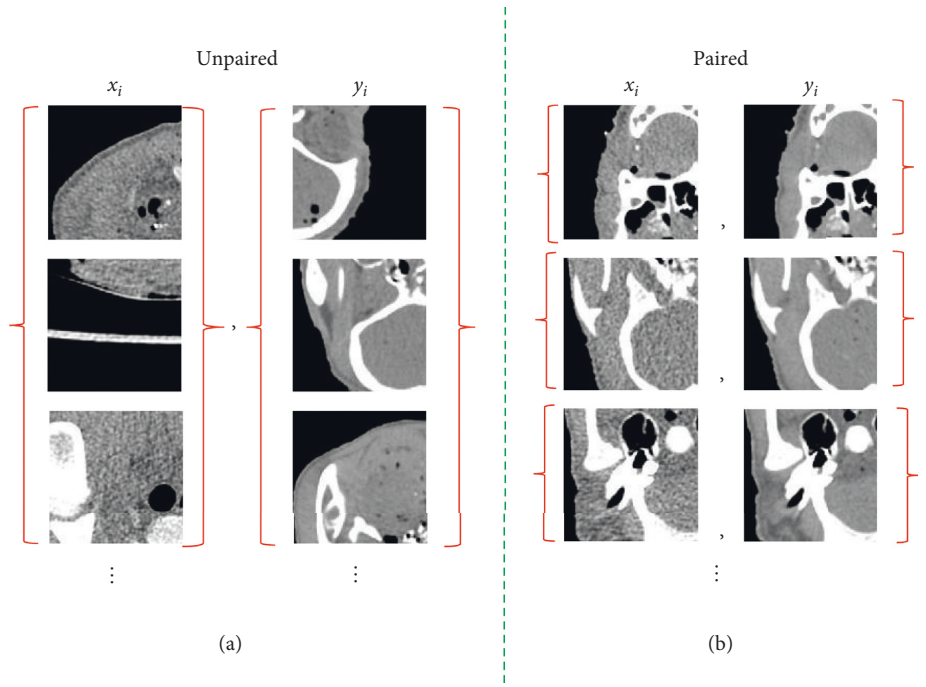

Figure 1: Schematic diagram of (a) unpaired dataset and (b) paired dataset.

In this process, x can be seen as a sample from the LDCT distribution P_l and y can be seen as a sample from the NDCT distribution P_n. The denoising process transforms x to a certain distribution P_g. And, the denoising process aims to determine an optimal G to make P_g close to P_n. However, in the reconstructed LDCT images, noise is complicated and uniformly distributed over the whole image; as such, distributions P_l and P_n have no explicit mathematical relationship up to date [36]. The traditional methods usually have difficulty in denoising LDCT images. For deep learning-based methods, the uncertainty of a noise model can be ignored due to the learning capability of high-level features and presentation of data distribution by the CNN. Therefore, designing a tailored CNN is an effective method to suppress noise in LDCT and improve image quality.

2.2. Introduction of CycleGAN. In 2017, Zhu et al. [38] proposed an unpaired network named CycleGAN, which has gained extensive attention. This network can capture the special characteristics of one image collection and figure out how these characteristics could be translated into other image collection without using any paired training examples; this network has been successfully utilized in style transfer, object transfiguration, season transfer, and photo enhancement.

Under the assumption that there is some underlying relationship between the source domain X and target domain Y, the goal of CycleGAN is to learn mapping $G : X \longrightarrow Y$ so that the distribution of image from $G(x)$ is indistinguishable from the distribution of image from domain Y. This network includes two mapping functions, namely, $G : X \longrightarrow Y$ and $F : Y \longrightarrow X$ and also introduces two discriminators, namely, D_X and D_Y. Discriminator D_Y aims to distinguish between translated samples $G(x)$ and real samples y. Discriminator D_X aims to distinguish between translated samples $F(y)$ and real samples x. In theory, adversarial training can identify mappings G and F that produce outputs identically distributed as target domains Y and X [34]. However, with its large sufficient capacity, a network can map the same set of input images to any random permutation of images in the target domain, where any of the learned mappings can induce an output distribution that matches the target distribution. Therefore, adversarial loss alone cannot guarantee that the learned function can map individual input x to desired y. To further reduce the space of possible mapping functions, the mapping functions G and F should be cycle consistent. As shown in Figure 2(a), for each image x from domain X, the image translation cycle should be able to bring x back to the original image: $x \longrightarrow G(x) \longrightarrow F(G(x)) \approx x$, which is named as forward cycle consistency. Similarly, as demonstrated in Figure 2(b), for each image y from domain Y, the image translation cycle should be able to bring y back to the original image: $y \longrightarrow F(y) \longrightarrow G(F(y)) \approx y$, which is named as backward cycle consistency. The abovementioned behavior can be incentivized by cycle-consistency loss.

$$L_{\text{cyc}}(G, F) = \mathbb{E}_{x \sim P_{\text{data}}(x)}\left[\|F(G(x)) - x\|_1\right] + \mathbb{E}_{y \sim P_{\text{data}}(y)}\left[\|G(F(y)) - y\|_1\right], \tag{2}$$

where $P_{\text{data}(x)}$ is the distribution of x and $P_{\text{data}}(y)$ is the distribution of y.

In LDCT imaging, although the projection data contain a lot of noise, it is usually complete. Therefore, the reconstructed images still contain useful information that is basically consistent with corresponding NDCT images. This indicates that there is a close relationship between the LDCT

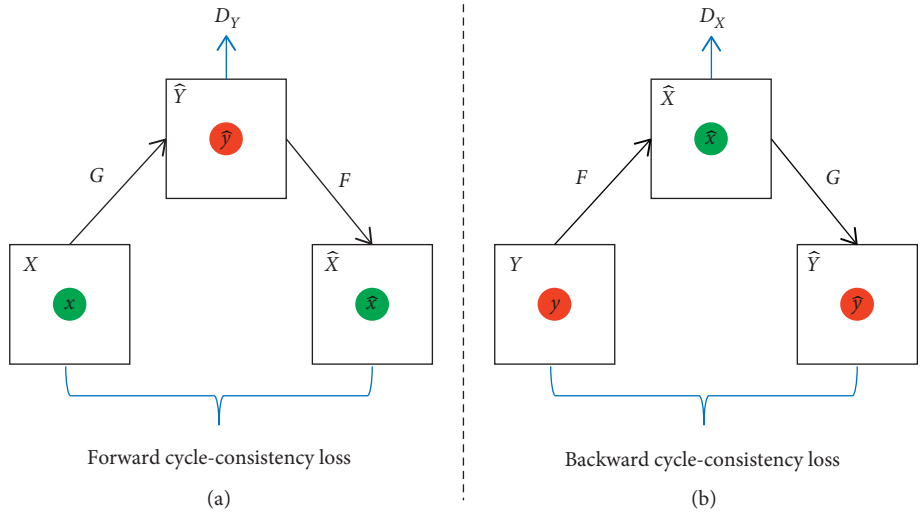

Figure 2: Structure diagram of CycleGAN. (a) Forward cycle-consistency loss. (b) Backward cycle-consistency loss.

image and NDCT image and satisfies the basic assumption of CycleGAN. Thus, this study considers using this unpaired network for LDCT image reconstruction.

Based on its structure, CycleGAN mainly focuses on the map of distributions. This network is better at the overall conversion of images and may overlook the correspondence of details. However, for LDCT noise reduction, the outputs should not only appear similar to an NDCT image but also retain details as much as possible; more importantly, the output must not contain false information, which may cause misdiagnosis. These issues require additional supervision and restraint to the network in the training process to make it more suitable for LDCT reconstruction. In this study, we consider incorporating prior image information into the network to guarantee content correspondence and prevent the generation of fake details during denoising process.

2.3. Unpaired Denoising Network Based on CycleGAN with Prior Information. Figure 3 shows an overview of our proposed method. The network contains forward and backward cycles and two generators and discriminators. In order to more clearly illustrate the training mechanism of the proposed network, we randomly selected an LDCT image from LDCT image collection and an NDCT image from the NDCT image collection as the input-ground truth pair. Note that the LDCT image is not corresponding to the NDCT image, as shown in Figure 4.

In the forward cycle, generator G_N is trained to generate images that are as close to corresponding NDCT images as possible (Figure 3(a)). Generator F_L is trained to translate the resulting image $G_N(x)$ back to the corresponding LDCT image. In the backward cycle, generator F_L is trained to generate images that are as close to corresponding LDCT images as possible (Figure 3(b)). Generator G_N is trained to translate the resulting image $F_L(y)$ back to the NDCT image. In the training process of network, the discriminators D_N and D_L are used to estimate the probability that the sample is from the real image rather than generating image. At the same time, the generators G_N and F_L attempt to generate images that are not easily distinguishable by the discriminators. This paper utilizes the adversarial loss [43] as the objective function to train the "game" process:

$$\begin{aligned} L_{\mathrm{GAN}_N}(G_N, D_N, X, Y) &= \mathbb{E}_{y\sim p_{\mathrm{data}}(y)}[\log D_N(y)] \\ &\quad + \mathbb{E}_{x\sim p_{\mathrm{data}}(x)}[\log(1 - D_N(G_N(x)))], \\ L_{\mathrm{GAN}_L}(F_L, D_L, X, Y) &= \mathbb{E}_{x\sim p_{\mathrm{data}}(x)}[\log D_L(x)] \\ &\quad + \mathbb{E}_{y\sim p_{\mathrm{data}}(y)}[\log(1 - D_L(F_L(y)))]. \end{aligned} \tag{3}$$

In order to reduce the feasible domain space of the mapping functions, the cycle consistency is introduced to further constrain the training process of the network so that the network can be trained under unpaired data:

$$\begin{aligned} L_{\mathrm{cyc}}(G_N, F_L) &= \mathbb{E}_{x\sim P_{\mathrm{data}}(x)}\left[\left\|F_L(G_N(x)) - x\right\|_1\right] \\ &\quad + \mathbb{E}_{y\sim P_{\mathrm{data}}(y)}\left[\left\|G_N(F_L(y)) - y\right\|_1\right]. \end{aligned} \tag{4}$$

For this cycle consistency network, the performance of a generator requires the indirect supervision through the results of another generator. For example, in the forward cycle, in addition to discriminator D_N, the performance of generator G_N also needs to be supervised by the results $F_L(G_N(x))$ of another generator F_L. This mechanism does not guarantee the accuracy of the final input and may lead to the occurrence of fake details. For LDCT image reconstruction, the accuracy of the results is critical, and if false information is generated, it may cause misdiagnosis, leading to serious consequences. These circumstances require direct constraints to the generators, especially to generator G_N, which directly produces the desired outcome. Therefore, this paper incorporates the prior image information into the network to directly supervise the generator G_N, as shown in Figure 3(a). For fear of changing the unpaired property of the network, the resulting images

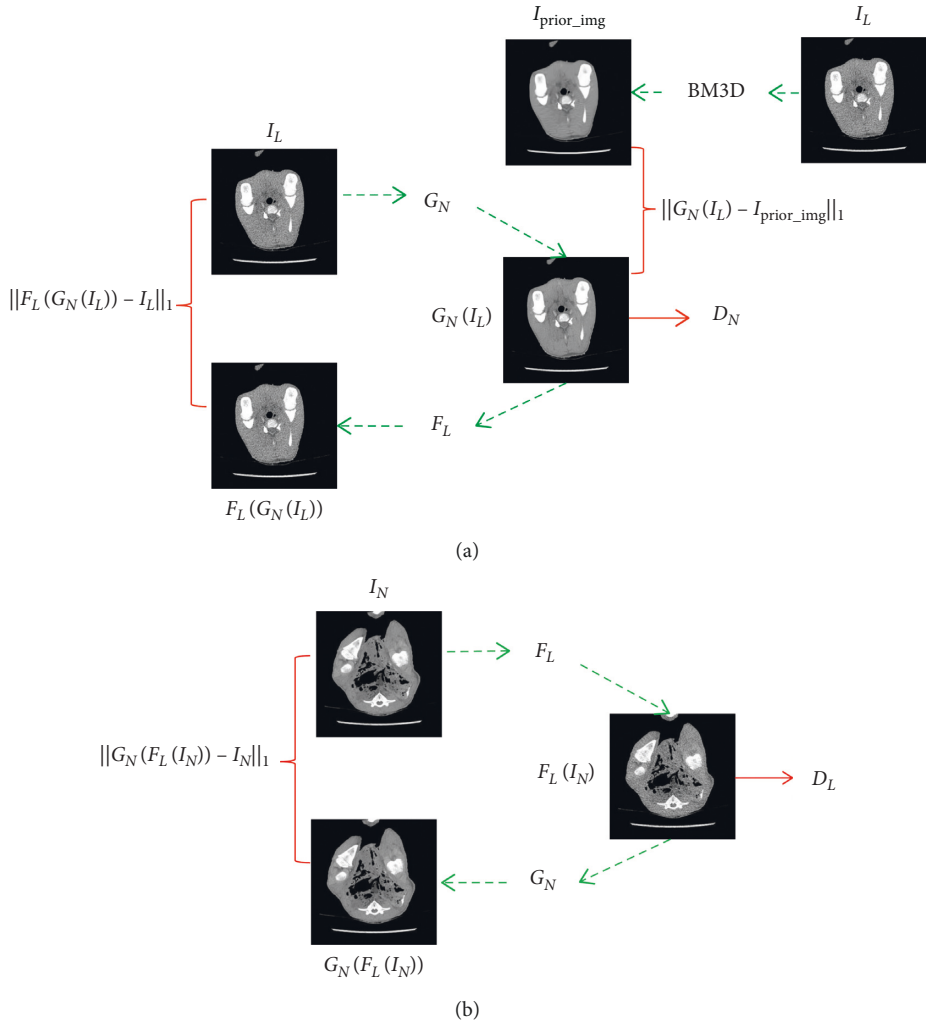

Figure 3: Overview of the proposed method. (a) Forward cycle. (b) Backward cycle.

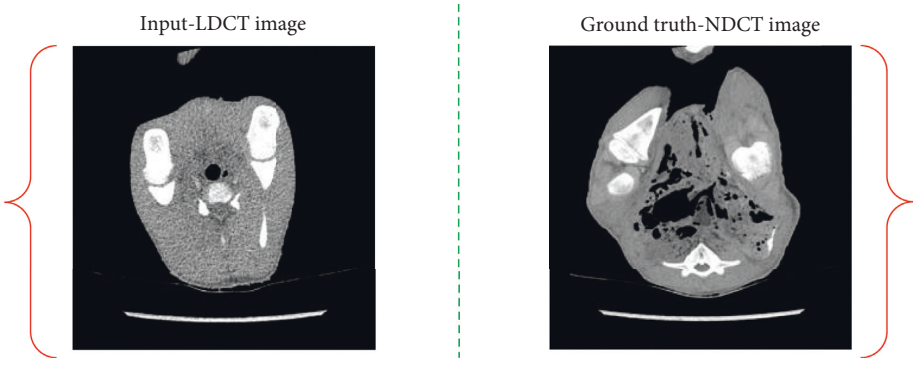

Figure 4: One input-ground truth pair of the proposed unpaired network.

processed by BM3D method utilizing LDCT images are regarded as prior images. And, the mean absolute error (MAE) between the prior image and the generated image is introduced into the loss function to constrain the training of the network. The adversarial loss of the forward cycle can be written as

$$L^{p}_{\mathrm{GAN}_N}(G_N, D_N, X, Y) = \mathbb{E}_{y\sim p_{\mathrm{data}}(y)}[\log D_N(y)] + \mathbb{E}_{x\sim p_{\mathrm{data}}(x)}\left[\log(1 - D_N(x)) + \alpha\left\|G_N(x) - I_{\mathrm{prior\_img}}\right\|_1\right], \quad (5)$$

where α is the weight of the MAE. In the training process, the generator G_N tries to minimize the objective function (5) while the discriminator D_N tries to maximize it, that is, $\min_{G_N} \max_{D_N} L^p_{\mathrm{GAN}_N}(G_N, D_N, X, Y)$. We denote the proposed network as CycleGAN-BM3D.

Through the above analysis, the total loss function of our proposed method is

$$\begin{aligned} L(G_N, F_L, D_N, D_L) = {} & L^p_{\mathrm{GAN}_N}(G_N, D_N, X, Y) \\ & + L_{\mathrm{GAN}_L}(F_L, D_L, Y, X) \\ & + \lambda L_{\mathrm{cyc}}(G, F), \end{aligned} \tag{6}$$

where λ is a nonnegative parameter used to balance the weight of the cycle consistency loss. The total objective function of the proposed CycleGAN-BM3D is

$$G_N^*, F_L^* = \arg \min_{G_N, F_L} \max_{D_N, D_L} L(G_N, F_L, D_N, D_L). \tag{7}$$

2.4. Network Architecture. In the proposed method, the network of the generator, as shown in Figure 5(a), includes three submodules: encoder, convertor, and decoder. The encoder extracts the features from the input image utilizing CNN. The network of the encoder includes one 7×7 Convolution-InstanceNorm-ReLU layer with 64 filters and stride 1 denoted as c7s1-64, two 3×3 Convolution-InstanceNorm-ReLU layers with k filters and stride 2 in which k equals to 128 and 256, respectively. We denote these two layers as d128 and d256. The convertor, as shown in Figure 5(b), is used to convert feature vectors extracted from the source domain X to the target domain Y. The convertor contains six residual network (Resnet) blocks [44], and each block contains two 3×3 convolutional layers with 256 filters on both layers. The decoder includes three layers. The first two layers are 3×3 fractional-strided-Convolution-InstanceNorm-ReLU layers with stride 1/2 and 64 and 32 filters, respectively. We denote the two layers as u64 and u32. The third layer is a 7×7 Convolution-InstanceNorm-ReLU with 3 filters and stride 1 denoted as c7s1-3. The network of the discriminator, as shown in Figure 5(c), consists of five convolution layers. The first four layers are 4×4 Convolution-InstanceNorm-LeakyReLU layers with stride 2 and 64, 128, 256, and 512 filters, respectively. We denote them as C64, C128, C256, and C512. We use leaky ReLUs with slope 0.2. In the last layer, a 4×4 convolution layer with 1 filter and stride 1 is utilized to produce a one-dimensional output.

3. Experiments and Results

3.1. Experimental Dataset and Performance Evaluations. The CT images of a deceased piglet were selected as the experimental dataset to verify the performance of the proposed network. The images were scanned by a 64-slice multidetector GE Healthcare scanner (Discovery CT750 HD) by using 100 kV and 0.625 mm slice thickness. Five different tube currents were set to yield CT images with different dose levels. The specific scanned parameters and effective dose of different tube currents are listed in Table 1.

In each dose level, 906 images with size 512×512 were acquired. As shown in Figure 6, we partitioned the slices by taking one's data and then skipping 10 slices. We finally obtained 360 images reconstructed by FBP using the projection data of 5% dose as the noisy dataset, that is, source collection X. And, 180 images were obtained for testing. The normal dose dataset utilized consists of 360 images, which are corresponding to the noisy dataset and obtained from the NDCT images constructed by FBP. The normal dose dataset is the target collection Y. Given the unpaired property of the proposed network, the training images and the ground truth do not require a one-to-one correspondence. The number of two image datasets can also be different. In the training stage, we performed an unpaired operation for the inputs and labels of the network. In addition, each image was divided into sixteen 128×128 images to enlarge the training dataset to 5760 images.

For comparison, we selected some representative traditional methods and other networks.

3.1.1. BM3D. This method exhibits outstanding performance in noise reduction over other traditional image denoising methods.

3.1.2. Original CycleGAN. This network is trained without the constraint of prior image to test the supervised effect of the prior image. The input dataset and ground truth dataset are the same as the proposed method CyclGAN-BM3D, which are not one-to-one correspondence.

Structural similarity (SSIM) [45], peak signal-to-noise ratio (PSNR), and normalized mean absolute distance (NMAD) are selected as measures of reconstruction quality for the quantitative assessment of the proposed network and abovementioned contrast algorithms. Specifically, PSNR and NMAD are defined as follows:

$$\begin{aligned} \mathrm{PSNR} &= 10 \log_{10} \left(\frac{\mathrm{MAX}^2(f)}{1/N \sum_{i=1}^{N} \left| f(i) - f_0(i) \right|^2} \right), \\ \mathrm{NMAD} &= \frac{\sum_{i=1}^{N} \left| f(i) - f_0(i) \right|}{\sum_{i=1}^{N} |f(i)|}, \end{aligned} \tag{8}$$

where f and f_0 represent the denoising image and ideal image, respectively, i is the pixel in the image, and N is the total number of pixels in the image. A higher PSNR indicates that the image is of higher quality. The NMAD value close to 0 indicates small differences between the ideal image and the reconstructed results. In general, $\mathrm{SSIM} \leq 1$ and $\mathrm{SSIM} = 1$ indicate the exact theoretical reconstruction.

3.2. Implementation Details. In the training process, the negative log likelihood objective of the first two items in L_{GAN_N} and L_{GAN_L} is replaced by least squares loss to stabilize the proposed model [46]. After the replacement, we train G_N to minimize

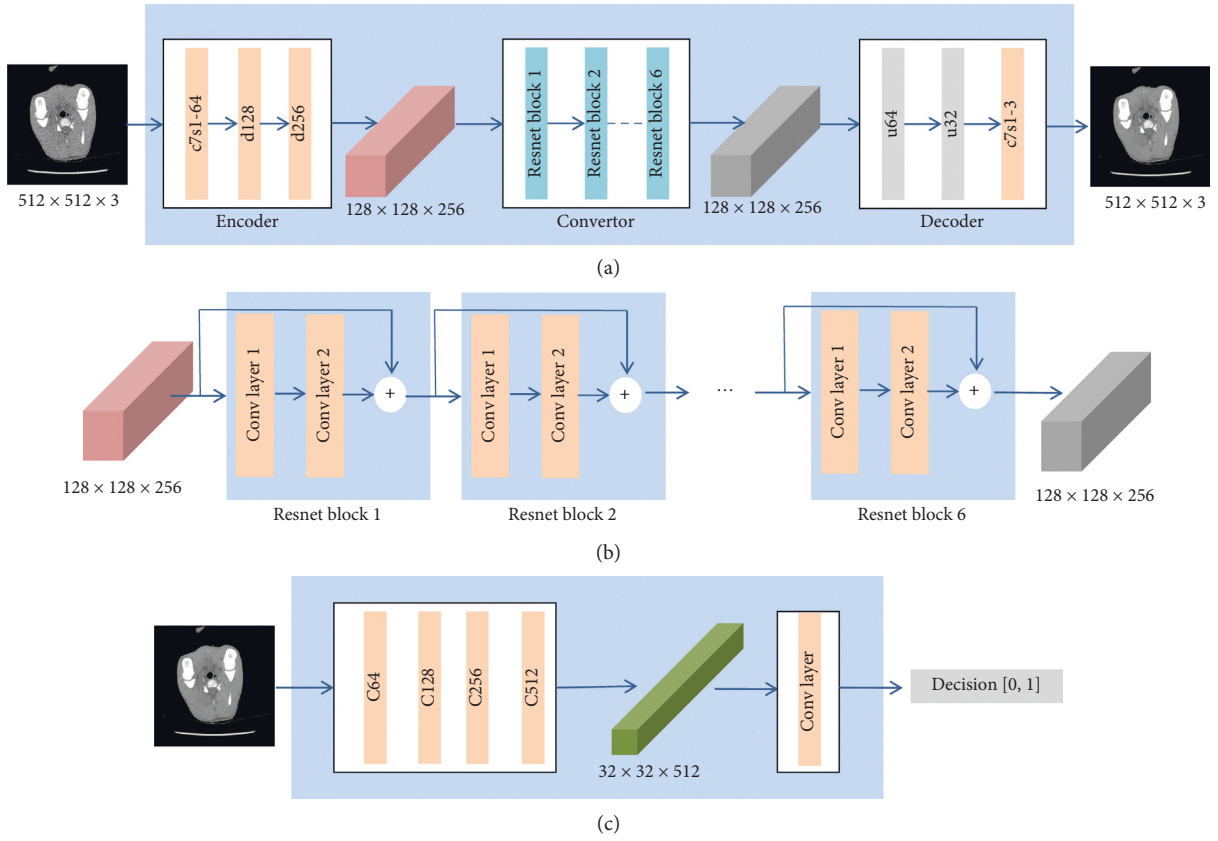

Figure 5: Network structure. (a) Diagram of generator's network structure. (b) Diagram of convertor's network structure. (c) Diagram of discriminator's network structure.

Table 1: CT scanning protocol for the experiment.

	Normal dose	50% dose	25% dose	10% dose	5% dose
Tube current (mAs)	300	150	75	30	15
Effective dose (mSv)	14.14	7.07	3.54	1.41	0.71

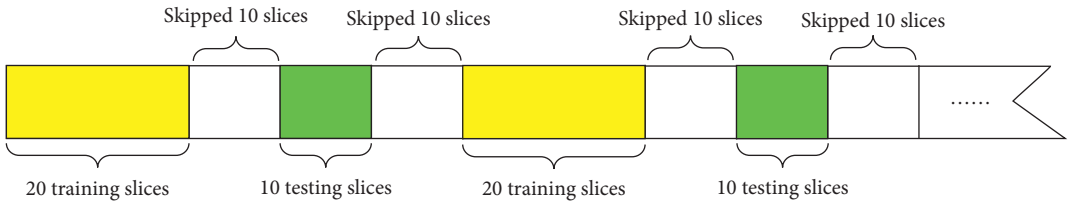

Figure 6: Schematic diagram of data preparation. The yellow rectangular blocks represent the training data, the green rectangular blocks represent the test data, and the white rectangular blocks represent the skipped slices.

$$\mathbb{E}_{x\sim p_{\text{data}}(x)}\left[\left(D_N\left(G_N(x)\right)-1\right)^2+\alpha\left\|G_N(x)-I_{\text{prior\_img}}\right\|_1\right]. \tag{9}$$

We also train F_L to minimize

$$\min \mathbb{E}_{y\sim p_{\text{data}}(y)}\left[\left(D_L\left(F_L(y)\right)-1\right)^2\right]. \tag{10}$$

For discriminators D_N and D_L, the objectives are

$$\begin{aligned}&\min \mathbb{E}_{y\sim p_{\text{data}}(y)}\left[\left(D_N(y)-1\right)^2\right]+\mathbb{E}_{x\sim p_{\text{data}}(x)}\left[D_N\left(G(x)^2\right)\right],\\&\min \mathbb{E}_{x\sim p_{\text{data}}(x)}\left[\left(D_L(x)-1\right)^2\right]+\mathbb{E}_{y\sim p_{\text{data}}(y)}\left[D_L\left(F_L(y)^2\right)\right].\end{aligned} \tag{11}$$

For the setting of parameters, λ is set as 10. Adam solver with a batch size of 1 is selected as the optimizer to optimize the networks. We keep the same learning rate for the first

10,000 epochs and linearly decay the rate to zero over the next 10,000 epochs. The proposed network in this paper trained 40,000 epochs. α is an important parameter for controlling the weight of prior information during training. When the value of α is too small, the effect of prior information will be negligible and cause minimal improvement in image quality. By contrast, a very large α will overemphasize the role of prior information and, to some extent, limit the learning ability of the network itself. In this paper, a series of networks was trained by setting different values of α to determine a suitable value. For the sake of fairness, each network has the same parameters' setting, except α. We randomly selected 10 LDCT images to test the performance of different networks. The effect of α was quantitatively determined by plotting the average SSIM and NMAD of the denoising images in Figure 7.

From the curves of Figure 7, when $\alpha = 10$, the SSIM reaches the maximum, indicating that the denoising images are most similar to the NDCT images in structure, that is, under this circumstance, the network has the greatest ability to retain the details of the LDCT images. NMAD reflects the accuracy of denoising to some extent. Smaller NMAD indicates that the noise in the LDCT images is removed more completely. Considering the detail retention and noise reduction of the network, this paper set α as 10.

To analyze the potential denoising capability of selected algorithms and networks, two representative slices and the corresponding zoomed regions of interest (ROIs) are shown in Figures 8–10, respectively.

As shown in Figure 8, when using traditional methods (BM3D) or deep learning-based methods, the noise that appears in the LDCT image is suppressed to varying degrees. The classic BM3D method has an outstanding noise suppression effect but makes the processed image oversmoothed so that some vital details disappear. As indicated by the red arrows in ROI, the results of BM3D lose some information of the bone. Although the result of the original CycleGAN is not oversmoothed, it shows fake details, connecting the unconnected bones in the NDCT image. The CycleGAN-BM3D, which introduces prior image information, does not have redundant details and retains the information that should be retained.

Figure 9 shows the overall second slice of different methods and the corresponding absolute difference images between NDCT images and the resulting images. In the difference images, the darker the color is, the smaller the error will be. It can be clearly observed that the result of CycleGAN-BM3D has the smallest difference.

For further analysis of image details, two regions were selected as ROIs, which are shown in Figure 10. In ROI I, the tissue pointed by red squares is smeared out in the BM3D images but is easily identifiable in the CycleGAN and CylceGAN-BM3D images. As marked by the yellow ellipses in ROI II, the three black holes in the results of BM3D and CycleGAN are blurred and inseparable but are recognizable in the result of CycleGAN-BM3D. Furthermore, the smooth area below the ROI II of CycleGAN-BM3D is the most similar to the NDCT image.

Based on the visual effect, the proposed network CycleGAN-BM3D can not only better suppress noise but also retain more details than the other networks. More importantly, after adding the constraint of prior information, CycleGAN-BM3D can effectively prevent the generation of fake details compared with the original CycleGAN without prior information.

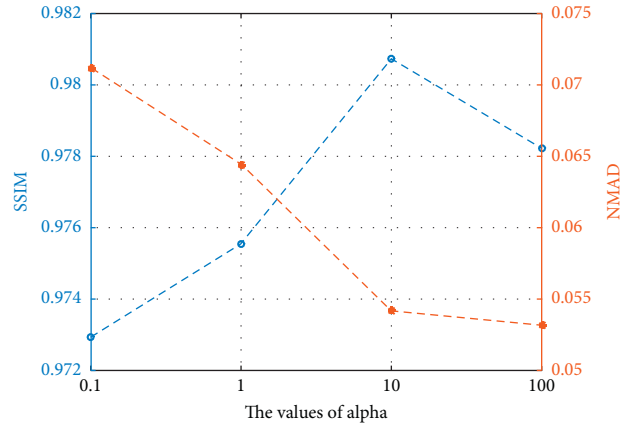

Figure 7: Average SSIM and NMAD of 10 images in different values of α. The blue line indicates the SSIM curve and the orange line represents the NMAD curve.

For quantitative analysis, the average of PSNR, SSIM, and NMAD was calculated for 180 slices in the test dataset to measure performance of the proposed method and the other compared methods. (Table 2).

In each evaluation item, the results with the best performance are marked black. CycleGAN-BM3D ranks first in terms of SSIM even with the unpaired training dataset. As such, the results of CycleGAN-BM3D are the most structurally similar to the NDCT images. In terms of PSNR and NMAD, CycleGAN-BM3D also exhibits satisfactory performance, indicating that the noise removal is relatively clean. Compared with the other algorithms, CycleGAN shows the worst performance because it mainly focuses on mapping the data distribution from the LDCT to NDCT, and cyclic loss may not be enough to supervise the generation of details and suppression of noise. This method needs to add supervision during training to improve image quality. The introduction of prior information in CycleGAN-BM3D enhances the constraints to the image content. That is, in the proposed CycleGAN-BM3D method, cyclic loss plays a role in distribution mapping and prior information loss is used to guarantee the relevance of the content. Therefore, the proposed method demonstrates good performance in noise suppression and detail preservation. We note that the numerical results of BM3D are in the front rank. From the visual effect, the noise removal of BM3D is complete and the main information of the image is basically retained, as much, BM3D has a high quantitative evaluation result. That finding is the reason why we choose the result of BM3D as the prior information.

4. Discussion and Conclusion

In the modern CT imaging field, the hidden risk of radiation dose has increased the demand for LDCT. However, LDCT

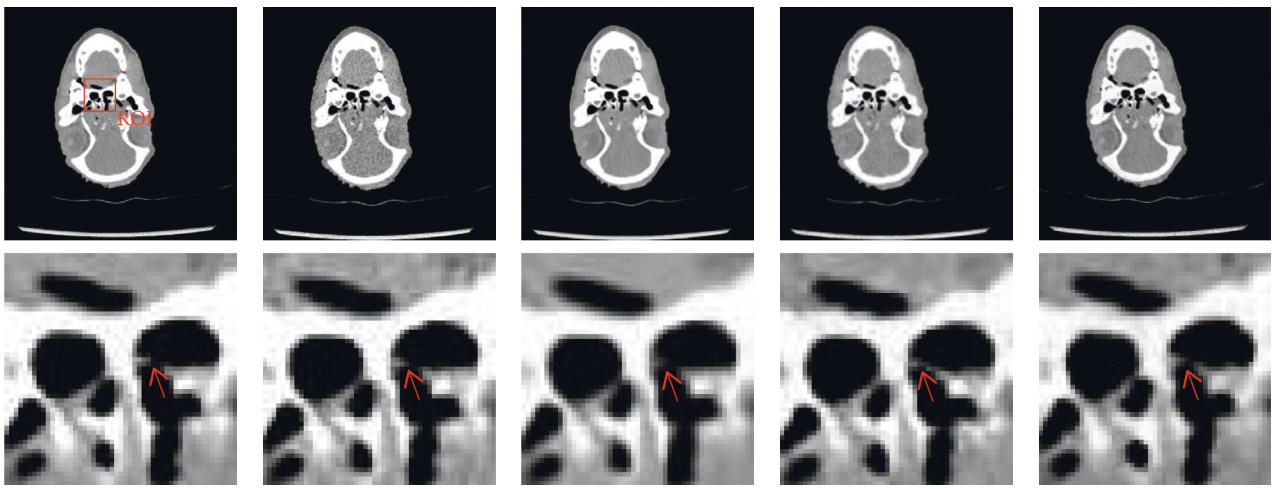

Figure 8: Results of (a) NDCT, (b) LDCT, (c) BM3D, (d) CycleGAN, and (e) CycleGAN-BM3D, respectively. The display widow is [800, 1300].

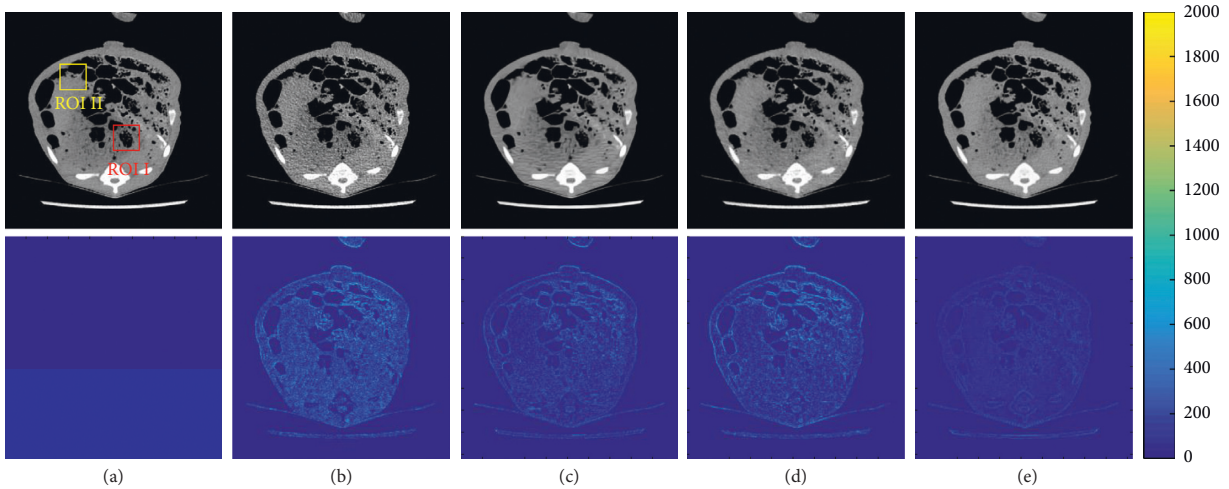

Figure 9: Results of (a) NDCT, (b) LDCT, (c) BM3D, (d) CycleGAN, and (e) CycleGAN-BM3D, respectively. The display widow is [800, 1300].

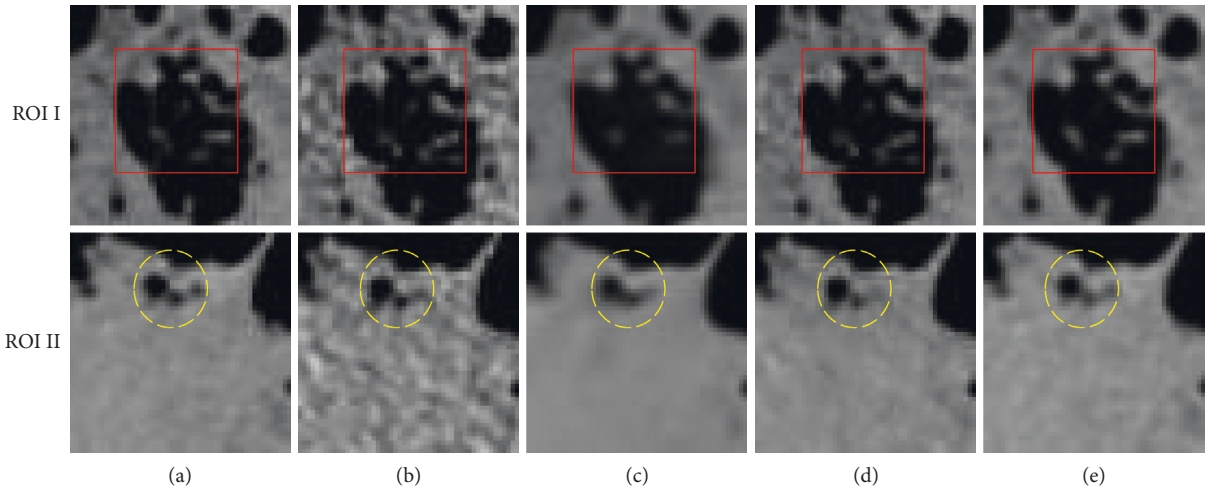

Figure 10: Zoomed-in ROIs of slice 2. The first column is the NDCT (a). The following columns are the results from (b) LDCT, (c) BM3D, (d) CycleGAN, and (e) CycleGAN-BM3D, respectively. The display widow is [800, 1300].

Table 2: Quantitative evaluation of results by different algorithms on 180 slices in the test dataset.

	PSNR	SSIM	NMAD
LDCT	27.6514 ± 1.3862	0.8698 ± 0.0375	0.1124 ± 0.0174
BM3D	32.2185 ± 0.9599	0.9271 ± 0.0245	0.0681 ± 0.0087
CycleGAN	29.0833 ± 0.8661	0.9059 ± 0.0263	0.0890 ± 0.0096
CycleGAN-BM3D	**34.3577 ± 0.1475**	**0.9798 ± 0.0041**	**0.0583 ± 0.0012**

images often suffer from serious noise, which degrades image quality and troubles clinical diagnosis. In the past two years, deep neural network provides a new idea for LDCT noise reduction. Most of the existing neural networks for LDCT reconstruction usually require well-matched datasets for network training. However, the well-matched CT images of different dose levels are difficult to obtain. This may affect the performance of networks and lead to blurred details or fake information in the resulting images.

To improve the quality of LDCT image and broaden the application of neural networks in LDCT noise reduction, this paper proposed an unpaired network based on CycleGAN with prior image information. In contrast to existing denoising networks, the proposed network can be trained by unpaired datasets, thereby alleviating the limitation of paired dataset requirement. Most GANs used to reduce noise mainly focus on the distribution mapping from LDCT to NDCT, and this process may overlook the accurate content correspondence. To enhance the constraint to the content and prevent producing fake details, we incorporate the prior image processed by BM3D into CycleGAN to supervise the generation of image content. In the experiment of real data, visual inspection demonstrated that the proposed method can suppress noise in the LDCT image and prevent the generation of fake details. The result of quantitative evaluations indicated that, after incorporating prior information, the PSNR improved more than 3 dB and SSIM also increased compared with the original CycleGAN without prior information. The results of qualitative and quantitative evaluations indicated that the proposed method exhibits reasonable performance and outperforms the original CycleGAN when applied to LDCT reconstruction.

The validity of prior information affects the performance of the proposed method. In this work, the LDCT images processed by traditional methods are obtained as prior information, which is a simple and efficient way. In the future, we intend to explore other representative shared features between LDCT and NDCT images as prior information to further improve the performance of the proposed network, such as the sparsity or sharpness information.

Data Availability

The data used in the study can be obtained from http://homepage.usask.ca/~xiy525/publication/sagan/.

Conflicts of Interest

The authors declare that they have no conflicts of interest.

Authors' Contributions

Chao Tang and Jie Li contributed equally to this work.

Acknowledgments

This study was funded by the National Natural Science Foundation of China (grant no. 61601518) and the National Key R&D Program of China (grant no. 2018YFC0114500).

References

[1] D. J. Brenner and E. J. Hall, "Cancer risks from CT scans: now we have data, what next?," *Radiology*, vol. 265, no. 2, pp. 330-331, 2012.

[2] O. W. Linton and F. A. Mettler, "National conference on dose reduction in CT, with an emphasis on pediatric patients," *American Journal of Roentgenology*, vol. 181, no. 2, pp. 321–329, 2003.

[3] D. J. Brenner and E. J. Hall, "Computed tomography—an increasing source of radiation exposure," *New England Journal of Medicine*, vol. 357, no. 22, pp. 2277–2284, 2007.

[4] I. A. Elbakri and J. A. Fessler, "Statistical image reconstruction for polyenergetic X-ray computed tomography," *IEEE Transactions on Medical Imaging*, vol. 21, no. 2, pp. 89–99, 2002.

[5] J. Wang, T. Li, and L. Xing, "Iterative image reconstruction for CBCT using edge-preserving prior," *Medical Physics*, vol. 36, pp. 252–260, 2009.

[6] P. J. L. Riviere, J. Bian, and P. A. Vargas, "Penalized-likelihood sinogram restoration for computed tomography," *IEEE Transactions on Medical Imaging*, vol. 25, no. 8, pp. 1022–1036, 2006.

[7] J. Wang, T. Li, H. Lu, and Z. Liang, "Penalized weighted least-squares approach to sinogram noise reduction and image reconstruction for low dose X-ray computed tomography," *IEEE Transactions on Medical Imaging*, vol. 25, no. 10, pp. 1272–1283, 2006.

[8] Y. Zhang, J. Zhang, and H. Lu, "Statistical sinogram smoothing for low-dose CT with segmentation-based adaptive filtering," *IEEE Transactions on Nuclear Science*, vol. 57, no. 5, pp. 2587–2598, 2010.

[9] Q. Xie, D. Zeng, Q. Zhao et al., "Robust low-dose CT sinogram preprocessing via exploiting noise-generating mechanism," *IEEE Transactions on Medical Imaging*, vol. 36, no. 12, pp. 2487–2498, 2017.

[10] A. M. R. Schilham, B. van Ginneken, H. Gietema, and M. Prokop, "Local noise weighted filtering for emphysema scoring of low-dose CT images," *IEEE Transactions on Medical Imaging*, vol. 25, no. 4, pp. 451–463, 2006.

[11] A. Borsdorf, R. Raupach, T. Flohr, and J. Hornegger, "Wavelet based noise reduction in CT-images using correlation analysis," *IEEE Transactions on Medical Imaging*, vol. 27, no. 12, pp. 1685–1703, 2008.

[12] Y. Chen, Z. Yang, Y. Hu et al., "Thoracic low-dose CT image processing using an artifact suppressed large-scale nonlocal means," *Physics in Medicine and Biology*, vol. 57, no. 9, pp. 2667–2688, 2012.

[13] B. D. Man and S. Basu, "Distance-driven projection and backprojection in three dimensions," *Physics in Medicine and Biology*, vol. 49, no. 11, pp. 2463–2475, 2004.

[14] R. M. Lewitt, "Multidimensional digital image representations using generalized Kaiser-Bessel window functions," *Journal of*

the Optical Society of America A, vol. 7, no. 10, pp. 1834–1846, 1990.

[15] B. R. Whiting, P. Massoumzadeh, O. A. Earl, J. A. O'Sullivan, D. L. Snyder, and J. F. Williamson, "Properties of preprocessed sinogram data in X-ray computed tomography," *Medical Physics*, vol. 33, no. 9, pp. 3290–3303, 2006.

[16] S. Ramani and J. A. Fessler, "A splitting-based iterative algorithm for accelerated statistical X-ray CT reconstruction," *IEEE Transactions on Medical Imaging*, vol. 31, no. 3, pp. 677–688, 2012.

[17] E. Y. Sidky and X. Pan, "Image reconstruction in circular cone-beam computed tomography by constrained, total-variation minimization," *Physics in Medicine and Biology*, vol. 53, no. 17, pp. 4777–4807, 2008.

[18] Y. Liu, J. Ma, Y. Fan, and Z. Liang, "Adaptive-weighted total variation minimization for sparse data toward low-dose X-ray computed tomography image reconstruction," *Physics in Medicine and Biology*, vol. 57, no. 23, pp. 7923–7956, 2012.

[19] Z. Tian, X. Jia, K. Yuan, T. Pan, and S. B. Jiang, "Low-dose CT reconstruction via edge-preserving total variation regularization," *Physics in Medicine and Biology*, vol. 56, no. 18, pp. 5949–5967, 2011.

[20] Q. Xu, H. Yu, X. Mou, L. Zhang, J. Hsieh, and G. Wang, "Low-dose X-ray CT reconstruction via dictionary learning," *IEEE Transactions on Medical Imaging*, vol. 31, no. 9, pp. 1682–1697, 2012.

[21] Y. Zhang, X. Mou, G. Wang, and H. Yu, "Tensor-based dictionary learning for spectral CT reconstruction," *IEEE Transactions on Medical Imaging*, vol. 36, no. 1, pp. 142–154, 2017.

[22] J. K. Choi, B. Dong, and X. Zhang, "Limited tomography reconstruction via tight frame and simultaneous sinogram extrapolation," *Journal of Computational Mathematics*, vol. 34, no. 6, pp. 575–589, 2016.

[23] A. Buades, B. Coll, and J. M. Morel, "A review of image denoising algorithms, with a new one," *Multiscale Modeling & Simulation*, vol. 4, no. 2, pp. 490–530, 2005.

[24] Z. Li, L. Yu, J. D. Trzasko et al., "Adaptive nonlocal means filtering based on local noise level for CT denoising," *Medical Physics*, vol. 41, no. 1, Article ID 011908, 2014.

[25] M. Aharon, M. Elad, and A. Bruckstein, "K-SVD: an algorithm for designing overcomplete dictionaries for sparse representation," *IEEE Transactions on Signal Processing*, vol. 54, no. 11, pp. 4311–4322, 2006.

[26] P. F. Feruglio, C. Vinegoni, J. Gros, A. Sbarbati, and R. Weissleder, "Block matching 3D random noise filtering for absorption optical projection tomography," *Physics in Medicine and Biology*, vol. 55, no. 18, pp. 5401–5415, 2010.

[27] D. Kang, P. Slomka, R. Nakazato et al., "Image denoising of low-radiation dose coronary CT angiography by an adaptive block-matching 3D algorithm," in *Proceedings of the Medical Imaging: Image Processing*, International Society for Optics and Photonics, March 2013.

[28] H. Chen, Y. Zhang, W. Zhang et al., "aLow-dose CT via convolutional neural network," *Biomedical Optics Express*, vol. 8, no. 2, pp. 679–694, Prague, Czech Republic, 2017.

[29] E. Kang, J. Min, and J. C. Ye, "A deep convolutional neural network using directional wavelets for low-dose X-ray CT reconstruction," *Medical Physics*, vol. 44, no. 10, pp. e360–e375, 2017.

[30] H. Chen, Y. Zhang, M. K. Kalra et al., "Low-dose CT with a residual encoder-decoder convolutional neural network (RED-CNN)," *IEEE Transactions on Medical Imaging*, vol. 36, no. 12, pp. 2524–2535, 2017.

[31] J. Johnson, A. Alahi, and L. Fei-Fei, "Perceptual losses for real-time style transfer and super-resolution," in *Proceedings of the European Conference on Computer Vision*, pp. 694–711, Springer, Amsterdam, The Netherlands, October 2016.

[32] C. Ledig, L. Theis, F. Huszar et al., "Photo-realistic single image super-resolution using a generative adversarial network," 2016, https://arxiv.org/abs/1609.04802.

[33] D. Wu, K. Kim, F. G. El et al., "Iterative low-dose CT reconstruction with priors trained by artificial neural network," *IEEE Transactions on Medical Imaging*, vol. 36, no. 12, pp. 2479–2486, 2017.

[34] I. Goodfellow, "Nips 2016 tutorial: generative adversarial networks," 2016, https://arxiv.org/abs/1701.00160.

[35] J. M. Wolterink, T. Leiner, M. A. Viergever, and I. Isgum, "Generative adversarial networks for noise reduction in low-dose CT," *IEEE Transactions on Medical Imaging*, vol. 36, no. 12, pp. 2536–2545, 2017.

[36] Q. Yang, P. Yan, Y. Zhang et al., "Low dose CT image denoising using a generative adversarial network with Wasserstein distance and perceptual loss," *IEEE Transactions on Medical Imaging*, vol. 37, no. 6, pp. 1348–1357, 2017.

[37] X. Yi and P. Babyn, "Sharpness-aware low-dose CT denoising using conditional generative adversarial network," *Journal of Digital Imaging*, vol. 31, no. 5, pp. 655–669, 2018.

[38] J. Y. Zhu, T. Park, P. Isola, and A. A. Efros, "Unpaired image-to-image translation using cycle-consistent adversarial networks," in *Proceedings of the 2017 IEEE International Conference on Computer Vision (ICCV)*, pp. 2242–2251, Venice, Italy, October 2017.

[39] Z. Yi, H. Zhang, P. Tan, and M. Gong, "DualGAN: unsupervised dual learning for image-to-image translation," in *Proceedings of the 2017 IEEE International Conference on Computer Vision (ICCV)*, pp. 2868–2876, Venice, Italy, October 2017.

[40] T. M. Quan, T. Nguyen-Duc, and W. K. Jeong, "Compressed sensing MRI reconstruction using a generative adversarial network with a cyclic loss," *IEEE Transactions on Medical Imaging*, vol. 37, no. 6, pp. 1488–1497, 2018.

[41] J. M. Wolterink, A. M. Dinkla, M. H. F. Savenije et al., "Deep MR to CT synthesis using unpaired data," in *Simulation and Synthesis in Medical Imaging*, pp. 14–23, Springer, Berlin, Germany, 2017.

[42] C.-B. Jin, H. Kim, W. Jung et al., "Deep CT to MR synthesis using paired and unpaired data," 2018, https://arxiv.org/abs/1805.10790.

[43] I. Goodfellow, J. Pouget-Abadie, M. Mirza et al., "Generative adversarial nets," in *Proceedings of the Advances in Neural Information Processing Systems 27 (NIPS 2014)*, Montreal, Quebec, Canada, 2014.

[44] K. He, X. Zhang, S. Ren, and J. Sun, "Deep residual learning for image recognition," in *Proceedings of the 2016 IEEE Conference on Computer Vision and Pattern Recognition (CVPR)*, pp. 770–778, Las Vegas, NV, USA, June 2016.

[45] Z. Wang, A. C. Bovik, H. R. Sheikh, and E. P. Simoncelli, "Image quality assessment: from error visibility to structural similarity," *IEEE Transactions on Image Processing*, vol. 13, no. 4, pp. 600–612, 2004.

[46] X. Mao, Q. Li, H. Xie, R. Y. Lau, and Z. Wang, "Multiclass generative adversarial networks with the L2 loss function," 2016, https://arxiv.org/abs/1611.04076v1.

Hindawi
Computational and Mathematical Methods in Medicine
Volume 2019, Article ID 1641895, 8 pages
https://doi.org/10.1155/2019/1641895

Research Article

Measuring and Monte Carlo Modelling of X-Ray and Gamma-Ray Attenuation in Personal Radiation Shielding Protective Clothing

Michaela Kozlovska,[1] **Jaroslav Solc**,[2] **and Petr Otahal**[1]

[1]*Nuclear Protection Department, National Institute for NBC Protection (SUJCHBO v.v.i.), Kamenna 262 31, Pribram, Czech Republic*
[2]*Czech Metrology Institute, Brno 638 00, Czech Republic*

Correspondence should be addressed to Michaela Kozlovska; kozlovska@sujchbo.cz

Received 13 September 2019; Accepted 15 October 2019; Published 19 November 2019

Guest Editor: Adam Konefal

A collection of personal protective equipment (PPE), suitable for use in case of accident in nuclear facilities or radiological emergencies, was gathered at the National Institute for Nuclear, Chemical and Biological Protection, Czech Republic. The shielding characteristics of the various PPE materials were measured via narrow geometry spectral attenuation measurements with point radionuclide sources covering a broad range of photon energies. Photon relative penetration and attenuation for relevant energies of the spectra were the principal experimentally determined quantities for tested PPE. Monte Carlo simulations in the MCNPX™ code were carried out to determine photon attenuation for respective energies in the tested PPE, and the results were compared to those determined experimentally. Energy depositions in a unit volume of an ORNL phantom were simulated in a radioactive aerosols atmospheric environment to determine effective doses both for the whole body and in various organs in the human torso during exposure to different dispersed radioactive aerosols while wearing one of the PPE protecting against X- and gamma-ray. This work aimed to determine the effective dose and its decrease for individual PPE protecting against X- and gamma-ray.

1. Introduction

Some samples of personal protective equipment (PPE), protecting against X- and gamma-ray, were collected and tested at the National Institute for NBC Protection (SUJCHBO v.v.i.), Czech Republic. This type of PPE can be used by first responders in emergencies such as an accident during radioactive material transportation, terrorist incidents involving radiological dispersal devices (RDD) or nuclear weapons, or by specialised emergency response workers during accidents in nuclear facilities.

The authors are not aware of any other published studies concerning X- and gamma-ray attenuation in PPE.

The collection of PPE protecting against X- and gamma-ray due to the presence of shielding layers comprising heavy metals or their alloys can be divided into two groups: (a) body overalls, covering the whole body and (b) local garments, primarily covering the torso and shielding radiation-sensitive body organs, together with nonworn equipment, such as a radiation protection shield. OPCH-90 PPE (without a shielding layer) was chosen as a reference PPE. Table 1 presents individual tested PPE together with their parameters from the manufacturers' materials and experimentally determined density thicknesses.

Relative penetration and attenuation of X- and gamma-ray, penetrating the samples and originating from different radionuclide point sources, were determined for a broad energy range, together with mass attenuation coefficients, which describe the attenuating qualities of shielding layer materials in individual PPE. Corresponding lead equivalents of individual shielding layers, which express the thickness of the equally attenuating lead sheet, were calculated as well.

The experimentally determined values of these above-mentioned quantities for the first part of the collection of PPE protecting against X- and gamma-ray were presented by Kozlovska [2].

Together with experimental testing, Monte Carlo (MC) simulations of selected individual PPE were carried out. The

Table 1: Whole body and local PPE protecting against X- and gamma-ray.

	Whole-body PPE protecting against X- and gamma-ray				Local PPE protecting against X- and gamma-ray				
PPE	DEMRON Full Body Suit	DEMRON Class 2 Full Body Suit***	HKX 1558 Whole Body Anti-Radiation Wear	OPCH-90 (the reference one)	DEMRON Radiation Torso Vest 1/2/4 Ply	Df Vest W-2mm/ W-1mm	BIORUBBER E-400 Vest + Pants	BIORUBBER E-600 Vest	DEMRON IED RDD Shield*****
Picture									
Producer	Radiation Shield Technology, USA	Radiation Shield Technology, USA	Guangzhou Hekang Biotechnology co. Ltd., China	Ecoprotect s.r.o., Czech Republic	Radiation Shield Technology, USA	Alpha Technical Research co. Ltd., Japan	YAMAMOTO Corporation, Japan	YAMAMOTO Corporation, Japan	Radiation Shield Technology, USA
Shielding layer material	DEMRON*	DEMRON*	Lead compounds, dispersed in rubber	—	DEMRON* 1/2/4 ply	Tungsten, dispersed in resin	BIORUBBER E-400**	BIORUBBER E-600**	DEMRON*
Shielding properties	Not given	Not given	Lead equivalent 0.25 mm	—	Not given	Lead equivalent 2.0 mm/ 1.0 mm****	^{137}Cs dose rate decrease 4.4%	^{137}Cs dose rate decrease 10.5%	Not given
Surface layer	Nonwoven textile	Nonwoven textile	Textile	Butyl rubber	Nonwoven textile	Nylon	Antiadhesive BRS	Antiadhesive BRS	Nonwoven textile
Density thickness ($g{\cdot}cm^{-2}$)	0.13	0.13	0.40	0.053	0.32/0.26/0.47	2.08/1.12	0.72	1.61	3.97

*DEMRON is a water- and gas-tight polymer composite of PE, PVC, and inorganic salts of high-atomic number elements DEMRON Full Body Suit (except for lead). **BIORUBBER consists of heavy metal (primarily lead) alloys dispersed in synthetic material with a regular honeycomb structure of cells, created by pure limestone. ***Meets the NFPA 1994/2007 requirements, presented by the National Fire Protection Association [1]. ****Lead equivalent set for energy 1332.5 keV of radionuclide ^{60}Co. *****Protects against improvised explosive devices (IEDs) and radiological dispersive devices (RDDs).

following quantities were simulated: relative penetration and attenuation of monoenergetic photons by individual shielding layers and energy deposition in a unit volume of the ORNL phantom while wearing or not-wearing an individual PPE protecting against X- and gamma-ray.

The X- and gamma-ray penetration rates in simulated shielding layer material of individual PPE were determined for the main energies of the spectra. The decrease of effective dose both in the whole body and, due to the presence of PPE, the human torso alone were also assessed by the MC modelling of a human body during exposure to selected dispersed radioactive aerosols.

2. Materials and Methods

2.1. Measurement of X- and Gamma-Ray Spectra. The spectra of X- and gamma-ray, penetrating tested PPE samples and originating from different radionuclide point sources, were measured by two handheld spectrometers: an InSpector 1000 with detachable IPROL-1 scintillation $LaBr_3$ probe, and a Falcon 5000 HPGe detector, both manufactured by Canberra Industries, Inc., USA.

Samples of tested PPE were placed on a holder between the source and the detector at the defined distance to meet the lowest possible dead time of the detector and avoid false pulse coincidence. Photon spectra were measured on a testing bench, which enables the precise coaxial narrow beam geometry settings of the source, the detector, and the set of both outer and inner cylindrical collimators (Figure 1). Outer collimators were made from lead, and their outer and inner diameters were 16.5 cm and 6.0 cm, respectively; the lengths were 22.5 cm and 40.5 cm, respectively, in the case of IPROL-1 $LaBr_3$ probe measurement, which was inserted into the collimator. Inner collimators were also made of lead at lengths of 8.5 cm, and their outer and inner aperture diameters were 6.0 cm and 1.2 cm, respectively.

The narrow beam geometry setting was used for spectra measurement to minimise the number of scattered photons contributing to the measured spectra unwantedly influencing peak areas and causing a build-up effect.

To cover the wide photon energy range from 30.5 keV to 1,408 keV, the following radioactive point sources activation ranging from 9.5 to 40.0 MBq were used: ^{241}Am, ^{133}Ba, ^{152}Eu, ^{137}Cs, and ^{60}Co.

Measurement live times ranged from 120 to 1,800 s to obtain net peak areas for all significant sufficiently high full-energy peaks, achieving their relative uncertainty below 1%.

Measured spectra were subsequently analysed using Genie 2000 Gamma Analysis Software v. 3.2, manufactured by Canberra Industries, Inc. For the primary spectra energies, corresponding to the main peaks of total absorption, photon penetration and attenuation rates in a tested PPE sample were determined. These quantities were determined via comparing net peak areas in the spectra, measured with the sample placed between the source and the detector, and the corresponding net peak areas in the spectra, measured without any samples, for the same time between the source and the detector.

Figure 1: Spectra measurement arrangement.

The energy dependency of mass attenuation coefficients was determined from the relative attenuation and experimentally assessed density thicknesses of individual PPE samples to describe shielding qualities of individual shielding layer materials. For each tested sample, a lead equivalent, which sets the thickness of the equally attenuating lead sheet, was determined using the values of the lead mass attenuation coefficient, stated by Johnson and Birty [3]. Mean lead equivalents for individual PPE protecting against X- and gamma-ray was set as mean of lead equivalents determined for the individual energies of significant peaks, except for absorption edges.

Together with the spectra of photons penetrating tested PPE samples, the spectra of photons penetrating a lead sheet (thickness of 1.25 mm) were similarly measured, and the same quantities were determined to test the measurement and spectra evaluation methods.

2.2. Radon-Aerosol Chamber. The Radon-Aerosol Chamber (RAC) at SUJCHBO v.v.i. we used for PPE testing in a dispersed radioactive atmosphere is a gas-tight testing box of 10 m^3 volume with dimensions of 250 cm (length) × 200 cm (width) × 200 cm (height), strictly separated from the ambient atmosphere. The RAC enables the creation of a stable atmosphere containing high concentrations of radioactive or nonradioactive aerosol particles under various physical conditions. It is also possible for the created aerosol particles to be sampled and measured externally. The RAC parameters are described by Burian [4].

2.3. Monte Carlo Simulations. Monte Carlo (MC) simulations were performed using the general-purpose MC code MCNPX™ version 2.7.E [5]. Full photon and electron transport and the detailed treatment of bremsstrahlung radiation were considered in the whole volume of the RAC. Photon transport utilised the MCPLIB04 photoatomic data library described by White [6], and the low-energy cutoff was set to 10 keV. Electron transport utilised the el03 library described by Adams [7], and the low-energy cutoff was set to 50 keV.

2.4. Simulations of PPE Materials. The elemental compositions of PPE materials necessary for input to the MC model were taken from the results of X-ray fluorescence spectrometry (XRF) and scanning electron microscopy (SEM) measurements. In addition, during the later analysis, energy-dispersive X-ray spectrometry was also applied to collect additional material information.

A simple MC model consisting of a point source emitting monoenergetic photons perpendicularly to a layer of PPE material was used to calculate relative penetration in individual PPE samples. Material relative penetration for each photon energy was obtained using an F1-type tally located behind the layer counting the number of photons (per one photon emitted from the source) that did not undergo interaction in the layer. The statistical uncertainty of the F1-tally results was 0.1%. Consequently, the relative attenuation and relative penetration at different energies were compared to those measured experimentally.

For input to the MC model, the mass density of the samples was determined by finding the best match between measured and calculated relative penetration, keeping the elemental composition fixed.

2.5. Simulations of Effective Dose. MC simulations of energy deposition in a unit volume of an ORNL phantom described by Eckerman et al. [8] were performed in the chosen dispersed radioactive aerosol environment in the RAC. The ORNL phantom was positioned in a standing position at the centre of the RAC, and it was modelled to either wear one of the simulated PPE protecting against X- and gamma-ray (respectively, the simulated PPE together with a PPE preventing radioactive contamination over it in the case of local PPE protecting against X- and gamma-ray), or to solely wear PPE preventing radioactive contamination.

The following dispersed radionuclides were simulated: ^{99m}Tc, ^{131}I, ^{137}Cs, ^{140}La, and ^{24}Na. ^{131}I and ^{137}Cs radionuclides emit both beta particles and gamma-ray of medium energies, while ^{140}La and ^{24}Na radionuclides emit both beta particles and gamma ray of high energies. However, the ^{99m}Tc radionuclide only emits gamma ray of low energy.

Both gamma and beta contributions to the effective dose were taken into account in the simulations. Energy distributions were taken from Radiological Toolbox [9], which contains data from the ICRP 38 publication [10]. Three radiation sources were considered in the RAC: (1) dispersion of the radionuclide in the air; (2) deposition on the RAC walls; and (3) deposition on the outer surface of the tested PPE or covering PPE preventing radioactive contamination. For the evaluation of the results, it was assumed that 90% of the total activity was dispersed in the air and that the surface activity of the RAC walls and PPE were equal.

The equivalent dose was determined by calculation of the absorbed dose in the ORNL phantom organs. The deposited energy in each organ was initially obtained using the *F8-type tally independently for each of three radiation sources and both gamma and beta contributions. The deposited energies in each organ were then recalculated into the equivalent dose per unit activity. The equivalent doses were finally weighted by the tissue weighting factors defined in the ICRP 103 publication [11] and summed into the effective dose.

The resulting calculated values of the whole body effective dose and equivalent doses on various organs were compared to the values of the same quantities, simulated in the same way for the ORNL phantom without the PPE. The effective dose on the human torso alone was also considered to compare individual whole-body PPE protecting against X- and gamma-ray and local ones. The following organs were included in the effective dose on the human torso calculation: lungs, stomach, colon, testes and genitalia, liver, oesophagus, urinary bladder, small intestine, gall bladder, pancreas, spleen, heart, adrenals, kidneys, and thymus.

The decrease of equivalent dose on various organs, as well as whole-body effective dose decrease and decrease of effective dose on the human torso for individual PPE protecting against X- and gamma-ray, used in atmospheres of various dispersed radionuclides, were subsequently calculated from the resulting values of corresponding equivalent and effective doses.

3. Results and Discussion

3.1. Measurement of X- and Gamma-Ray Spectra. Figure 2 presents the spectra of the ^{133}Ba radionuclide gamma-ray without PPE and the penetrating BIORUBBER E-600 Vest PPE sample. The spectra were measured with an InSpector 1000 spectrometer with a detachable IPROL-1 scintillation $LaBr_3$ probe and smoothed by averaging over three adjacent channels. A significant decrease of relative attenuation of more energetic photons, penetrating the sample, is evident from the spectra.

Experimentally determined mean lead equivalents for individual PPE protecting against X- and gamma-ray, together with a reference PPE without a shielding layer and a reference lead sheet, are presented in Figure 3. The mean lead equivalent for the DEMRON IED RDD Shield was not determined due to a strong build-up factor in the thick material, inversely depending on penetrating photon energy.

From the mean lead equivalent values of tested PPE samples, it is evident that the higher the density thickness of a tested sample, the higher its lead equivalent (Figure 3 and Table 1). The mean lead equivalent of some of the tested PPE protecting against X- and gamma-ray does not even meet the requirements of 0.35 mm, respectively, 0.25 mm, for the lead equivalent of heavy protective aprons, respectively, light protective aprons, used by radiological operators, respectively, used in operating rooms, and specified by CENELEC 1999 [12].

The lead equivalent of the reference OPCH-90 PPE (without any shielding layer) is almost negligible; the mean lead equivalent of the reference Pb sheet of 1.22 ± 0.10 mm corresponds to its thickness of 1.25 mm. The experimentally assessed mean lead equivalent value for HKX 1558 Whole-Body Anti-Radiation Wear equal to 0.24 ± 0.02 mm corresponds to the value of 0.25 mm stated by the manufacturer (Table 1).

The experimentally determined lead equivalent for Df Vest W-1 mm equal to 0.99 ± 0.10 mm at the energy of 1,332.5 keV corresponds to the value of 1.0 mm stated by the manufacturer, while the same quantity for Df Vest W-2 mm

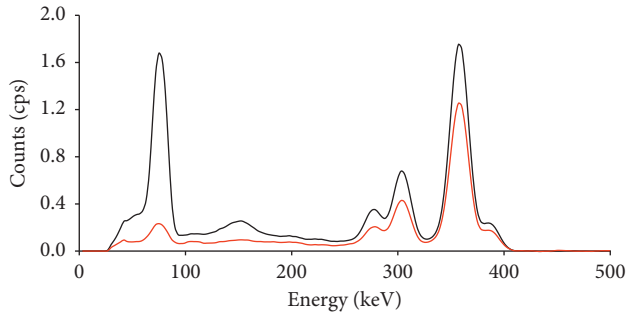

Figure 2: Smoothed spectra of radionuclide ^{133}Ba gamma-ray without a PPE (black line) and penetrating BIORUBBER E-600 Vest (red line), measured with an InSpector 1000 spectrometer with a detachable scintillation $LaBr_3$ probe IPROL-1.

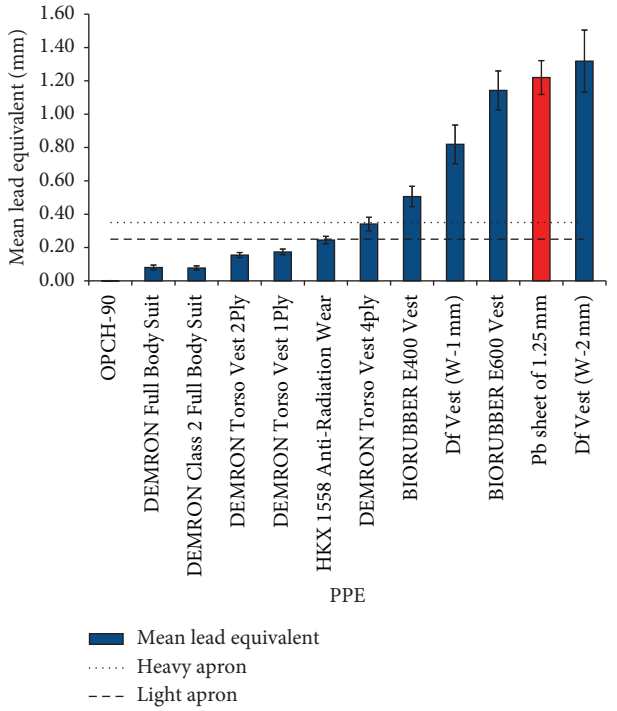

Figure 3: Mean lead equivalents of tested PPE (the mean lead equivalent of reference Pb sheet is red) together with CENELEC requirements for heavy and light aprons. Error bars represent the standard deviation of measurements.

of 1.71 ± 0.06 mm is 14.5% lower than the value of 2.0 mm stated by the manufacturer (Table 1). However, lead equivalent values determined at lower energies for both these PPE, as well as mean lead equivalents, are lower, which indicates the presence of a build-up factor in these relatively thick materials.

4. Monte Carlo Simulations of PPE Material

Figure 4 presents the energy dependence of measured and simulated photon relative penetration in the BIORUBBER E-400 Vest and their relative difference. Both measured and simulated penetration rates are in excellent agreement, which proves the correctness of (1) the PPE material composition determined by XRF and SEM measurements and (2) the estimated density thickness of the material. The decreased relative photon penetration (and therefore increased attenuation) at the energy of about 88 keV corresponds to the lead absorption edge, which occurs at photoelectric absorption when there is sufficient photon energy to eject an electron from the K-shell.

Similar agreement between measured and simulated attenuation and penetration was obtained for all other studied materials as well.

5. Monte Carlo Simulations of Effective Dose

Figure 5 presents an example of visualisation of simulated ORNL phantom energy depositions while only wearing PPE preventing radioactive contamination, and the same PPE together with the BIORUBBER E-600 Vest under it, in a dispersed ^{99m}Tc aerosol atmosphere. Visualisations for other PPE or other radionuclides are presented in the electronic annex.

For the selected dispersed radioactive atmosphere, a decrease of energy deposition due to the presence of PPE protecting against X- and gamma-ray depends on the PPE lead equivalent. On the other hand, the higher the beta and gamma particle energy emitted by dispersed radionuclide, the lower the decrease of energy deposition, as higher energy particles are much less attenuated by PPE (Figure 2).

Table 2 presents decrease of the various organs' contribution to the effective dose when protected with individual tested PPE exposed to the ^{131}I radionuclide dispersed in 10 m^3 of the atmosphere in the RAC geometry. Numerical results for other studied radionuclides are presented in the electronic annex. However, the results for other radionuclides are graphically presented in Figure 6, which summarises values of the effective dose decrease on human torso organs when protected with individual tested PPE exposed to various radionuclides in the given geometry.

For individual simulated dispersed radionuclides, it is evident from Figure 6 that the higher the density thickness (and corresponding lead equivalent) of the PPE protecting against X- and gamma-ray, the higher the decrease of the effective dose. On the other hand, the higher the beta and gamma particle energy emitted by dispersed radionuclides, the lower the decrease of the effective dose.

For the simulated ^{99m}Tc radionuclide, the decrease of the effective dose on the human torso organs of an ORNL phantom, protected by individual PPE protecting against X- and gamma-ray, is significantly higher than the resulting decrease when protected by the reference PPE OPCH-90 without a shielding layer. However, in the case of other simulated radionuclides, the decrease of the effective dose on human torso organs is only significantly higher than that of the reference PPE if the ORNL phantom is protected by PPE of a sufficient lead equivalent, which meets the CENELEC requirements for heavy and light aprons, used to shield against diagnostic medical X-ray radiation (Figures 6 and 3).

Most of the radiation-sensitive organs of the body are situated in the human torso, so the decrease of the whole-body

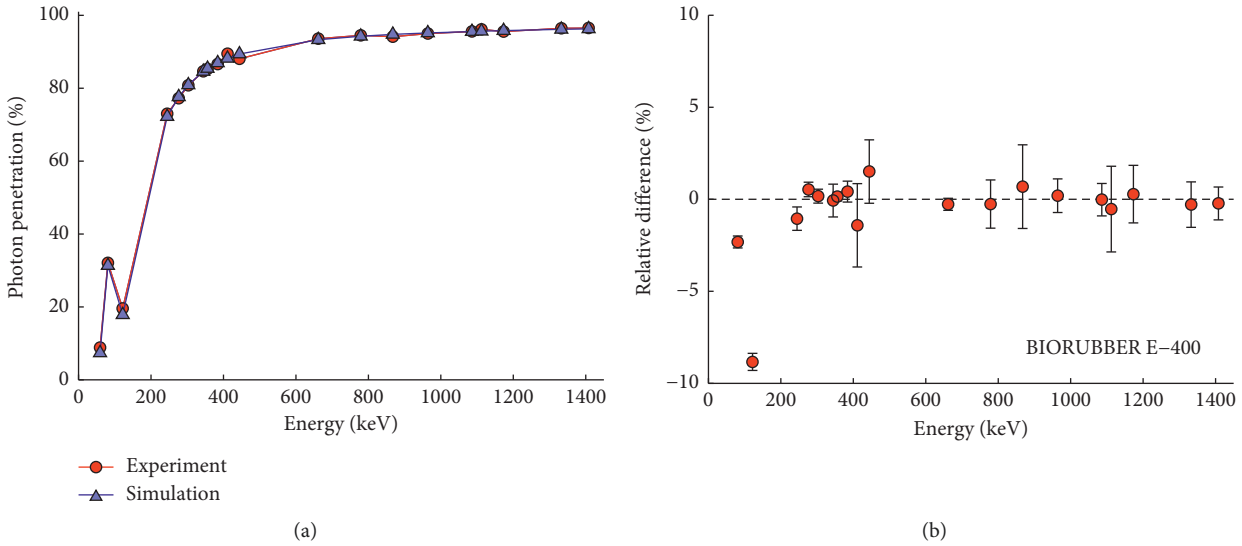

Figure 4: BIORUBBER E-400 Vest material. (a) Measured and simulated photon relative penetration. Error bars are equivalent to data point size. (b) Relative difference between measured and simulated relative photon penetration.

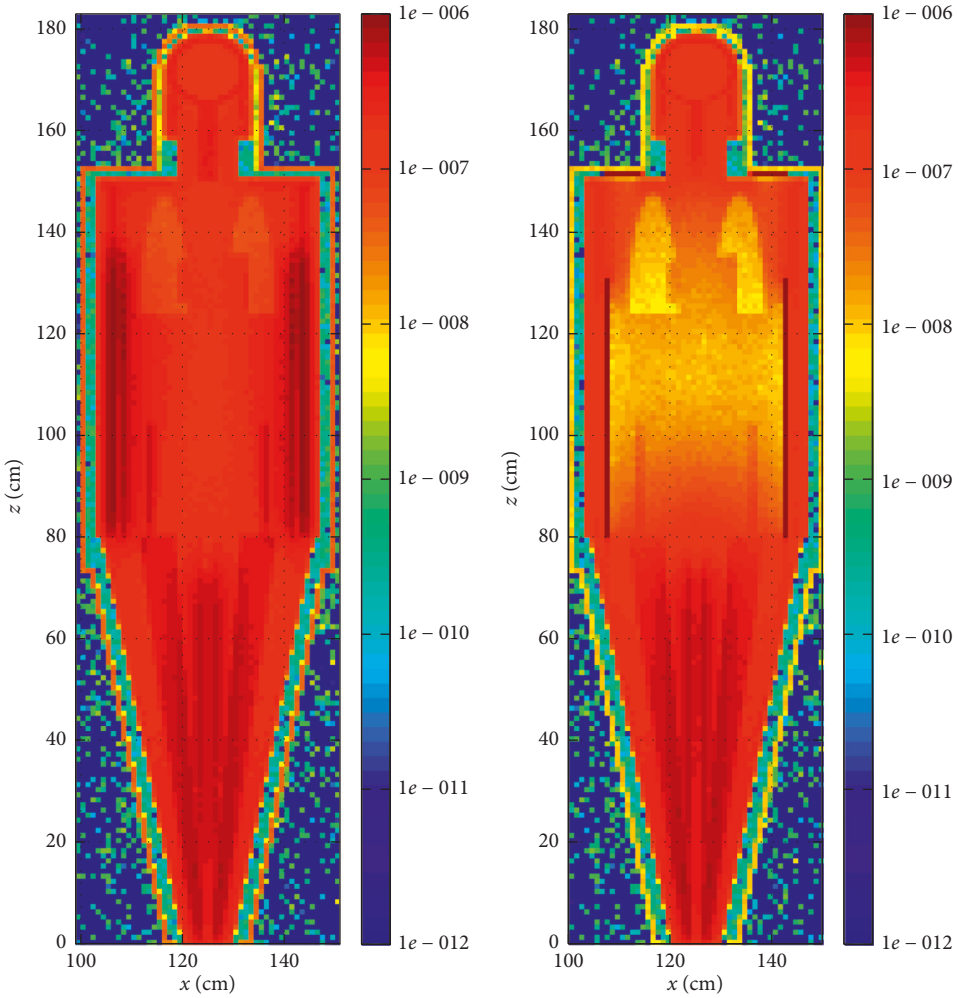

Figure 5: An example of simulated energy deposition in ORNL phantom, wearing PPE preventing radioactive contamination only (a) and the same PPE together with BIORUBBER E-600 Vest (b) in dispersed ^{99m}Tc aerosol atmosphere. Colorbar in relative units.

Table 2: Decrease of various organs' contribution to the effective dose when protected with individual tested PPE in an atmosphere of dispersed radionuclide ^{131}I. Organs included in "torso organs" are listed in the text.

PPE protecting against X- and gamma-ray	Torso organs (%)	Lungs (%)	Testes and genitalia (%)	Brain (%)	Thyroid (%)	Skin (%)
DEMRON Full Body Suit	−5.4	−4.9	−4.8	−1.5	−1.0	−84.8
DEMRON Class 2 Full Body Suit	−5.2	−4.7	−4.5	−1.5	−0.9	−84.8
HKX 1558 Whole Body Wear	−14.3	−13.5	−15.1	−8.0	−11.3	−88.0
OPCH 90 (the reference one)	−4.7	−4.3	−0.5	1.6	3.9	−82.1
DEMRON Torso Vest 2Ply	−7.2	−6.3	−8.5	−1.0	−4.3	−39.2
DEMRON Torso Vest 4Ply	−12.3	−11.0	−13.2	−1.6	−7.2	−39.6
DF Vest W-2 mm	−38.7	−34.0	−46.3	−3.9	−19.7	−50.8
BIORUBBER RSM E400 Torso Vest	−15.8	−16.2	−5.2	−1.9	−9.3	−36.1
BIORUBBER RSM E600 Torso Vest	−30.0	−30.9	−7.2	−3.3	−14.3	−35.9

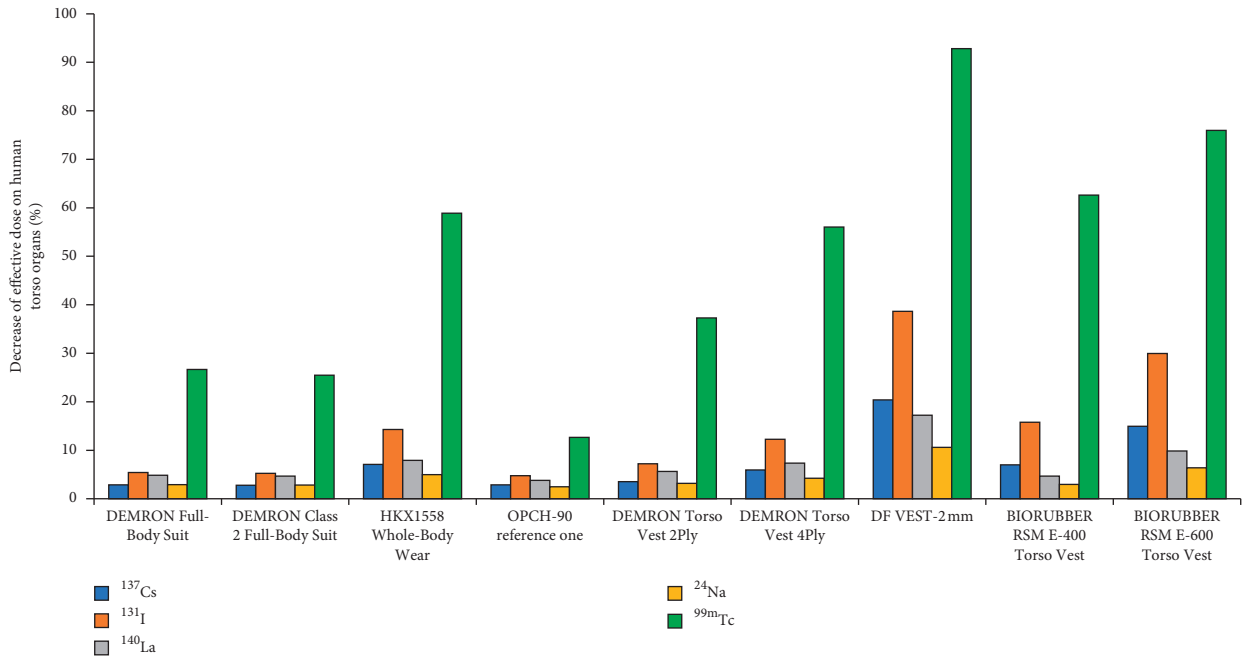

Figure 6: Simulated decrease of effective dose on human torso organs when protected with tested PPE exposed to various radionuclides dispersed in the atmosphere.

effective dose obtained with vests is similar to the decrease of human torso effective dose only. For the same decrease of effective dose, it is more efficient to use vests instead of whole-body PPE because the vests are much lighter. For example, the Demron Radiation Torso Vest 4 Ply weighs 4.3 kg, while HKX 1558 Whole-Body Anti-Radiation Wear weighs 10.1 kg. However, the effective dose decrease on human torso organs gained with these two PPE is comparable.

6. Conclusions

A collection of personal protective equipment protecting against X- and gamma-ray was gathered and tested at the National Institute for NBC Protection, Czech Republic. Relative penetration of X- and gamma-ray in tested samples in the energy range from 30.5 to 1,408 keV was determined.

Measurements were supported with Monte Carlo simulations in the MCNPX™ code determining relative penetration and attenuation of PPE. The simulated data resulted in excellent agreement with measurements. After this validation of the MC models of tested PPE, simulations of energy deposition in organs of an ORNL phantom, in the chosen dispersed radioactive aerosol environment, were performed. Consequently, to estimate the efficiency of the PPE, whole-body effective dose and equivalent dose in various organs in the human torso were calculated and compared to the values of the same quantities, similarly simulated for the ORNL phantom without the simulated PPE in the various dispersed radioactive aerosol atmospheres.

Data Availability

The measured spectra and simulated energy depositions in the ORNL phantom used to support the findings of this study are available from the corresponding author upon request. Visualisations of simulated energy depositions in the ORNL phantom are presented in the electronix annex.

Conflicts of Interest

The authors declare that there are no conflicts of interest regarding the publication of this paper.

Acknowledgments

These experiments comprised a part of the "Prevention, Preparedness, and Mitigation of Severe Accidents at Czech Nuclear Power Plants in Connection with New Findings of Stress Tests after the Fukushima Accident" project (no. VG 20132015105, funded by the Ministry of the Interior of the Czech Republic).

Supplementary Materials

The electronic annex presents (1) numerical decrease of the various organs' contribution to the effective dose when protected with individual tested PPE exposed to the other simulated radionuclides dispersed in 10 m3 of the atmosphere in the RAC geometry (Table 2) and (2) visualisations of simulated ORNL phantom energy depositions while only wearing PPE preventing radioactive contamination, and the same PPE together with individual PPE protecting against X- and gamma-ray under it, in a various-dispersed radionuclide's aerosol atmosphere. (*Supplementary Materials*)

References

[1] National Fire Protection Association, *NFPA 1994 Standard on Protective Ensembles for First Responders to CBRN Terrorism Incidents*, National Fire Protection Association, Quincy, MA, USA, 2007 edition, 2006, http://www.niordc.ir/uploads/nfpa_1994_-_2007.pdf.

[2] M. Kozlovska, R. Cerny, and P. Otahal, "Attenuation of X and gamma rays in personal radiation shielding protective clothing," *Health Physics*, vol. 109, no. Supplement 3, pp. S205–S211, 2015.

[3] T. E. Johnson and B. K. Birty, *Health Physics and Radiological Health*, Lippincott Williams & Wilkins, Philadelphia, PA, USA, 1998.

[4] I. Burian, P. Otahal, J. Vosahlik, and E. Pilecka, "Czech primary radon measurement equipment," *Radiation Protection Dosimetry*, vol. 145, no. 2-3, pp. 333–336.

[5] D. B. Pelowitz, "MCNPX™ 2.7.E extensions—a general monte carlo n particle transport code," Report LA-UR-11-01502, Los Alamos National Laboratory, Los Alamos, NM, USA, 2011.

[6] M. C. White, "Photo-atomic data library MCPLIB04: A New Photoatomic library based on data from ENDF/B-VI release 8," Report LA-UR-03-1019, Los Alamos National Laboratory, Los Alamos, NM, USA, 2003.

[7] K. J. Adams, "Electron upgrade for MCNP4B," Report LA-UR-00-3581, Los Alamos National Laboratory, Los Alamos, NM, USA, 2000.

[8] K. F. Eckerman, M. Cristy, and J. C. Ryman, *The ORNL Mathematical Phantom Series*, 1996.

[9] K. F. Eckerman and A. L. Sjoreen, "Radiological Toolbox User's Guide," *Oak Ridge National Laboratory, ORNL/TM-2013/16*, U.S. Nuclear Regulatory Commission, NUREG/CR-7166, Oak Ridge, TN, USA, 2013.

[10] International Commission on Radiological Protection, "Radionuclide transformations: energy and intensity of emissions. ICRP publication 38," in *Annals of the ICRP*, vol. 16, no. 2/3, Pergamon Press, New York, NY, USA, 1983.

[11] ICRP, "The 2007 recommendations of the international commission on radiological protection. ICRP publication 103," *Annals of the ICRP*, vol. 37, no. 2-4, 2007.

[12] CENELEC, *Protective Devices against Diagnostic Medical X-Radiation— Part 3: Protective Clothing and Protective Devices for Gonads*, CENELEC EN 61331-3, Brussels, Belgium, 1999.